



Universiteit
Leiden
The Netherlands

Conductance of perovskite oxide thin films and interfaces

Mubeen Dildar, I.

Citation

Mubeen Dildar, I. (2013, February 6). *Conductance of perovskite oxide thin films and interfaces*. *Casimir PhD Series*. Retrieved from <https://hdl.handle.net/1887/20501>

Version: Not Applicable (or Unknown)

License: [Licence agreement concerning inclusion of doctoral thesis in the Institutional Repository of the University of Leiden](#)

Downloaded from: <https://hdl.handle.net/1887/20501>

Note: To cite this publication please use the final published version (if applicable).

Cover Page



Universiteit Leiden



The handle <http://hdl.handle.net/1887/20501> holds various files of this Leiden University dissertation.

Author: Mubeen Dildar, Ishrat

Title: Conductance of perovskite oxide thin films and interfaces

Issue Date: 2013-02-06

Conductance of perovskite oxide thin films and interfaces

Proefschrift

ter verkrijging van
de graad van Doctor aan de Universiteit Leiden,
op gezag van de Rector Magnificus prof. mr. P.F. van der Heijden,
volgens besluit van het College voor Promoties
te verdedigen op Woensdag 6 februari 2013
klokke 16:15 uur

door

Ishrat Mubeen Dildar
geboren te Lahore, Pakistan
op 23 augustus 1978

Promotiecommissie

Promotor:	Prof. dr. J. Aarts	
Overige leden:	Prof. dr. J. Santamaría	(University of Madrid)
	Prof. dr. E. R. Eliel	
	Dr. ir. S. J. van der Molen	
	Prof. dr. ir. T. H. Oosterkamp	
	Prof. dr. ing. A. J. H. M. Rijnders	(Universiteit Twente)
	Prof. dr. J. Zaanen	
	Prof. Dr. H. W. Zandbergen	(Universiteit Delft)

Cover Illustration: A high resolution TEM micrograph of the interface between two band insulators LaAlO_3 and SrTiO_3 .

The research reported in this thesis has been funded by the Higher Education Commission of Pakistan (HEC).

Internet: <http://www.hec.gov.pk>

This research has been partly funded by the Leiden Institute of Physics (LION) and the Stichting voor Fundamenteel Onderzoek der Materie (FOM), the Netherlands.

Casimir PhD series, Delft-Leiden 2013-3

ISBN: 978-90-8593-148-5

©Ishrat Mubeen Dildar

To my mother

Contents

1	Introduction	1
2	Oxide films and interfaces	5
2.1	Physics of manganites	5
2.1.1	The crystal structure	5
2.1.2	Electronic features of undoped LaMnO_3	6
2.1.3	Doped LaMnO_3 & double exchange mechanism	8
2.2	Phase diagram of $\text{La}_{1-x}\text{B}_x\text{MnO}_3$, $\text{B}=\text{Ca},\text{Sr}$	9
2.3	Electronic transport in thin films of metallic manganites	12
2.3.1	Effect of strain in thin films of manganites	12
2.3.2	On the critical thickness	14
2.3.3	Hall effect in manganites	15
2.4	Interfaces of complex oxides	17
2.4.1	Intrinsic Electronic reconstruction	18
2.4.2	Oxygen Vacancies	20
2.4.3	Intermixing Effects	21
2.4.4	Conducting interfaces made by MBE and cationic stoichiometry	21
2.4.5	Oxide interfaces versus semiconductors and devices	22
3	Sample fabrication and characterization	29
3.1	Sputtering	29
3.1.1	DC and RF reactive sputtering	30
3.1.2	Targets, substrates and thin film growth process	30
3.2	Surface and structure characterization	33
3.2.1	Atomic Force Microscopy	33
3.2.2	X-ray reflectometry (XRR)	35

3.2.3	X-ray Diffraction (XRD)	35
3.2.4	Reciprocal Space Mapping (RSM)	36
3.3	Lithographical techniques for patterning	36
3.3.1	Optical lithography	37
3.3.2	Electron beam lithography	38
3.4	Measuring properties of thin films	38
3.5	Avoiding target degradation in sputtering manganite thin films	38
3.5.1	Characteristic features of thin films of LCMO	39
3.5.2	Observations-possible causes of rough films	40
3.5.3	Hypothesis - role of Oxygen in LCMO	40
3.5.4	Results-Reutilizing the LCMO target	42
3.5.5	Pre-conditioning only	44
3.5.6	Role of substrate orientation	46
3.5.7	Conclusion	46
4	Carrier density in thin films of doped manganites	49
4.1	Introduction	50
4.2	Experimental	51
4.3	Results	52
4.3.1	Characterization by AFM	52
4.3.2	Characterization by RSM	52
4.3.3	Resistivity measurement	52
4.3.4	Hall Offset as a homogeneity parameter	57
4.4	Discussion	61
4.5	Anomalous Hall effect	64
4.6	Conclusion	66
5	Mesoscopic transport in thin films of $\text{La}_{0.67}\text{Sr}_{0.33}\text{MnO}_3$	71
5.1	Introduction	71
5.2	Experimental	72
5.3	Results	73
5.4	Discussion	79
5.5	Conclusion	83
6	Interfaces of $\text{LaAlO}_3/\text{SrTiO}_3$ made by sputter deposition	87
6.1	Introduction	87
6.2	Sputter grown LAO/STO interfaces	88
6.2.1	Surface characterization by AFM	90
6.2.2	Characterization by XPS	93
6.2.3	Thickness measurement of LaAlO_3 films by XRR	93
6.2.4	Structure of LaAlO_3 thin films by XRD	96
6.3	Interface Conductance	96
6.4	The LAO/STO Interface	98
6.4.1	Quality of interface	98
6.4.2	Stoichiometry of LAO film	103

6.4.3	Intermixing effects	103
6.4.4	Attempts to fabricate conducting interfaces	104
6.5	Discussion	106
6.5.1	Conclusion	110
6.6	Magnetic Properties of sputter grown interfaces	110
6.6.1	Introduction	110
6.6.2	Experimental	111
6.6.3	Results	112
6.6.4	Discussion	114
6.6.5	Conclusion	116
	Summary	121
	Samenvatting	123
	Curriculum Vitae	125
	List of publications	127
	Acknowledgments	129

Introduction

The physics of metallic oxides has been an area of intense research ever since the discovery of high temperature superconductivity by Bednorz and Müller in 1986. In that case, the oxide was $(\text{La,Ba})_2\text{CuO}_4$, which, as we would now describe it, consisted of a parent compound La_2CuO_4 in which the trivalent La was partly replaced by divalent Ba. As a consequence, the Cu takes on a mixed valence character and can be Cu^{2+} or Cu^{3+} . The material in question is a perovskite, which can be thought of as containing Cu-O planes, and the Ba doping leads to hole doping of these Cu-O planes. Here, all the ingredients which makes the correlated electron (metallic) oxides so interesting, come together. The parent compound is a Mott insulator, in which the Cu d electrons cannot form a band because of the strong Coulomb interactions. It is also magnetic, because the Cu has a half-integer spin ($S = 1/2$). Doping then brings in holes, bands start to form, and the magnetism changes its character. Within the family of perovskite oxides, all of the $3d$ elements can be accommodated in the structure, and all yield different properties. In particular the Mn-based materials have their own interesting niche. The parent compound LaMnO_3 (a perovskite variant with a somewhat different structure than the 2-1-4 compound discussed above) is also an antiferromagnetic insulator, with the magnetism coming from the trivalent manganese with spin $S = 2$. Doping with divalent ions such as Ca or Sr also here leads to metallicity, and also the antiferromagnetism is replaced by ferromagnetism. Since the electronic band formation forces the electron spins to be parallel in this case, transitions can be found from a paramagnetic insulating phase to a ferromagnet metallic (FM) one. This is the basis of the so-called Colossal magnetoresistance effect, which was (re)discovered in 1991. More phases are possible than the FM one, and in particular static ordering of the charges, or also ordering of the directions of directed d -orbitals, leads to a multitude of physical phenomena.

Although the research questions are mostly curiosity-driven, a possible interest from an applications point of view is that in going from a Mott insulating state to a metallic state, large numbers of electrons become available for conduction, and

this might offer alternative scenarios for transistor-like devices. Next to research on bulk materials, it is therefore of interest to study the behavior of these materials in thin film form. This also leads to other particular questions. Films have to be grown on substrates, high quality films should have small amounts of defects, and an epitaxial relation with the substrate is therefore strongly desired. Even then, lattice parameters will usually not match, and the films will be under tensile or compressive strain, which also has consequences for the out-of-plane lattice parameter. Since the properties of the perovskites are strongly linked to their structure, consisting of deformable cages of oxygens surrounding the metal ions, strain will lead to different properties, and strain engineering becomes a possibility. Working in the direction of devices, there are then two important questions, which also have strong fundamental coloring. One is how thin a film can be made on a given substrate and still show uniform and homogeneous properties (which may still be different from the bulk because of the strain). In other words, what is the possible influence of the interface and the various discontinuities presented by the interface. The other is whether the charge carrier density can be influenced by an electric field, and therefore is switchable. Here, the field offers a bonus in the sense that one of the most used substrates for perovskites growth, SrTiO_3 (a Ti-based 1-1-3 perovskite itself) has a very high dielectric constant, and is therefore very suitable for applying electric fields. This Thesis concentrates on the first question posed above, about the conducting properties of very thin films and interfaces, but it opens the door to the second question by using SrTiO_3 as the preferred substrate.

In the first part, we study two different manganites which have been doped into the metallic regime, $\text{La}_{0.7}\text{Ca}_{0.3}\text{MnO}_3$ (LCMO) and $\text{La}_{0.7}\text{Sr}_{0.3}\text{MnO}_3$ (LSMO). When grown on various substrates, in particular on SrTiO_3 (STO), it is known that the strain leads to a change of the temperature of the combined paramagnetic-to-ferromagnetic and insulator-to-metal transition, which is most pronounced in LCMO. There, the bulk transition temperature of about 270 K goes down to 110 K for very thin films on STO. This is connected to subtle changes in the structure and the electronic bandwidth, but there is also the question whether the carrier concentration or the basics of the band structure are changing. This is investigated by measuring the Hall effect in various combinations of manganites and substrates. The data indicate that, quite generically, the electrical conductance of the films are due to the combined effect of the strained material, and a relatively thick layer extending from the interface with non- or badly conducting properties. This layer is of the order of 5 nm and therefore relatively thick. We also investigate what happens with the properties of such films when they are structured into bridges of micron- or submicron width. Here we concentrate on LSMO, and find that structuring down to 1 μm does not change the basic conducting properties, but going down to 300 nm does : the conductance becomes non-Ohmic, which is probably due to loss of oxygen, or oxygen-based inhomogeneities.

In the second part, we go to a slightly different subject, and study the properties of the interface between two simple perovskite band insulators, LaAlO_3 (LAO) and SrTiO_3 . The interest here lies in the fact that the discontinuity in the charge variation which occurs when stacked layers of ionic AlO and LaO_2 give way to

neutral SrO and TiO₂ is believed to lead to a conducting interface. This has been a much investigated topic in the last ten years. The conductance is (quasi-) 2-dimensional, which is of interest in itself, while gating can be applied when the substrate is STO on which a thin film of LAO is grown. It has become clear over time, that not only electronic reconstruction (moving charges to the interface to compensate for the discontinuity) plays a role, but also intermixing effects, oxygen vacancies, and even possibly stoichiometry. Almost all of the published research has been performed on samples grown with the process of pulsed laser deposition (PLD), and it is well documented that the interface properties, including the amount of conductance, are correlated with the oxygen background pressure which is used in the process, and which should not be too high. The interfaces studied in this thesis are grown by sputtering in a high background pressure of oxygen (typically 10³ higher than in PLD), and they are found to be insulating, and also non-magnetic. Investigations by transmission electron microscopy show them to be of high quality, and it seems the high oxygen pressure is the important factor in rendering the interface non-conducting, although the afore-mentioned issue of stoichiometry also plays a role. This leads to a different perspective on the formation of the conducting layer.

Outline of thesis

Following this Introduction, in **chapter 2** we discuss the fundamental physics of manganese perovskite oxides. The phase diagram, electrical transport phenomena and the effects of strain are discussed there. In **chapter 3**, the deposition technique of sputtering in a high oxygen pressure atmosphere is presented, and details are given of the techniques used to characterize the thin films which are grown in this way. In **chapter 4**, measurements of the ordinary and anomalous Hall effect are presented and used to discuss the transport properties of very thin films of LCMO and LSMO. In **chapter 5**, the transport properties of LSMO thin films are studied further, now by structuring them down to mesoscopic length scales by electron beam lithography. In **chapter 6**, the results are presented of the fabrication of interfaces between LAO and STO by reactive radiofrequency sputtering, which are found to be non-conducting. Since the possibility of magnetism at the interfaces also is under discussion, magnetic properties are measured as well, and an estimate is given for the upper boundary of the amount of magnetism present at these sputtered interfaces.

Oxide films and interfaces

This chapter provides a general introduction in the physics of manganite perovskites, both for bulk materials and in thin film form. It also provides an introduction into the phenomena encountered at interfaces of complex oxides, in particular at the interface between two insulators SrTiO_3 and LaAlO_3 .

2.1 Physics of manganites

The perovskite-type manganites have the general formula $\text{RE}_{1-x}\text{AE}_x\text{MnO}_3$, where RE stands for trivalent rare earth ions such as La, Pr, and Nd and A for divalent alkaline earth ions such as Sr, Ca, and Ba. Depending on the composition, they show a variety of magnetic and electronic phenomena, including ferromagnetism, antiferromagnetism, charge and orbital ordering and magnetic-field driven metal insulator transitions. The physical properties of the manganites strongly depend on their crystal structure, and they are therefore sensitive to pressure and strain. There is a general relation between the electronic parameters and the structural modification in the perovskites which is described below.

2.1.1 The crystal structure

The manganites belong to the family of perovskites. The general formula is ABO_3 where A and B are two cations of different size and O is the anion that bonds them together. In the idealized cubic unit cell of such a compound, the A atom sits at corner positions (0,0,0), the B atoms sits at body centered positions (1/2, 1/2, 1/2) and oxygen atoms sit at face centered positions (1/2, 1/2, 0) as shown in Figure 2.1. So, the B cations are in a 6-fold coordination surrounded by an octahedron of anions and the A cation in 12-fold cubo-octahedral co-ordination.

The sizes of the ionic radii of ABO_3 determine the so-called tolerance factor t , which measures how well the B-atom fits in the AO_6 cage. Using the radii r_A , r_B

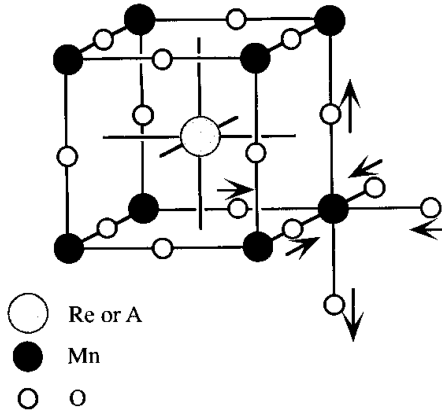


Figure 2.1: The perovskite type manganites with general formula ABO_3 . Taken from ref. [10].

and r_O of the A-, B- site ions and the oxygen, t is defined as

$$t = \frac{(r_A + r_O)}{\sqrt{2}(r_B + r_O)} \quad (2.1)$$

For cubic structures $t = 1$. In manganites, the smaller size of the A-site atoms generally leads to a smaller tolerance factor, $t < 1$. That places the B–O bonds under compression and the A–O bonds under tension. As a consequence, the oxygen octahedra have to buckle in order to fill the space around the A-site atoms. This buckling consists of rotation of the octahedra about the a, b, and c axis (a 3-axis rotation). The final effect is that the structure deforms into a Pnma orthorhombic, rhombohedral or tetragonal structure depending on the relative orientation of deformation [1].

2.1.2 Electronic features of undoped LaMnO_3

The undoped compound LaMnO_3 is a Mott insulator. Its structure has been thoroughly studied by neutron diffraction experiments [2]. Its electronic configuration allows for orbital ordering as stated below.

The Mn atom in undoped LaMnO_3 is surrounded by an oxygen octahedron. The configuration of the outer electrons in the manganese ion is $3d^4$. The degeneracy is lifted by the crystal field as shown in Figure 2.2. The five 3d orbitals divide into two sets of orbitals which are degenerate. The doublets are d_z^2 and $d_{x^2-y^2}$, denoted by e_g . The three lower lying triplets, d_{xy} , d_{yz} and d_{zx} are denoted by t_{2g} . The e_g orbitals are oriented towards the neighboring oxygen while the t_{2g} states

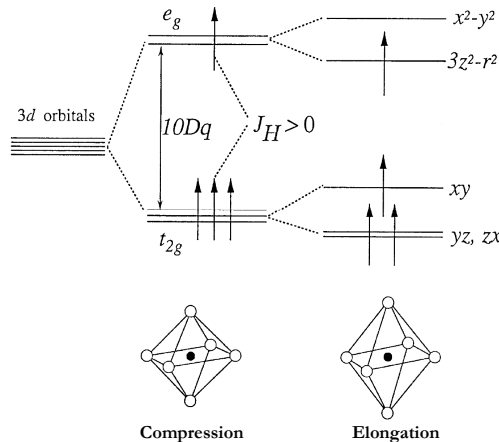


Figure 2.2: Ligand-field splitting of five-fold degenerate atomic 3d levels into lower t_{2g} (triply degenerate) and higher e_g (doubly degenerate) levels. Jahn-Teller distortion of the MnO_6 octahedron further lifts each degeneracy in compressed and elongated mode as shown in the figure, taken from ref. [13].

have nodes in these directions. This means e_g orbitals can intermix with oxygen p orbitals. The crystal field splitting between the t_{2g} and e_g is about 1 eV.

Double occupancy of an individual t_{2g} level is strongly suppressed by Hund's coupling rule and electrostatic repulsion, so the three 3d electrons in Mn^{+4} are spin aligned in the t_{2g} levels (spin $S=3/2$). The Mn^{+3} ion has one additional electron, which does not occupy a t_{2g} level due to strong Coulomb repulsion and the Pauli exclusion principle, but instead occupies one of the e_g levels. This electron is also strongly Hund coupled and therefore spin-aligned with the t_{2g} triplet, making $S = 2$.

The e_g electrons become localized when the hopping interaction is relatively small. The cause of the e_g electron localization is two-fold: one is electron correlation among t_{2g} electron and the e_g states, although e_g states are more strongly hybridized with the O 2p states. The other is the Jahn-Teller coupling of the e_g electron with the surrounding oxygen displacement. Such an electronic configuration has a tendency to distort its environment at the cost of elastic energy but it gains electronic energy which makes it stable. This is a consequence of the Jahn-Teller theorem which states that a cation with a ground state that is degenerate, but not a Kramers' doublet, may be stabilized by a distortion of the surroundings to some lower symmetry that removes the ground state degeneracy. This is shown schematically in Figure 2.2. The MnO_6 octahedra distort so as to give a two long and four short geometry about the MnO_6 , so the z^2 orbital is occupied and the x^2-y^2 orbital empty. These z^2 orbitals can and do order in the MnO_6 planes of

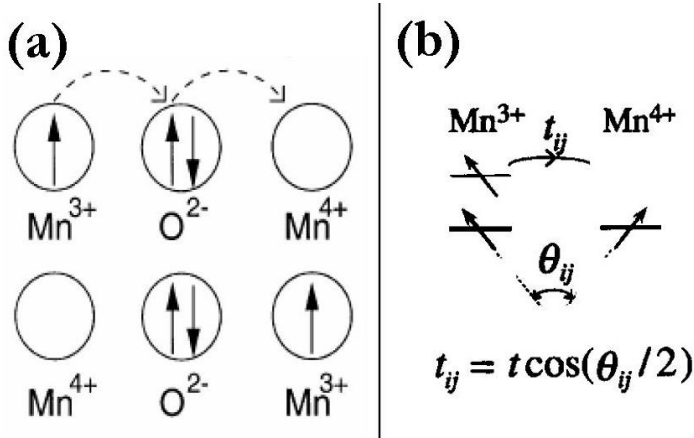


Figure 2.3: (a) A charge transfer in double exchange mechanism, (b) Transfer integral (hopping matrix), figure taken from ref. [13]

the structures so that long and short Mn-O bonds alternate in a "checkerboard" pattern. Thus, the orbital ordering in the manganites is always associated with a cooperative Jahn-Teller distortion.

2.1.3 Doped LaMnO₃ & double exchange mechanism

The undoped LaMnO₃ is an A-type antiferromagnetic (AAF) insulator, with an antiferromagnetic coupling in one (pseudocubic) direction and a ferromagnetic coupling in the planes orthogonal to this. Doping changes the magnetic order, the compound exhibits a mixed valence character, which results in a rich phase diagram.

The Mott insulator LaMnO₃ can be doped by divalent impurities to create electron vacancies or holes in the e_g orbital states of the crystal. This hole doping makes the Mn sublattice a mixture of Mn³⁺ and Mn⁴⁺. The e_g electrons escape from the long-range ordering and can become itinerant. They hop between Mn³⁺ ion and Mn⁴⁺ ion with the help of the oxygen in between. This process is called the double exchange mechanism.

The basic idea of double exchange (DE) as a mechanism for electrical conduction in the manganites was postulated by Zener [3]. In the initial model there was the simultaneous transfer of one electron from a manganese 3d e_g orbital to an oxygen 2p orbital and transfer from the same orbital to a manganese 3d e_g orbital on an adjacent ion as shown in Figure 2.3. In this way the e_g electrons are able to move throughout the lattice. Both electrons involved in the exchange must have the same spin (because of the Pauli exclusion principle). This leads to a ferromagnetic arrangement of the e_g electrons.

Further theoretical work was performed by Anderson and Hasegawa [4] and de Gennes [5]. In the limit of large Hund coupling, the spin of the e_g electron is tied

to the core t_{2g} spin and the hopping parameter t varies as

$$t_{ij} = b \left(\cos \frac{\theta_{ij}}{2} \right) (J_H \gg T) \quad (2.2)$$

where θ_{ij} is the angle between the core t_{2g} spins on adjacent manganese ions, which depends only on the relative orientation of the two spins and not their absolute direction with respect to the crystallographic axes [4]. The kinetic energy of the e_g electron is proportional to t_{ij} . Thus, in the DE model, if the manganese spins are arranged ferromagnetically then t_{ij} will be maximized and the electrons become itinerant. Therefore, ferromagnetism and metallicity are intimately linked. The basic DE model is in qualitative agreement with the experimental data. However, Millis *et al.* have shown that a Hamiltonian incorporating only the DE interaction cannot explain the change in magnitude of resistance at the metal-insulator transition [6]. A very strong electron-phonon coupling stemming from a Jahn-Teller splitting of Mn^{+3} ion, causes a local lattice distortion of the oxygen octahedra and traps the electron in the crystal lattice called polaron, resulting in increase in resistance at MI transition. A CMR effect where the large decrease in resistance under magnetic field occurs, can also be explained on basis of electron-phonon coupling. The localization of conduction band electrons as polaron can be turned off by the application of magnetic field, a significant decrease in resistance under magnetic field, as T is decreased through T_c , permitting the formation of a metallic state [7–10].

2.2 Phase diagram of $\text{La}_{1-x}\text{B}_x\text{MnO}_3$, $\text{B}=\text{Ca},\text{Sr}$.

As discussed before, the static collective Jahn Teller distortion present in LaMnO_3 is removed with increase in the doping level, and thereby the amount of Mn^{4+} . Introducing divalent Ca^{2+} or Sr^{2+} impurities therefore leads to different phases, with different conducting and magnetic regimes. This will be briefly sketched below, following the concentration x of the dopand atom, and the phase diagram given in Figure 2.4.

$x < 0.2$; insulating state

Increasing the doping to $x = 0.1$ does not change the A-type antiferromagnetic ground state qualitatively. A small net magnetic moment appears due to spin canting effects, or droplet-like phase separation. The material is insulating. Above, $x = 0.1$, the system becomes ferromagnetic, although still insulating. Apparently, although the e_g electron is mostly localized, it can already convey spin information to neighbor sites. The ferromagnetic transition temperatures T_c rises steeply with increasing doping, from 150 K to 250 K (Sr-doping) or 170 K (Ca-doping). In LCMO, the additional effects of charge ordering is found below 80 K. This is due to the larger Mn-O-Mn bond angles in the Ca-system.

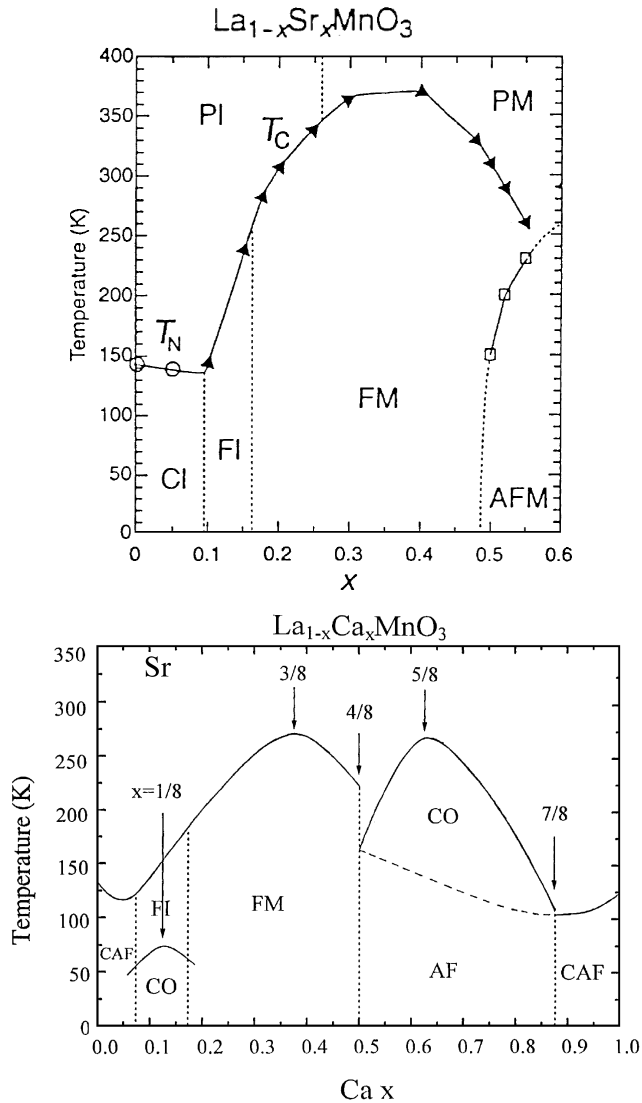


Figure 2.4: Phase diagram of (a) $\text{La}_{1-x}\text{Sr}_x\text{MnO}_3$ taken from references [11–13], (b) $\text{La}_{1-x}\text{Ca}_x\text{MnO}_3$ taken from reference [13]. They are constructed from measurements of macroscopic quantities such as the resistivity and magnetic susceptibility, reproduced from FM: Ferromagnetic Metal, FI: Ferromagnetic Insulator, AF: Antiferromagnetism, CAF: Canted AF, and CO: Charge/Orbital Ordering. FI and/or CAF could be a spatially inhomogeneous states with FM and AF coexistence.

0.2 > x < 0.5, the ferromagnetic metallic state

Doping beyond $x = 0.2$ leads to the formation of a band and a ferromagnetic metallic state (FM). T_c further increases to 350 K (LSMO) or 260 K (LCMO). The difference is again due to the difference in bond angles, leading to a larger band width for the Sr-doped system. The maximum in T_c is reached around $x = 0.3 - 0.35$. In the FM state, the distinction between Mn^{3+} and Mn^{4+} ions is lost, and the collective Jahn-Teller distortion has disappeared. Above T_c , where the material becomes paramagnetic and insulating, the residual conductance can be described by polaron hopping [7, 10], which means that (dynamic) lattice deformations are still present. This is the phase where Colossal Magnetoresistance occurs, because of the sensitivity of the electronic motion to the spin directions and therefore an applied magnetic field.

Lynn *et al.* used neutron scattering measurements to discover the formation of combined structural/magnetic polarons in LCMO cubic systems at the metal-insulator transition [14]. The formation of these nanoscale polarons truncates the ferromagnetic phase, and thus explains the first-order nature of the transition. These polarons form a well-defined thermodynamic glass phase above the ferromagnetic ordering temperature, which then melts into a polaron fluid at higher temperatures. They also suggested this polaron glass as an additional phase in the refinement of the phase diagram of LCMO.

x ≈ 0.5, Antiferromagnetic and charged ordered state

For the bulk material of LCMO, at $x=0.5$, two transitions are seen on cooling. A ferromagnetic state is initially entered at around 230 K. At lower temperatures, there is a transition to an antiferromagnetic state. The Neel temperature is approximately 135 K on cooling and 185 K on warming [15]. This thermal hysteresis is typical of a first-order phase transition in the presence of pinning. Additionally, phase coexistence between ferromagnetic and charge ordered phases has been seen in bulk samples of $\text{La}_{0.5}\text{Ca}_{0.5}\text{MnO}_3$ [16] and a charge-ordered ferromagnetic phase was observed at 90 K [17]. It therefore appears that the low-temperature boundary between the ferromagnetic and antiferromagnetic phases is not sharp and there is a mixed-phase region around $x = 0.5$.

0.5 > x < 1, the antiferromagnetic state

Values of x in the range $0.5 < x < 1$ give a charge-ordered (CO) insulator as the low-temperature ground state. In a CO state, the Mn^{+3} and Mn^{+4} ions arrange themselves into two distinct sub-lattices to form a series of stripes of the two types of ions [18]. Well ordered structures are formed when the ratio between Mn^{+4} and Mn^{+3} is integer, such as 1:1, 1:2 etc. For other levels of doping, the ordered structure comprises extra planes of one type of Mn ion to obtain the correct chemical composition [19]. There is an additional transition on further cooling, in which the manganese spins align themselves in an anti-parallel arrangement to form an antiferromagnet. This occurs in the range 100 - 150 K and the Neel temperature

T_N depends on the level of calcium doping. Neutron studies suggest that this phase is a CE type antiferromagnetic with a checkerboard arrangement of spins [2]. For LSMO, for $0.5 > x < 0.6$ an interesting A-type antiferromagnetic metallic state is stabilized.

2.3 Electronic transport in thin films of metallic manganites

$\text{La}_{1-x}\text{Ca}_x\text{MnO}_3$ and $\text{La}_{1-x}\text{Sr}_x\text{MnO}_3$ are interesting candidates to study the fundamental physics of the interplay between electronic, magnetic and lattice degree of freedom. This can lead to quite complicated phase diagrams, as shown above. Another dimension, however, is given by studying manganite thin films, which adds the effects of strain (by the substrate) and disorder to the other ingredients. Especially very thin films (20 nm and below) are of interest here. In this regime, strain can be uniform, electric fields can penetrate to a significant degree and the effects of the interface become important and can be studied. Different doping regimes can be of interest, and much work has been devoted to the regime around $x = 0.2$, on the border between the insulating and metallic states. Here, we concentrate on the more homogeneous regime around $x = 0.35$. This doping level gives the highest Curie temperatures, 370 K in bulk $\text{La}_{0.7}\text{Sr}_{0.3}\text{MnO}_3$ and 250 K in bulk $\text{La}_{0.7}\text{Ca}_{0.3}\text{MnO}_3$. In thin films these values are usually lower, as we shall see below, but the basic physics is the same. Figure 2.5 shows magnetoresistance and magnetization measurements of two films on SrTiO_3 (STO) substrates, of a 7 nm LSMO and a 9 nm LCMO film. The resistivity is seen to peak strongly at the onset of magnetization, which is the hallmark of the transition from the high temperature, semiconducting and polaron dominated regime to the low temperature ferromagnetic metallic regime. Note that the peak temperature T_p is close to the Curie temperature T_c , and can be taken as a measure for the latter. One of the focus point of this thesis is the possible connection between strain and the amount of carriers in the films. Below, we therefore briefly discuss the known effects of strain and the basis of the Hall effect, which can be used to measure the carrier density.

2.3.1 Effect of strain in thin films of manganites

The phase diagram shown in Figure 2.4 refers to bulk single crystalline materials. The properties of manganites can change in case of epitaxial thin films and additional effects can be studied as a function of thickness [21] or strain which can be either tensile or compressive, depending on the substrate [22].

The major effects of strain derive from the double exchange mechanism and its sensitivity to bond lengths and bond angles. Moreover, deformations of the oxygen octahedra reinforce the tendency to Jahn-Teller deformations. Generally, strain therefore leads to smaller bond lengths and lower Curie temperature. Strain can be induced by the lattice mismatch between substrate and film. If the lattice

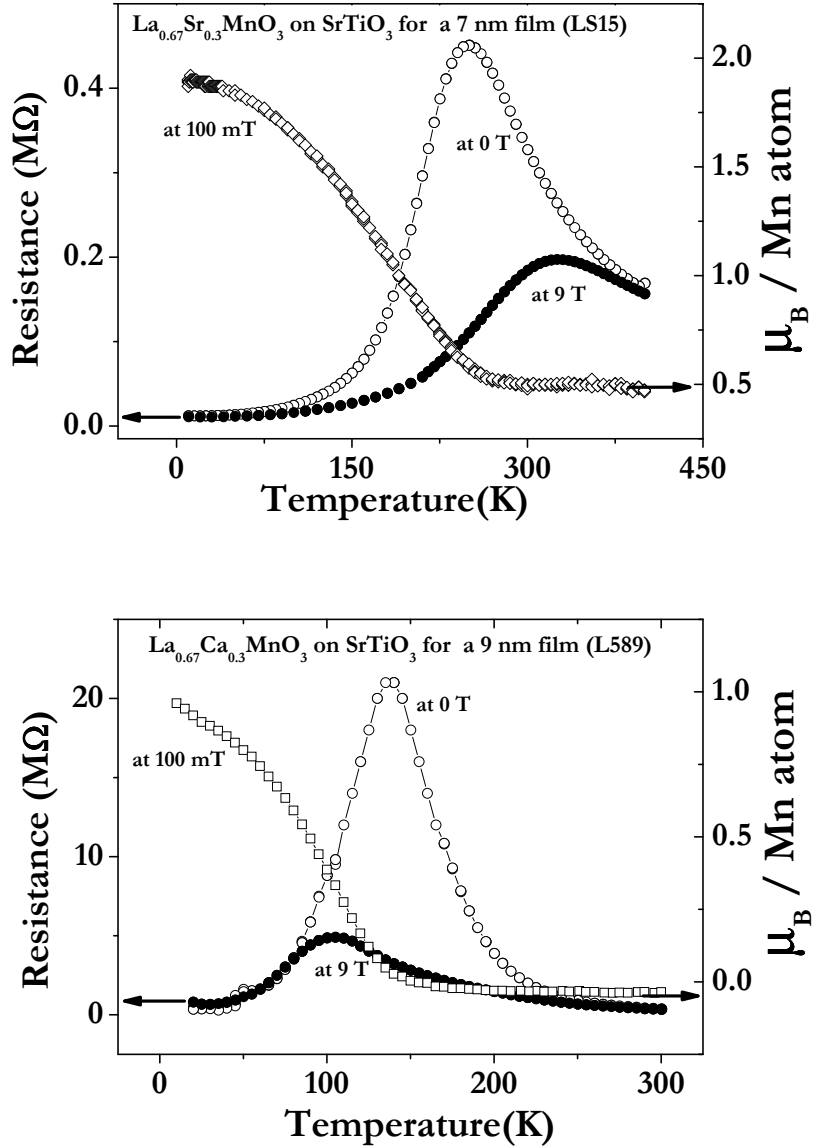


Figure 2.5: Transport and magnetic properties of thin films of (top) $\text{La}_{0.67}\text{Sr}_{0.33}\text{MnO}_3$ on SrTiO_3 for 7 nm, (bottom) $\text{La}_{0.67}\text{Ca}_{0.33}\text{MnO}_3$ on SrTiO_3 for 9 nm. Both are own data taken on sputter-grown films.

constant of the film is larger than that of the substrate, the strain is compressive. For the other way round, the strain is tensile. If the lattice constant of the film is larger than the substrate, it is compressive strain and if the lattice constant of substrate is larger than the film, it is tensile strain. The relevant parameter here is the mismatch f , given by

$$f = \frac{a^f - a^s}{a^s} \% \quad (2.3)$$

where a^f refers to the lattice constant of film, a^s for the substrate and 'f' is the mismatch.

The lattice strain has direct implication with Poisson's effect where the elastic properties of thin films propose a change between crystal axis and the bonds within the material lattice to accommodate the stress. When the bonds elongate in the direction of load/force/initial change, they shorten in the other directions. The same formalism in manganites is sensitive to both Mn-O bond distance (d_{Mn-O} and Mn-O-Mn bond angle (θ)). These parameters directly influence the case of electron hopping between Mn ions. Under the effect of strain, the slight changes in d_{Mn-O} and θ can also change the on-site coulomb correlation energy and/or bandwidth. This may lead to a metal-insulator transition/ferromagnetic ordering slightly suppressed as compared to the bulk material. Moreover, the co-operative nature of Jahn-Teller (JT) effect makes these materials much susceptible to strain.

2.3.2 On the critical thickness

Since this thesis will be much concerned with very thin films, it is relevant to mention here the issue of the critical thickness of manganite thin films, in particular LSMO and LCMO. It is generally found that bulk-like magnetic and electronic properties only develop beyond a certain (critical) thickness, resulting in a "dead layer" of a few nm. For a LSMO, early work of Sun *et al.* an electrically dead layer of about 3 nm (growth on NGO) to 5 nm (growth on LAO) was observed [23]. It was noted that, given the differences in lattice parameters, strain did not appear to be the driving factor. The issue was also discussed by Huijben *et al.*, who studied thin films of LSMO grown on STO (001) and found an electrically and magnetically dead layer of about 10 unit cells, or 4 nm [24]; and by Kim *et al.* who reported a critical thickness of 8 u.c's when growing on $(LaAlO_3)_{0.3} (SrAl_{0.5}Ta_{0.3}O_3)_{0.7}$ (LSAT), where strain is minimal [25]. Similar findings were reported for LCMO by Bibes *et al.* using nuclear magnetic resonance, found a layer of about 5 nm to nonferromagnetic and insulating when grown on STO [26]. Zanderbergen *et al.* found a critical thickness of about 6 nm [27], similar to de Andres *et al.*, growing on STO and NGO [28].

While dead layers are therefore well documented, their cause is not fully clear. At least three ingredients play a role. One is the oxygen content; one may be the presence of a polar discontinuity, which will be discussed later; one is the difference in structure which may occur in very thin films due to the lattice mismatch. It was shown by Yang *et al.* for instance, that the microstructure of very thin films of LCMO on STO is different from the bulk: the structure is 2-tilt rather than

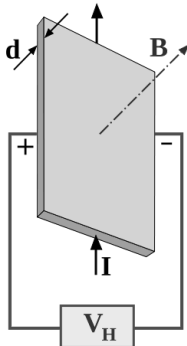


Figure 2.6: A schematic diagram to measure Hall voltage.

3-tilt [29]. Very recently, in a similar vein, it was shown that octahedra rotation in very thin films of LSMO on STO leads to special magnetic configuration around a thickness of 9 u.c or 3.5 nm [30].

2.3.3 Hall effect in manganites

The Hall effect is the voltage which appears as a result of current applied in a conductor under the influence of an applied magnetic field [31].

Figure 2.6 shows the experimental geometry to produce this effect. The setup is usually arranged such that the magnetic field, current and resulting Hall field are all perpendicular to each other. When an electric current flows through a conductor in a magnetic field, the field exerts a transverse force (Lorentz force) on the moving charge carriers which pushes them to one side of the conductor. A buildup of charge at the sides of the conductors will balance this magnetic influence, producing a measurable voltage between the two sides of the conductor, the Hall voltage. For a simple metal with a spherical Fermi surface and only one type of charge carrier (electrons) the Hall voltage V_H across a thin metallic plate is given by

$$V_H = -\frac{IB_z}{ned} \quad (2.4)$$

where I is the current across the plate length, B_z is the magnetic field perpendicular to the plate, d is the thickness of the plate, e is the elementary charge, and n is the charge carrier density. Denoting the current density by j_x , and the Hall electric field E_y , the quantity known as the Hall coefficient is then defined as

$$R_H = \frac{E_y}{j_x B_z} \quad (2.5)$$

By setting the force from the electric field equal to the Lorentz force, the Hall coefficient in the free electron approximation is given by

$$R_H = -\frac{1}{ne} \quad (2.6)$$

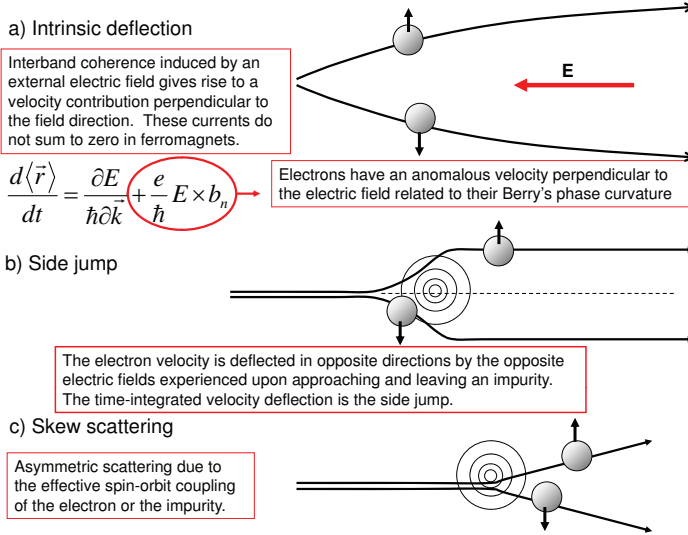


Figure 2.7: Three mechanisms of anomalous Hall effect. The figure is taken from reference [46].

This is used to determine the sign and number of charge carrier when only one type is involved, the one-band model. In semiconducting materials, both electrons and holes play a role, and since they reside in different bands, with different masses and mobilities, R_H is given by

$$R_H = \frac{n_h \mu_h^2 - n_e \mu_e^2}{e(n_h \mu_h + n_e \mu_e)^2} \quad (2.7)$$

where n_h is the carrier density of holes, n_e is the carrier density of electrons, μ_h is the mobility of holes and μ_e is the mobility of electrons.

Hall effect in ferromagnetic Materials

In ferromagnetic materials, there is an additional contribution to the Hall voltage caused by scattering of electrons from magnetic moments [32]. This extra term is proportional to the magnetization M of the sample [33]. This can be written as

$$\rho_H = \mu_0(R_H H_a + R_A M) \quad (2.8)$$

where now H_a is the applied magnetic field, R_H is the ordinary Hall co-efficient and R_A is the coefficient describing the so-called anomalous Hall effect (AHE).

The origin of the AHE is not trivial, and different ideas have been developed to explain this phenomenon. The first theoretical explanation of the AHE was given by Karplus and Luttinger and the AHE was considered to originate from spin-orbit interactions causing population imbalance of electronic spin states and asymmetric motion of electrons. The effect is intrinsic [35]. Smit *et al.* found that above treatment of the AHE is beyond the usual Boltzmann transport theory. He stated that impurity scattering is essential for the steady state and hence also for AHE [37]. That mechanism was named skew scattering. Skew scattering describes the average deflection of the trajectory of a charge carrier in a scattering event, and yields a contribution which is proportional to the Bloch state transport lifetime. It dominates more in nearly perfect crystals. After that Luttinger developed the systematic theory for AHE in the presence of the impurity scattering [36]. The third mechanism of the impurity-induced AHE, is the side jump model which was proposed by Berger [38,39]. He proposed that the center of mass of a wave packet undergoes a discontinuous and finite sideways displacement on scattering by a center potential, in the presence of spin orbit interaction. The asymmetric scattering of spin polarized electrons make skew scattering and side jump mechanisms as extrinsic AHE.

The two extrinsic terms can be related to the longitudinal resistivity as

$$\rho_{AH} = a\rho_{xx} + b\rho_{xx}^2 \quad (2.9)$$

The linear term on the right is called "skew scattering" and the quadratic is "side jumps" respectively. They both differ and depend by amount of disorder in the sample. The anomalous contributions to the Hall effect are shown in Figure 2.7. For a complete theoretical background, some reviews are given in Ref. [45,46].

2.4 Interfaces of complex oxides

Next to the electronic properties of very thin manganite layers, a significant part of this thesis is on the subject of the properties of an interface between the complex oxides. In particular, the issue of the formation of a two-dimensional electron gas (2DEG) at LAO/STO is investigated. The physics behind the formation of a two dimensional electron gas at the interface of the band insulators LaAlO₃ and SrTiO₃ is still subject to an ongoing debate even eight years after its discovery [47]. The basic idea is that polar LaAlO₃ on non-polar SrTiO₃, singly terminated by TiO₂, generates a high mobility quasi two-dimensional electron gas at the interface due to an electronic transfer mechanism (electronic reconstruction). The interface becomes conducting only when the LaAlO₃ thickness reaches a critical value of 1.6 nm (4 unit cells of LaAlO₃) and SrTiO₃ is singly terminated by TiO₂ [48,49]. These observations have mostly been made on samples grown by Pulsed Laser Deposition (PLD).

In this section, we give a brief summary of existing work on LAO/STO interfaces. We review the basic properties and discuss the mechanisms which have been claimed to be responsible for the observed conductance at the interface.

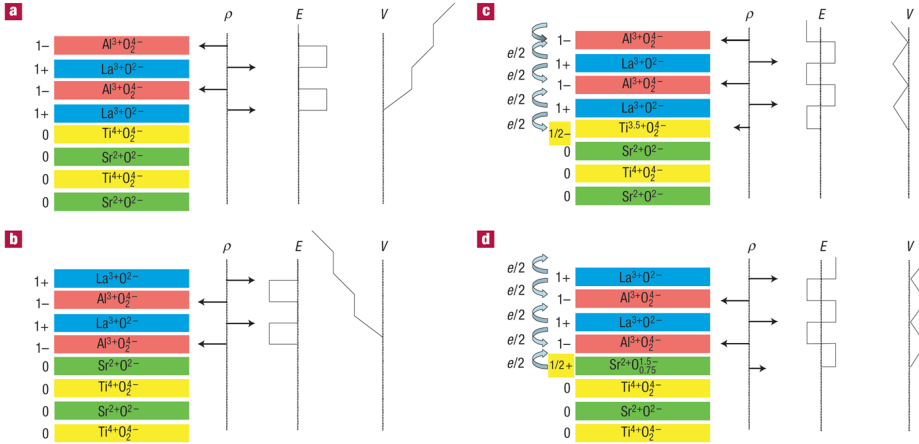


Figure 2.8: An intrinsic electronic reconstruction to avoid polar catastrophe for LAO/STO interfaces, adapted from Ref. [58]

2.4.1 Intrinsic Electronic reconstruction

The pioneering work to make conducting interfaces of LaAlO_3 and SrTiO_3 was that of Ohtomo and Hwang using pulsed laser deposition [47]. Both constituents are conventional band insulators but they differ in layer-to-layer charge variation. The interface therefore shows a charge discontinuity, the so-called polar discontinuity or catastrophe.

The intrinsic electronic reconstruction which arises from the polar catastrophe can be understood with the help of figure 2.8 where alternating layers of polar LAO (LaO^+ , AlO_2^-) and non-polar STO (SrO , TiO_2) are stacked. The charged layers can be considered as parallel plates of capacitors. The potential across each capacitor (each layer of LAO) is additive and should increase with increasing number of plates (LAO layers). To avoid a diverging potential, half an electron should be compensated at the interface. This doping allows the reconstructed interfaces to be n-type (charge carriers; electrons) or p-type (charge carriers; holes). However, only the n-type interface is found to be conducting while p-type is insulating. The valence change of Ti from Ti^{+4} to Ti^{+3} allows the construction of n-type interface.

Critical thickness for LaAlO_3 films

The same study raised another interesting observation on the minimum thickness of the LaAlO_3 film before mobile carriers and conductivity are observed at the n-type interface. This critical thickness is 4 unit cells on samples grown in a background oxygen pressure of 1.3×10^{-4} mbar [47]. The interface is insulating below this thickness. Thiel *et al.* [48] showed that after annealing, the sheet carrier density n_s for samples grown at the same pressure with fewer than 4 unit cells of LaAlO_3

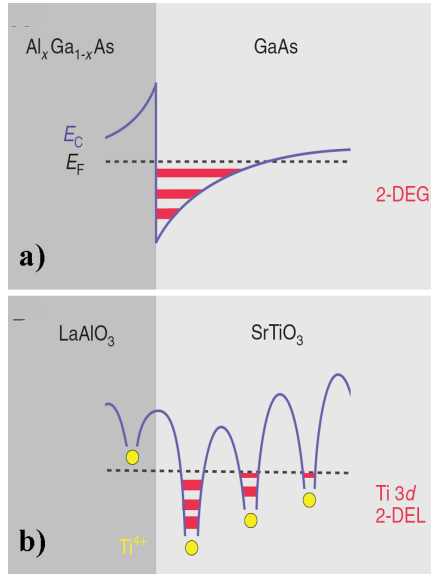


Figure 2.9: (a and b) Comparison between two-dimensional electron systems generated at interfaces between standard semiconductors, for example, between GaAs and $\text{Al}_x\text{Ga}_{1-x}\text{As}$ (a) and between LaAlO_3 and SrTiO_3 (b) taken from Ref. [53].

is below detectable levels. Above 4 unit cells, they observe a step-like jump in n_s but the value of the sheet carrier density is smaller than the theoretical value of $0.5 e/a_{\text{STO}}^2$ or $3.3 \times 10^{14} \text{cm}^{-2}$. The small sheet carrier densities suggest that not all electrons are participating in the transport. Huijben *et al.* [51] grew n-type interface samples with pressure of oxygen 10^{-5} mbar without annealing and observed that the samples are conducting for all LaAlO_3 thickness studied.

The sheet carrier density starts out small but finite for 1 u.c of LaAlO_3 and it increases with LaAlO_3 thickness until it saturates at $1.4 \times 10^{14} \text{cm}^{-2}$ for ≥ 6 u.c of LaAlO_3 . A theoretical study [52] on this issue favors the polar-nonpolar mechanism to be already valid for a one unit cell LaAlO_3 film, but in growing LaAlO_3 on SrTiO_3 may need some sacrificial layers to compensate surface defects and before the interface becomes conductive at 4 unit cells of LaAlO_3 .

Band offset and band-bending

As intrinsic electronic reconstruction on oxide interfaces would be followed by band bending and band offset like semi-conducting interfaces. Scanning tunnelling spectroscopy measurements of the density of states at the LaAlO_3 - SrTiO_3 interface [53] revealed remarkable differences between this two-dimensional electron system and the 2DEGs formed at interfaces between conventional semiconductors. As sketched in Figure 2.9a, at the semiconductor interface the mobile electrons move in two-dimensional subbands within the quantum well generated by band bending. At

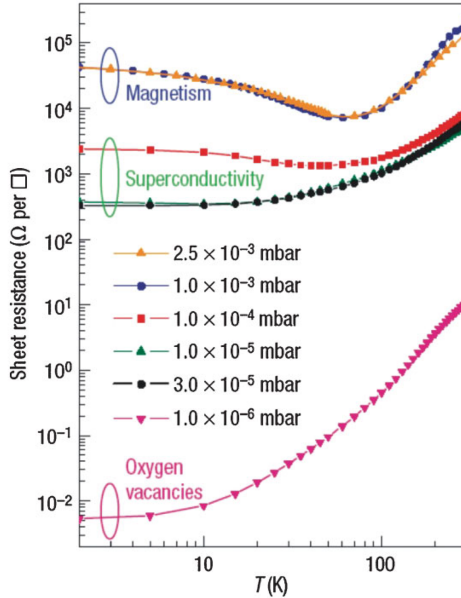


Figure 2.10: Conductivity of LAO/STO interface changing with background oxygen pressure and temperature, taken from Ref. [57]

the oxide interface, however, there are multiple quantum wells given by the ionic potentials of the TiO_6 octahedra, and within each quantum well are subbands that are a subset of the Ti 3d states (Figure 2.9b). In these bands, the electrons are subject to the correlations of the Ti 3d orbitals and form a two dimensional electron liquid rather than an electron gas.

2.4.2 Oxygen Vacancies

SrTiO_3 as a substrate is very sensitive to disturbances such as annealing or argon ion bombardment. In particular, the role of oxygen vacancies at the interface of LAO/STO is crucial. Pulsed laser deposition is a low pressure technique where the intensity of the plasma changes with the background pressure. In the case of conducting interfaces of LaAlO_3 and SrTiO_3 , this background oxygen pressure has significant effects on the conductivity [54]. A low growth pressure results in high conductivity and vice versa. Ohtomo & Hwang [47] discussed the possibility of oxygen vacancies forming at low pressures (10^{-6} mbar) but excluded them above 10^{-4} mbar. They argued that the substrate remains non-conducting while subjected to the growth conditions without growing films, and if oxygen vacancies would be the origin then p-type interface should also be conducting. The reasoning is not enough to exclude the possibilities of oxygen vacancies since their role may be the facilitator rather than the generator.

The properties of interfaces can be related to four different regions of oxygen pressure; (i) a three dimensional bulk conductivity is observed at an oxygen pressure of 10^{-6} mbar. It is agreed that this pressure produces oxygen defects in SrTiO₃ which in turn enhance the conductivity [47], (ii) two dimensional conductivity around $pO_2 = 10^{-4}$ mbar where superconductivity effects [61] are observed at 200 mK, (iii) still a two dimensional conductivity but magnetic effects [57] are observed at 10^{-3} mbar and (iv) a badly conducting interface at high oxygen pressure, 10^{-2} mbar [55,56]. This suggests that the background oxygen pressure plays a key role in the conductances of the interface and the above trend shows that even higher pressure should further decrease the conductance. Figure 2.10 gives an overview of resistance versus temperature behavior in the different regimes.

The reduction of STO was thoroughly studied by Scullin *et al* [65]. It was shown that annealing (450°C, 10^{-7} torr, 10 - 60 minutes) reduces an STO (001) substrate roughly over 5 nm into the crystal, but that the same crystals are reduced throughout their 500 μ m thickness when coupled with PLD. So, a question is whether the most often used PLD growth parameters of LAO films on STO (750°C - 850°C, 10^{-5} - 10^{-3} torr) would be enough to reduce STO substantially beyond the interface (thickness 1 nm), and so facilitate the conduction at the interface.

2.4.3 Intermixing Effects

The idea of an abrupt interface came to an end when Nakagawa *et al.* [58] found that the n-type interface is significantly rougher than p-type interface, using atomic-resolution electron energy loss spectroscopy (EELS). They suggested that the electronic dipole energy connected with the finite width of the electron gas can be reduced by exchanging Sr with La across the interface. Willmott [59] analyzed the interface structure using Coherent Bragg rod (COBRA) analysis combined with DFT calculations and concluded that the interface is not abrupt but shows a graded intermixing over 3 unit cells. Sr and La intermix at a greater depth (~ 6 Å further away from interface) than Ti and Al ions because of larger radii and form two monolayers of La_{1-x}Sr_xTiO₃. This intermixing is largely accepted to exist. Recently, Chambers [52] measured the intermixing effects at the interface by Rutherford backscattering, time of flight secondary ion mass spectrometry and electron energy loss spectroscopy. He found that including intermixing effects is essential to correctly model the outcomes of these techniques to account for the electric properties of interfaces. The question still remains what procedures could reduce such intermixing to create ideal interfaces.

2.4.4 Conducting interfaces made by MBE and cationic stoichiometry

All mechanisms discussed in the previous paragraphs have been studied on interfaces made by PLD. Interfaces grown by molecular beam epitaxy raised the issue of cation stoichiometry. This issue is not touched upon in PLD-grown interfaces till date.

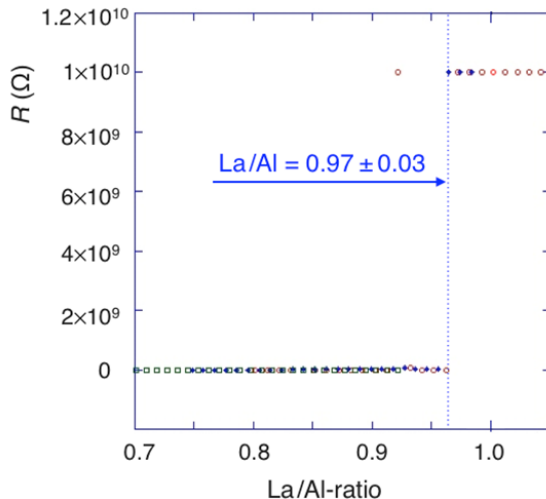


Figure 2.11: The ratio of La and Al versus resistance of the interface. Taken from Ref. [60].

In an MBE chamber, $\text{La}_{1+x}\text{Al}_{1-x}\text{O}_3$ films were grown by depositing La and Al from oppositely positioned effusion cells. Conductivity, film composition by RBS and interface structure and composition by HRTEM/EELS was measured as x was systematically changed between 0.1 and -0.1. It was found that conductivity occurs only in Al-rich films for which the La/Al atom ratio is 0.97 or less. Moreover, all HRTEM/EELS specimens showed some La diffused into the STO although not all were conducting.

For the RBS analysis, in order to move the Al RBS peak away from the substrate backscattering, STO films were grown on MgO (111) substrates and then the LAO film was grown on STO thin films. This procedure allowed the Al concentration to be measured with higher accuracy than when LAO is grown directly on bulk STO (001). This investigation strongly suggests that defects associated with non stoichiometry in the Al-rich direction may be required to activate conductivity.

2.4.5 Oxide interfaces versus semiconductors and devices

The physical phenomena which plays a role at oxide interfaces have more dimensions than conventional semiconductor interfaces. First the nature of interactions is different between the constituent electrons in interfaces of oxides and semiconductors. The electronic states of semiconductors are well described by single particle band theory. In complex oxides, however, there are strong correlations between the tightly bound transition metal d electrons and d-electrons can no longer independent but influence the behavior of all other electrons in the crystal. At interfaces in strongly correlated systems, the correlation parameters may be changed to values that are unachievable in the bulk. This complex character of the participant

materials makes it difficult to an intrinsic polar-nonpolar nature for the 2DEG as in semiconductors .

The key factors controlling the electronic behavior at oxide interfaces are ionicity, oxygen, electronic correlations and reconstruction [66]. Due to strong ionic character of oxides, the electronic orbitals tend to overlap less than the hybridized s-and p-orbitals which are characteristic of standard semiconductors. The characteristic bandwidth of oxides is less and effective masses exceed those of semiconductors, which enable the carriers to become localized. O^{2-} ions are quite polarizable, typically causing a large, nonlinear, and nonuniform polarizability of the lattice. Because the carrier density at oxide interfaces is high (10^{13} to $10^{14}/\text{cm}^2$, as opposed to the 10^{11} to $10^{12}/\text{cm}^2$ found in semiconductor heterostructures), this polarizability often leads to electrostatic screening lengths in complex oxides of 1 to 10 nm, which are smaller than typical screening lengths in semiconductors. This gives rise to more local and more confined novel interfacial properties which holds promise for smaller densities. Oxygen is also special because holes in the oxygen 2 p band may give rise to magnetism.

The two dimensional electron to be gas at oxides interfaces attract more interest due to its superconductivity behavior at 200 mK [61] and magnetism [57]. The flow of electrons can be controlled by an external electric field [48,62] analogous to conventional transistors. The possibility to ‘write’ and ‘erase’ conducting wires at the interface between LAO and STO with the tip of an atomic force microscope (AFM) [67], taking the first step towards highly dense nanodevices. The combination of all these properties in interfaces of oxides (totally different from the bulk) not only developed interest to understand its fundamental physics but also helped to improve technological applications. A variety of two dimensional electron systems can be stabilized at the oxide interfaces, exploiting spin, charge and orbital interaction as well as lattice vibrations. It was immediately realized that it can be the next generation of silicon based devices although achieving the mobility levels and purity seen in semiconductor heterostructures still remains a challenge. The confined electrons at the interface can be used to excite multiple electron and thus a step towards new type of solar cells [68].

Bibliography

- [1] J.B. Goodenough and J.M. Longo, *Magnetic and Other Properties of Oxides and Related Compounds*, Landolt-Bornstein, Vol. 4(Springer-Verlag, New York, 1970).
- [2] E.O. Wollan and W.C. Koehler, *Phys. Rev.* **100**, 545 (1955).
- [3] C. Zener, *Phys. Rev.* **82**, 403 (1951).
- [4] P.W. Anderson and H. Hasegawa, *Phys. Rev.* **100**, 675-81 (1955).
- [5] P.-G. de Gennes, *Phys. Rev.* **118**, 141-54 (1960).
- [6] A.J. Millis, P.B. Littlewood and B.I. Shraiman, *Phys. Rev. Lett.* **74**, 5144 (1995).
- [7] A.J. Millis, B.I. Shraiman, R. Mueller, *Phys. Rev. Lett.* **77**, 175 (1996).
- [8] H. Roder, J. Zang, and A.R. Bishop, *Phys. Rev. Lett.* **76**, 1356 (1996).
- [9] J.-S. Zhou, J.B. Goodenough, *Phys. Rev. Lett.* **80**, 2665 (1998).
- [10] A.J. Millis, *Nature* **392**, 147 (1998).
- [11] A. Urushibara, Y. Moritomo, T. Arima, A. Asamitsu, G. Kido, Y. Tokura, *Phys. Rev. B* **51**, 14 103 (1995).
- [12] H. Fujishiro, *J. Phys. Soc. Japan.* **67**, 1799 (1998).
- [13] Y. Tokura, *Colossal Magnetoresistive Oxides*, Vol. 2, Gordon & Breach Science publishers, 2000.

- [14] J.W. Lynn, D.N. Argyriou, Y. Ren, Y. Chen, Y.M. Mukovskii, and D.A. Shulyatev, *Phys. Rev. B* **76**, 014437 (2007).
- [15] J. Dho, I. Kim, S. Lee, K.H. Kim, H.J. Lee, J.H. Jung and T.W. Noh, *Phys. Rev. B* **59**, 492 (1999).
- [16] P. Levy, F. Parisi, G. Polla, D. Vega, G. Leyva, H. Lanza, R.S. Freitas and L. Ghivelder, *Phys. Rev. B* **62**, 6437 (2000).
- [17] J.C. Loudon, N.D. Mathur and P.A. Midgley, *Nature* **420**, 797 (2002).
- [18] C.H. Chen, S.-W. Cheong and H.Y. Hwang, *J. Appl. Phys.* **81**, 4326 (1999).
- [19] S. Mori, C.H. Chen and S.-W. Cheong, *Nature* **392**, 473 (1998).
- [20] Y. Moritomo, T. Akimoto, A. Nakamura, K. Ohoyama, M. Ohashi, *Phys. Rev. B* **58**, 5544 (1998).
- [21] M. Bibes, S. Valencia, Ll. Balcells, B. Martínez, J. Fontcuberta, M. Wojcik, S. Nadolski, and E. Jedryka, *Phys. Rev. B* **66**, 134416 (2002).
- [22] P. Dey, T.K. Nath, A. Taraphder, *Appl. Phys. Lett.* **91**, 012511 (2007).
- [23] J.Z. Sun, D.W. Abraham, R.A. Rao, and C. Eom, *Appl. Phys. Lett.* **74**, 3017 (1999).
- [24] M. Huijben, L.W. Martin, Y.-H. Chu, M.B. Holcomb, P. Yu, G. Rijnders, D.H.A. Blank, and R. Ramesh, *Phys. Rev. B* **78**, 094413 (2008).
- [25] B. Kim, D. Kwon, T. Yajima, C. Bell, Y. Hikita, B.G. Kim, and H.Y. Hwang, *Appl. Phys. Lett.* **99**, 092513 (2011).
- [26] M. Bibes, Ll. Balcells, S. Valencia, J. Fontcuberta, M. Wojcik, E. Jedryka, and S. Nadolski, *Phys. Rev. Lett.* **87**, 067210 (2001).
- [27] H.W. Zandbergen, S. Fresien, T. Nojima, and J. Aarts, *Phys. Rev. B* **60**, 10259 (1999).
- [28] A. de Andrés, J. Rubio, G. Castro, S. Taboada, J.L. Martínez, and J.M. Colino, *Appl. Phys. Lett.* **83**, 713 (2003).
- [29] Z.Q. Yang, R. Hendrikx, J. Aarts, Y. Qin, and H.W. Zandbergen, *Phys. Rev. B* **67**, 024408 (2003).
- [30] H. Boschker, J. Kautz, E.P. Houwman, W. Siemons, D.H.A. Blank, M. Huijben, G. Koster, A. Vailionis, and G. Rijnders, *Phys. Rev. Lett.* **109**, 157207 (2012).
- [31] E.H. Hall, *Philos. Mag.* **10**, 301 (1880).
- [32] E.H. Hall, *Philos. Mag.* **12**, 157 (1881).

-
- [33] A.W. Smith, R.W. Sears, *Phys. Rev.* **34**, 1466 (1929).
- [34] N. Nagaosa, J. Sinova, S. Onoda, A.H. MacDonald, N.P. Ong, *Rev. Mod. Phys.* **82**, 1539 (2010).
- [35] R. Karpus, J.M. Luttinger, *Phys. Rev.* **95**, 1154 (1954).
- [36] J. M Luttinger, *Phys. Rev.* **112**, 739 (1958).
- [37] J. Smit, *Physica* **24**, 39 (1958).
- [38] L. Berger, *Phys. Rev. B* **2**, 4559 (1970).
- [39] L. Berger, *Phys. Rev. B* **5**, 1862 (1972).
- [40] G. Sundaram and Q. Niu, *Phys. Rev. B* **59**, 14915 (1999).
- [41] A. Langenfeld and P.Wölfe, *Phys. Rev. Lett.* **67**, 739 (1991).
- [42] K.A. Muttalib and P.Wölfe, *Phys. Rev. B* **76**, 214415 (2007).
- [43] V.K. Dugaev, A. Crépieux, and P. Bruno, *Phys. Rev. B* **64**, 104411 (2001).
- [44] H. Meier, M.Y. Kharitonov, and K.B. Efetov, *Phys. Rev. B* **80**, 045122 (2009).
- [45] N. Nagaosa, *J. Phys. Soc. Jpn.* **75**, 042001 (2006).
- [46] N. Nagaosa, J. Sinova, S. Onoda, A.H. MacDonald, N.P. Ong, *Rev. Mod. Phys.* **82**, 1539 (2010).
- [47] O. Ohtomo, H.Y. Hwang, *Nature* **427**, 423 (2004).
- [48] S. Thiel, G. Hammert, A. Schmehl, C.W. Schneider, J. Mannhart, *Science* **313**, 1942 (2006).
- [49] C. Bell, S. Harashima, Y. Hikita, and H.Y. Hwang, *Appl. Phys. Lett.* **94**, 222111 (2009).
- [50] M. Huijben, A. Brinkman, G. Koster, G. Rijnders, H. Hilgenkamp and D.H.A. Blank, *Adv. Mat.* **21**, 1665 (2009).
- [51] M. Huijben, G. Rijnders, D.H.A. Blank, S. Bals, S. van Aert, J. Verbeeck, G. Tendeloo, A. Brinkman, and H. Hilgenkamp, *Nature* **5**, 556 (2006).
- [52] S.A. Chambers, M.H. Engelhard, V. Shutthanandan, Z. Zhu, T.C. Droubay, L. Qiao, P.V. Sushkob, T. Feng, H.D. Lee, T. Gustafsson, E. Garfunkel, A.B. Shah, J.-M. Zuo, Q.M. Ramasse, *Surf. Sci. Rep.* **65**, 317 (2010).
- [53] M. Breitschaft, V. Tinkl, N. Pavlenko, S. Paetel, C. Richter, J.R. Kirtley, Y.C. Liao, G. Hammerl, V. Eyert, T. Kopp, and J. Mannhart, *Phys. Rev. B* **81**, 153414 (2010).

- [54] A. Kalabukhov, R. Gunnarsson, J. Borjesson, E. Olsson, T. Claeson, D. Winkler, Phys. Rev. B **75**, 121404(R) (2007).
- [55] A. Kalabukhov, Y.A. Boikov, I.T. Serenkov, V.I. Sakharov, J. Borjesson, N. Ljustine, E. Olsson, D. Winkler and T. Claeson, Euro. Phys. Lett. **93**, 37001 (2011).
- [56] C. Cancellieri, N. Reyren, S. Gariglio, A.D. Caviglia, and J.-M. Triscone, Euro. Phys. Lett. **91**, 17004 (2010).
- [57] A. Brinkman, M. Huijben, M. van Zalk, J. Huijben, U. Zeitler, J.C. Maan, W.G. van der Wiel, G. Rijnders, D.H.A. Blank, and H. Hilgenkamp, Nature Mater. **6**, 493 (2007).
- [58] N. Nakagawa, H.Y. Hwang and D.A. Muller, Nature Mater. **5**, 204 (2006).
- [59] P.R. Willmott, S.A. Pauli, R. Herger, C.M. Schleputz, D. Martocchia, B.D. Patterson, B. Delley, R. Clarke, D. Kumah, C. Cionca and Y. Yacoby. Phys. Rev. Lett. **99**, 155502 (2007).
- [60] M.P. Warusawithana, A.A. Pawlicki, T. Heeg, D.G. Schlom, C. Richter, S. Paetel, J. MANNHART, M. Zheng, B. Mulcahy, J.N. Eckstein, W. Zander, and J. Schubert, Bulletin of the APS **55**, nr. 2 (2010), abstract ID BAPS.2010.MAR.B37.1.
- [61] N. Reyren, S. Thiel, A.D. Caviglia, L.F. Kourkoutis, G. Hammerl, C. Richter, C.W. Schneider, T.H. Kopp, A.-S. Ruetschi, D. Jaccard, M. Gabay, D.A. Muller, J.-M Triscone, J. Mannhart, Science **317**, 1196 (2007).
- [62] A.D. Caviglia, S. Gariglio, N. Reyren, D. Jaccard, T. Schneider, M. Gabay, S. Thiel, G. Hammerl, J. Mannhart, and J.-M. Triscone, Nature **456**, 624 (2008).
- [63] G. Herranz, M. Basletic, M. Bibes, C. Carretero, E. Tafra, E. Jacquet, K. Bouzouane, C. Deranlot, A. Hamzic, J.- M. Broto, A. Bathelemy, and A.Fert, Phys. Rev. Lett. **98**, 216803 (2007).
- [64] W. Siemons, G. Koster, H. Yamamoto, W.A. Harrison, G. Lucovsky, T.H. Geballe, D.H.A. Blank and M.R. Beasley, Phys. Rev. Lett. **98**, 196802 (2007).
- [65] M.L. Scullin, J. Ravichandran. C. Yu, M. Huijben, J. Seidel, A. Majumdar, R. Ramesh, Acta Materialia **58**, 457 (2010).
- [66] J. Mannhart, D.G. Schlom, Science **327**, 1607 (2010).
- [67] C. Cen, S. Thiel, C.W. Schneider, K.E. Andersen, C.S. Hellberg, J. Mannhart, J. Levy, Nature Mat. **7**, 298 (2008).
- [68] J. Heber, Enter the oxides, Nature **459**, 28 (2009).

Sample fabrication and characterization

In the previous chapter, we have discussed the fundamental physics and the phase diagram of manganites, their sensitivity to the amount of doping, choice of substrate and micro structuring. Also, the interfaces between LaAlO_3 and SrTiO_3 were described as interesting candidates to study the physical properties of interfaces and reasons for the conduction at the interfaces. Such studies demand a high quality growth of the materials. After growth, the films should be characterized to confirm their crystalline quality, morphology and most important for LaAlO_3 and SrTiO_3 , the interfaces. In this chapter, we give details of the deposition, information on targets and substrates, techniques used to characterize thin films.

Section 3.1 describes the sputter process and geometry, and discusses targets and substrates. Section 3.2 describes the characterization of the films by AFM (surface) and X-ray diffraction (bulk structure). Optical and electron beam lithographic techniques are described in section 3.4. The transport properties of films were measured by a physical properties measuring system (PPMS). Magnetic properties of films were measured by a SQUID-based magnetic properties measuring system (MPMS), described briefly in section 3.5. In the last section of the chapter, 3.6, we discuss the degradation of LCMO targets and a remedy to prolong its life time.

3.1 Sputtering

We used DC and RF sputtering techniques to grow the films which are studied in this thesis. Here we briefly describe them, including a discussion on the targets and substrates which were used.

3.1.1 DC and RF reactive sputtering

In reactive DC and RF sputtering of oxide materials, oxygen as a molecular gas incorporates in the growth process and compensates the deficiency of oxygen in the growing films. In normal DC sputtering, a dc power is applied between the cathode (target material) and anode (substrate) to ionize the argon gas. The newly formed Ar^+ ions accelerate towards the negatively charged cathode and a process of cascade ionization enables to sputter the target material. Ionization of molecular gases yields a negative valency which can cause backsputtering of the substrate. This can be avoided by choosing a high process pressure. The long path lengths of the ions to the substrate facilitates scattering and thermalization, and allow for on-axis sputtering. Off-axis sputtering can be used for the reactive gases even at low growth pressures [1].

Depending on the target material either DC or RF sputtering may be used. For a conducting target material, a constant voltage is used to accelerate the ions to the desired velocity. As the ions strike the surface, the resulting charges can move freely about the material to prevent any charge buildup. However, if the material is an insulator, as the ions strike the surface, their charge will remain localized and over time the charge will build up, making it impossible to further bombard the surface. In order to prevent this, alternating current is used at a frequency above 50 kHz. A high frequency is used so that the heavy ions cannot follow the switching fast enough and only electrons hit the surface to neutralize charge.

We used reactive DC sputtering to grow $\text{La}_{0.7}\text{Sr}_{0.3}\text{MnO}_3$ and $\text{La}_{0.7}\text{Ca}_{0.3}\text{MnO}_3$ thin films at high oxygen pressure of 3 mbar and 2.2 mbar. RF reactive sputtering was used to grow insulating LaAlO_3 films at 0.8 mbar (optimized pressure). Oxygen is used as reactive gas for both DC and RF sputtering.

3.1.2 Targets, substrates and thin film growth process

Targets

Conducting targets with nominal composition of $\text{La}_{0.7}\text{Sr}_{0.3}\text{MnO}_3$ (LSMO), $\text{La}_{0.7}\text{Ca}_{0.3}\text{MnO}_3$ (LCMO) and non-conducting LaAlO_3 (LAO) targets were purchased from commercial companies with a purity of 99.9% and density better than 96%. All materials, LSMO (the bulk lattice constant a_c is 3.863 Å), LCMO ($a_c = 3.873$ Å) and LAO ($a_c = 3.79$ Å) belong to the family of perovskites. For the growth of LAO films, we used stoichiometric and non-stoichiometric targets to try to vary the amount of aluminum in the respective films. The stoichiometric target is $\text{La}_1\text{Al}_1\text{O}_3$ and the non-stoichiometric target is $\text{La}_{0.94}\text{Al}_{1.06}\text{O}_3$. For the best epitaxial match with the films, perovskites substrates are used. The almost inevitable mismatch between film and substrate leads to strain as given in Table 3.1.

Substrates

SrTiO_3 (STO hereafter) (001) is a standard perovskite substrates used for the growth of manganites. The high dielectric constant of STO make them very use-

ful for gating experiments. The mismatch between LSMO, LCMO and LAO films with STO substrate gives tensile strain. The commercially available STO substrates have surfaces with equal amounts of SrO (AO) and TiO₂ (BO₂) - terminated domains separated by half unit-cell steps. Figure 3.1a shows as received STO which has mixed termination of both SrO and TiO₂ top layers. A line-profile of an untreated substrate (Figure 3.1b) gives a variation of about 0.2 nm. Such mixed terminated STO substrates are used to grow LSMO and LCMO films.

To study interfaces between LaAlO₃ and SrTiO₃, the growth should be controlled on the atomic scale and it is possible when the initial surface of the substrate is atomically smooth. To fabricate a single type interface, one layer of the initial substrate has to be terminated by either SrO or TiO₂. A thermal and chemical treatment is used to form perfectly crystalline TiO₂-terminated SrTiO₃ surfaces [2, 3]. Singly terminated TiO₂ surface shows unit cell step height (Figure 3.1d), the steps are clearly visible in Figure 3.1c. The single-terminated SrO surfaces can best be obtained by deposition of a SrO monolayer on a single terminated TiO₂ surface [4, 5]. In this thesis, only TiO₂-terminated surfaces are used and they were treated in TSST B.V, Enschede, the Netherlands.

Neodymium Gallate, NdGaO₃ offers less strain when compared to the SrTiO₃ substrate. The lattice parameters for the orthorhombic cell are $a = 5.426 \text{ \AA}$, $b = 5.502 \text{ \AA}$, $c = 7.706 \text{ \AA}$ while for a perovskite-related cell $a = b = 3.864 \text{ \AA}$; $c = 3.853 \text{ \AA}$, $\gamma_p = 89^\circ$ [6]. Strontium Lanthanum Gallate (SrLaGaO₄) has a tetragonal structure with $a = b = 3.843 \text{ \AA}$ and $c = 12.68 \text{ \AA}$ and it is slightly compressive LSMO and LCMO films. Lanthanum Aluminate, LaAlO₃ offers compressive strain and can also be represented as pseudocubic with $a = 3.793 \text{ \AA}$. We will use the cubic indexing for LAO in this thesis ($a_c = 3.79 \text{ \AA}$).

Substrate/Thin films	LSMO 3.873 Å	LCMO 3.863 Å	LAO 3.79 Å
STO (3.905 Å)	-0.82%	-1.07%	-2%
NGO (3.851 Å)	0.6%	0.3%	x
LSGO (3.843 Å)	0.78%	0.52%	x
LAO (3.79 Å)	2.2%	1.9%	0%

Table 3.1: Strain between substrates and thin films with respect to the bulk lattice constants. The cross sign represents that this combination of film and substrates is not used in this thesis.

The nomenclature

It will be useful to define the nomenclature which we shall use in the rest of the thesis to refer to films and their respective substrates. The thin films of LSMO are indicated by LS, in brackets we shall put the thickness in nanometer, $LS(21)$ and the substrate is put in the subscript, $LS(21)_{STO}$. The thin films of LCMO are denoted with L and LAO as LA.

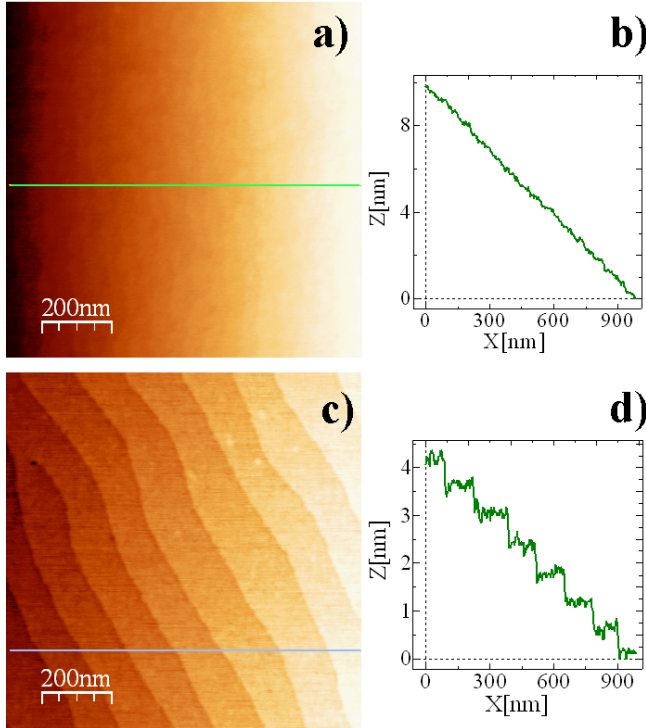


Figure 3.1: Surface analysis of STO substrate by atomic force microscopy (AFM). Untreated STO substrate is shown in (a) and its profile in (b). Parts (c) and (d) show a treated STO substrate. The profile (d) indicates the unit cell step height.

Thin film growth process

A schematic front view of the sputtering system is shown in Figure 3.2. A rotary feedthrough is connected to the center of the top flange, which can be lifted up by an electrical motor. A cross-piece with electrical and water feedthroughs, a plate with quartz crystal and heater element are connected to the rotary feedthrough. The substrate heater is surrounded by a cooling shroud to prevent the system and the temperature sensitive pressure gauges from temperature fluctuations. Four sputtering guns are mounted facing upward and the substrate heater can be rotated to be on-axis with the each available cathode [7].

The substrate is glued on heater with a conducting silver paste. The silver paste remains conducting at high temperatures with a melting point of 960°C . Four old STO samples are glued around the substrate to ensure the homogeneity of the temperature. The substrate and side plates are pre-baked at 300°C in air to make the glue harder in order to sustain high temperatures. A heater cover with a hole of 1.5 cm is used to have only substrates and side plate face the plasma, which helps to avoid contamination of the whole heater. The system is pumped down

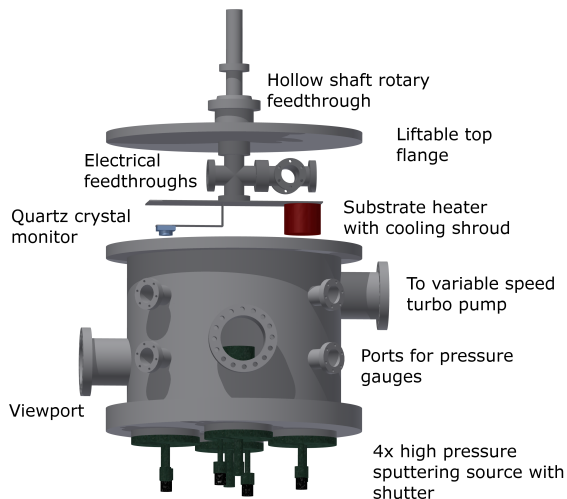


Figure 3.2: A 3d schematic view of the oxide sputtering system.

with a turbo pump for at least 8 hours which achieves a pressure of 1×10^{-6} mbar. Oxygen with purity of 99.999 % is entered into the system monitored by a flow meter. The pressure is regulated with the speed of the turbo pump, controlled by software. In DC sputtering, the targets are pre-sputtered at 1 mbar at a current of 100 mA and then deposition is done at a current of 350 mA at 3 mbar or 2.2 mbar. In RF sputtering, 20 W power is used for pre-sputtering and 30 W or higher power for deposition. The substrate holder which contains a heater is set to the optimized deposition temperature (which is 840°C for conducting films of LSMO and LCMO and 920°C for stoichiometric and non-stoichiometric LAO targets) and then the substrate holder is rotated on the top of plasma to deposit thin films of the required material. After deposition, the samples were cooled down in vacuum. Some samples of LaAlO_3 were cooled down in the growth pressure of oxygen but no significant changes were observed in properties of thin films.

3.2 Surface and structure characterization

Atomic force microscopy was used to view topography of all the LSMO, LCMO and LAO films. To investigate the quality of the films, we used x-rays diffraction.

3.2.1 Atomic Force Microscopy

All grown thin films are characterized by atomic force microscopy in tapping mode which provides better resolution of the images. AFM shows the quality of film surfaces in terms of flatness, roughness, and height profile. In tapping mode, the

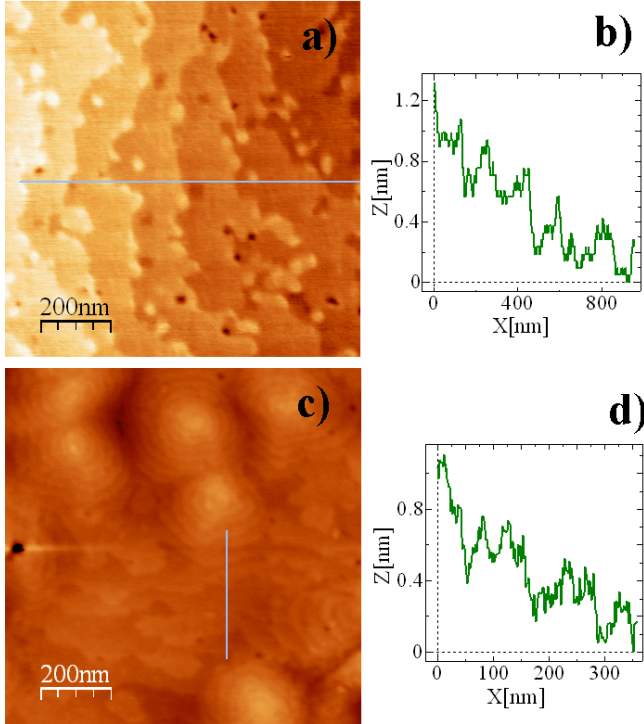


Figure 3.3: (a) Surface morphology of a 12 nm film of LSMO on STO, (b) the variation in height profile of (a) the step height is 0.4 nm. (c) A 35 nm film of LSMO on STO, shows spiral type morphology on some parts. The line profile (d) of the film is taken from the smoother part of the film. The overall roughness is 2 nm.

cantilever (driven by a piezoelectric actuator) vibrates at its resonance frequency. Upon approaching the sample, the tip briefly touches (taps) the surface at the bottom of each swing, resulting in a decrease in oscillation amplitude. The feedback loop keeps this decrease at a preset value and a topographic image of the sample surface can be obtained.

Figure 3.3 shows two films of LSMO on STO of thickness 12 nm and 35 nm. In Figure 3.3a, a very thin LSMO film shows the unit cell step height variation of the STO substrate. This indicates epitaxial match with the substrate. The thick film shown in Figure 3.3c shows spiral type morphology. At some portions, the steps can be seen. The roughness of 12 nm thick film is 0.4 nm while thick films are rougher because of more layers of material being deposited.

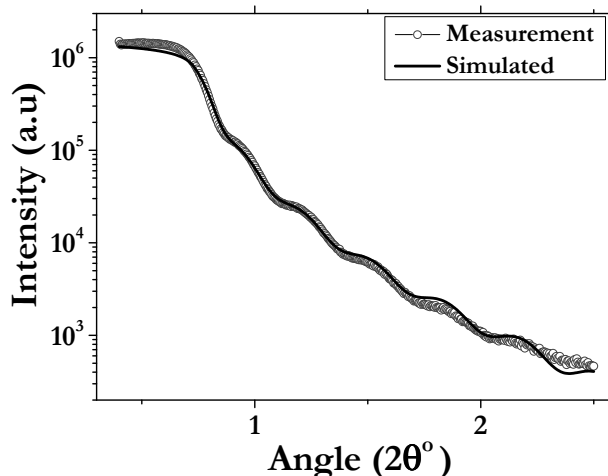


Figure 3.4: An X-ray reflectivity curve for a 24 nm thick film LCMO on STO (L598). The period of oscillation determines the thickness of film.

3.2.2 X-ray reflectometry (XRR)

X-ray reflectometry (XRR) is a non-contact, non-destructive analytical technique to determine thickness, density, and roughness of thin films. The basic idea behind the technique is to irradiate the sample with a beam of x-rays at very low angles. Increasing the angle of irradiation beyond a critical angle (depend on material), reflects the x-rays from interfaces and gives rise to interference fringes. The periodicity of the fringes is proportional to the thickness of the film. If the interface is not perfectly sharp and smooth then the reflected intensity will deviate from that predicted by the Fresnel law of reflectivity. This drop of intensity corresponds to the roughness of the films and the amplitude of the fringes is proportional to the density of the top and bottom layers. Figure 3.4 shows a film of 24 nm thick film of LCMO on STO. The number of fringes indicate the thickness and high intensity indicates the low interstitial roughness.

3.2.3 X-ray Diffraction (XRD)

X-ray diffraction is used to study the structure of thin films. We used a Siemens d500 diffractometer and a PAN analytical X-ray detector in Leiden to investigate the phase composition of thin films and the lattice constants. Figure 3.5 shows a typical way to measure lattice parameters. Taking STO as a reference, the lattice parameter of the film is calculated using Bragg's relation ($d \sin\theta = n \lambda$). Figure 3.5 shows a 20 nm thin film of LSMO on STO. The mismatch between film and substrate is about -1.4%.

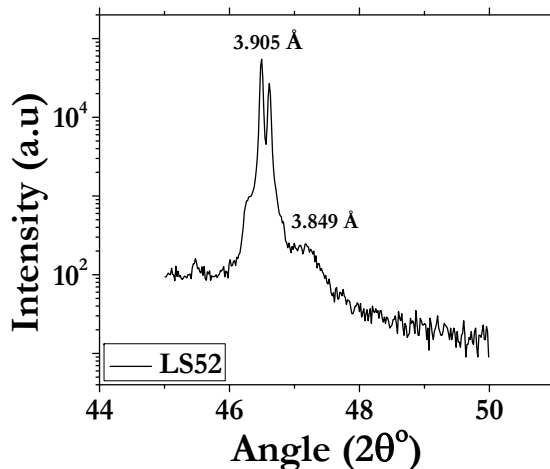


Figure 3.5: An XRD analysis of a 20 nm thin film of LSMO on STO.

3.2.4 Reciprocal Space Mapping (RSM)

High resolution XRD (RSM) measurements were performed with a Bruker D8 discoverer, equipped with a monochromator ($\lambda = 1.5406 \text{ \AA}$) and a Vantec-1 array detector in Twente University by Dr. S. Harkema. RSM measurements were performed on some films of LSMO, LCMO and LAO. The advantage of reciprocal space mapping is that the Bragg reflection under investigation is fully mapped in a confined area in Q-space. This means that the reflection is not only monitored by rocking curve crossing it but all directions are included in the measurement. This gives extra advantage to the non-symmetry of the crystals and to the epitaxy of the thin films. RSM maps for LCMO thin films are shown in section 3.5.

3.3 Lithographical techniques for patterning

We have used both optical and electron beam lithographic techniques to pattern LSMO and LCMO thin films to measure transport properties of these thin films. Figure 3.6 shows the basic process for optical and electron beam lithographic techniques. For positive resists, the resist is exposed with UV light or electron beam to remove the underlying material. The chemical structure of the resist becomes more soluble in the developer after exposure. The developer solution is washed away the exposed resist. Negative resists behave in just the opposite manner. Exposure to the UV light or electron beam causes the negative resist to become polymerized, and more difficult to dissolve. Therefore, the negative resist remains on the surface wherever it is exposed. The developer solution removes only the unexposed portions.

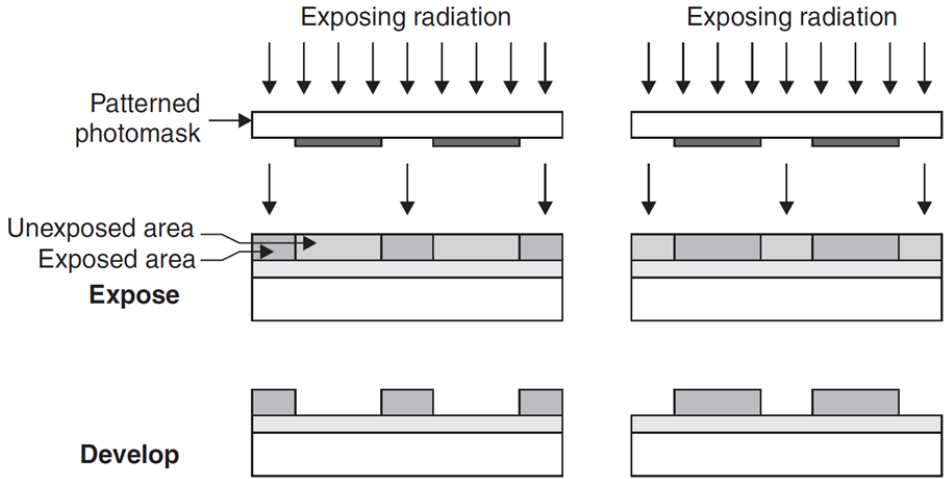


Figure 3.6: Lithographic operation with positive and negative resist (a) positive resist removes the exposed area and (b) negative resist leaves on the expose area after exposure and developing

3.3.1 Optical lithography

The LCMO and LSMO thin films were structured optically in a Hall bar geometry to investigate the effect of strain on carrier density. The structure is about $200\ \mu\text{m}$ wide and the distance between the voltage contacts was $1.2\ \text{mm}$. A positive resist MaP1205 was spun on to the sample with 6000 revolution per minute (rpm). The sample was baked at 120°C for 120 seconds. After that sample was exposed to UV light for 15 sec. Then it was developed in MaD532 for 15 seconds. LSMO films were structured using wet etching (H_2O : 49% HF: HCl: $\text{HNO}_3 = 25: 1: 1: 1$) with an etch rate of 2 nm per minute for LSMO films. LCMO thin films were etched using argon ion etching with an etch rate of 0.3 nm/sec. After Ar-etching, the LCMO films were treated with an oxygen plasma in order to restore the insulating properties of the STO substrate [8].

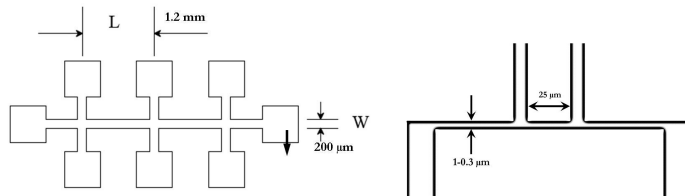


Figure 3.7: (Left) A standard Hall bar, (right) a structured patterned written with e-beam for small bridges, not to scale.

3.3.2 Electron beam lithography

We have used electron beam lithography to pattern small bridges for measuring the Hall effect and current-voltage characteristics. For this a Raith e-line machine was available which is a high resolution electron beam lithography system.

A Hall bar of width $50\ \mu\text{m}$ (the distance between voltage contacts = $94\ \mu\text{m}$) was patterned on a few LCMO films. We also patterned thin films of LSMO and LCMO in small bridges of width from $1\ \mu\text{m}$ down to $300\ \text{nm}$ to measure current voltage characteristics, with a distance of $25\ \mu\text{m}$ between voltage contacts.

A three step process was used to pattern Hall bar and small bridges. The typical structured patterns are shown in Figure 3.7. In the first step, Au markers were written because the contrast of LSMO or LCMO on STO is very poor. A lift-off process was used for this purpose: a bilayer of PMMA/MMA was spun on top of samples. The sample was baked at $180^\circ\text{C}/120^\circ\text{C}$ for 90/90 seconds and then only markers were written with e-beam. After developing, the sample was sputtered with gold in a Z400 sputtering system and then the lift off process is accomplished. In the second step, negative resist MaN2405 was spun onto the sample, and baked at $90^\circ\ \text{C}$ for 10 minutes. Then the structure of LSMO or LCMO was written. After developing, the sample was etched either wet or by argon ion etching. In the third step, the first step was repeated but now for making Au contacts using the Au markers as reference.

3.4 Measuring properties of thin films

The transport properties of unstructured and structured thin films of LSMO and LCMO were measured using a physical properties measuring system (PPMS) from Quantum Design. The temperature range for the system is from 2 K to 400 K and magnetic field can be set up to 9 T. The temperature stabilization is better than 200 mK. External voltage and sources are used to measure structured and unstructured thin films, current-voltage behavior and Hall voltage. Different LabVIEW programs were designed to accomplish this task.

The magnetic properties of thin films were measured using a SQUID-based magnetic properties measuring (MPMS) from Quantum Design. The system can vary temperature between 2 K to 400 K and a magnetic field can be applied in transverse and longitudinal direction upto 7 T. We have measured Curie temperature T_c and the saturation magnetization to find out anomalous behavior in thin films of LSMO and LCMO.

3.5 Avoiding target degradation in sputtering manganese thin films

In this section, we address the issue of aging of the sputtering targets. After prolonged use (typically a few years), we find that the morphology of the films becomes poor: hole appear, step size become larger, and the roughness increases.

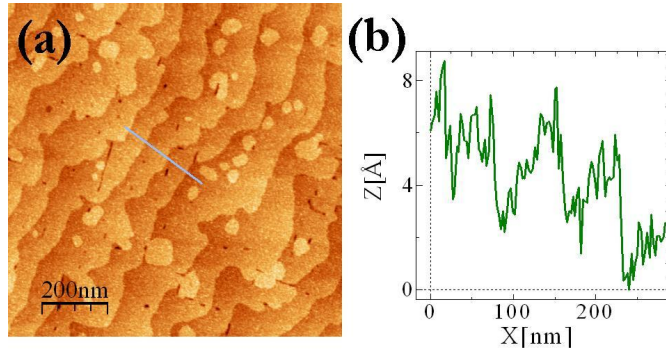


Figure 3.8: (a) Surface morphology of a 15 nm thin film of LCMO (L561) shows flat terraces. (b) The height profile gives step height of unit cell of 0.4 nm and the average roughness of the film is 0.2 nm.

We have performed experiments on the treatment of targets with water vapor in order to reverse their degradation. Below, we discuss the growth of films of LCMO on flat STO substrate before and after the target treatment.

3.5.1 Characteristic features of thin films of LCMO

Thin films of $\text{La}_{0.7}\text{Ca}_{0.3}\text{MnO}_3$ grown on SrTiO_3 substrate have characteristic features which can be distinguished by atomic force microscopy and transport properties. It is known that thin films of LCMO can be epitaxially grown on STO substrate, even though the mismatch ($a_{\text{LCMO}} = 3.783 \text{ \AA}$, $a_{\text{STO}} = 3.905 \text{ \AA}$, mismatch is -1%) leads to strained films. Still, they can be flat, with unit cell steps, which reflects the underlying substrate. In thick films, structural defects appear, the roughness also increases and steps are not visible anymore.

Figure 3.8a shows the topography of a 15 nm thin film of LCMO on STO grown with a new LCMO target. The film shows unit cell step height (Figure 3.8b). A detailed structural and interface analysis by HRTEM and EELS of these films is given elsewhere [9, 10].

Another distinguishing feature of LCMO thin films comes from the transport properties. Single crystal and very thick films of LCMO grown on any substrate show a T_{MI} of 270 K as shown in Figure 3.9 for a 75 nm film. In very thin films T_{MI} depends on lattice mismatch between substrate and film. STO produces tensile strain on LCMO whose in-plane lattice constant elongates Mn-O-Mn bond length and decreases Mn-O bond angle which suppresses the ferromagnetic state of LCMO, and reduces the transition temperature. It can be seen in Figure 3.9 that for a 11 nm film, T_{MI} is 130 K, 150 K less than the thicker one. A large reduction in resistance in LCMO films gives a large CMR effect [11] which is another characteristic feature of these films.

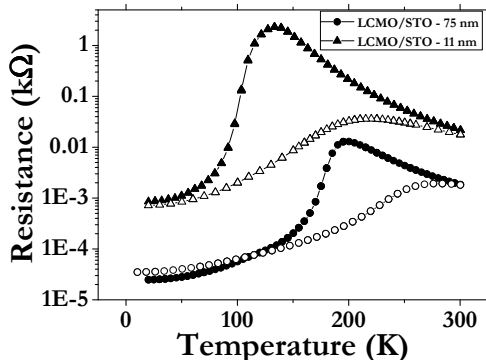


Figure 3.9: Temperature dependence of resistance for two films of LCMO on STO, a 75 nm film (shown in square symbols) and a 11 nm thin film (shown in triangles). Filled symbols represent the temperature versus resistance behavior at 0 T and open symbols at 9 T.

3.5.2 Observations-possible causes of rough films

We observed that thin films started to deteriorate with the passage of time without changing any growth parameters e.g., growth pressure, growth temperature, target to substrate distance, flow of oxygen. One of the films in this series of rough films is shown in Figure 3.10a. The growth time for this films is the same as shown in Figure 3.8a. It shows a structure of not well connected grains and holes as dark spots. The profile shows a non-homogeneous film which has a grain size of a 20 nm (Figure 3.10b). The rms surface roughness of this film is 5 nm.

The transport properties of such a film may show T_{MI} but also insulating behavior at low temperature as shown in Figure 3.11. Two thin films of 13 nm and 11 nm shown in Figure 3.11 and in Figure 3.9 respectively have approximately the same thickness but an insulating state shows up at low temperature for a film grown with an old target (L579). Some films grown with the old target show two or three resistance peaks (not shown here) which is improbable and indicates that films do not have the properties of LCMO films.

3.5.3 Hypothesis - role of Oxygen in LCMO

We see in the last two figures that thin films of LCMO are not good. They show large grains, are very rough and insulating. Without changing any growth parameters, the target was working for a long time to grow epitaxial LCMO films. We also observed a seasonal change in morphology which might be due to the humidity level which can effect the oxygen content in the growing films. We also know that the correct oxygen content is an important ingredient for high quality thin films of manganites. The role of oxygen stoichiometry is extensively studied for the colos-

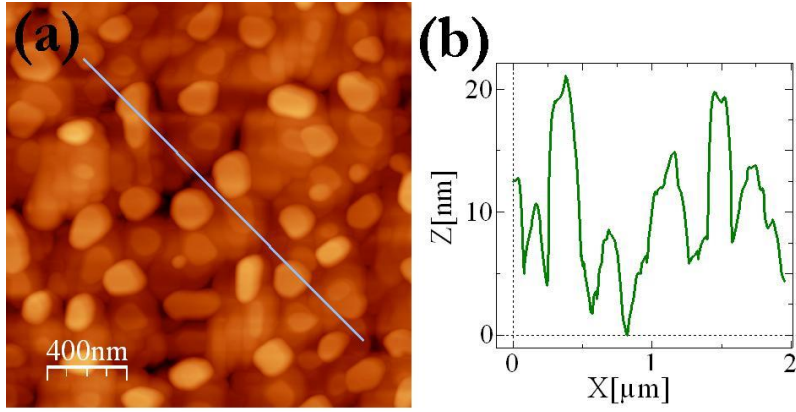


Figure 3.10: (a) Surface morphology of a 13 nm thin film of LCMO (L579) with a relatively old target (b) The height variation is 20 nm and rms roughness is 5 nm.

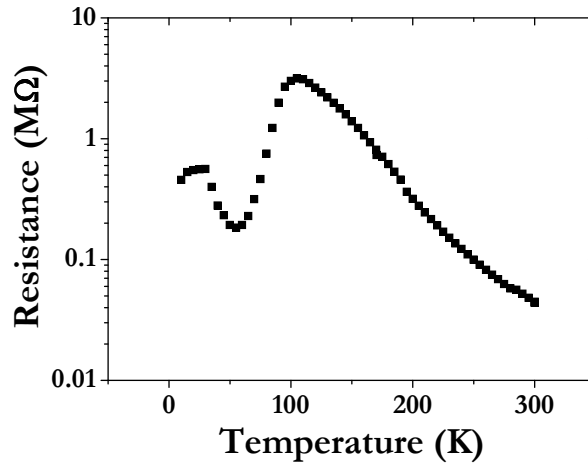


Figure 3.11: Temperature dependence of resistance of a 13 nm film of LCMO on STO (L579), the morphology of same films is shown in Figure 3.10.

sal magnetoresistive manganites [12–17]. The deficiency of oxygen can influence the crystalline structure, transport and magnetic properties of thin films [18, 19]. The preparation conditions are important for the growth of thin films and the oxygen content can be varied by changing the pressure of ambient gas or by post annealing [20]. The oxygen deficient films can be very rough and highly resistive.

Like manganites, high T_c superconductor YBCO has also been studied for the sensitivity of different growth parameters [21]. These critical growth parameters give a narrow window for epitaxial growth of thin films. Krupke *et al.* explained it as possible change in thin films of YBCO for a prolonged used target [22] and suggested treatment with water vapors [23]. Addition of water vapors produces atomic oxygen which triggers the film composition by increasing the atomic oxygen pressure since the dissociation of O_2 in a microwave discharge is almost entirely due to nitrogenous and hydrogenous impurities, as proved by Kaufmann and Kelso [24]. Costa *et al.* [25] and Brown *et al.* [26] showed that enhanced atomic oxygen content in the plasma was caused by a reduced combination rate of atomic oxygen at the chamber walls. In any case, each hydrogen atom introduced produces about 300 extra oxygen atoms which can be used to condition the old LCMO target. The poor morphology which shows holes in LCMO thin films may be caused by the LCMO target itself. The target might have exceeded its life time which results in reduced oxygen stoichiometry in the growing films.

3.5.4 Results-Reutilizing the LCMO target

Assuming the possible loss of oxygen in LCMO target, we treated the target with external oxygen in form of water vapors. A small reservoir of water was connected to the vacuum chamber which can be controlled by a power supply. The water pressure was optimized with respect to the base pressure of the system and few μ bar of water vapors were introduced in the system. The base pressure of our system is 1×10^{-6} mbar. The added water vapor is the water pressure at which thin films have been grown. The system was stabilized at water pressure for about one hour and then a specific process of pre-sputtering, sputtering and deposition was started. As this process relates to the dissociation of oxygen atoms, we name it pressure controlled oxygen dissociation (PCOD). The optimized water pressure in which high quality thin films are grown was 5×10^{-5} mbar. Below this pressure, films have holes and above this pressure, strange features in morphology were observed.

We have grown thin films at three different water pressures. Three pressures which show significant variation in morphology and structure are given in Table 3.2. We use three representative films to explain the growth of LCMO films at these water pressures.

Figure 3.12 shows three films grown at the water pressures given in Table 3.2. Film at pressure P1 is smooth but it shows some decorated outgrowth, following the steps of the substrate (Figure 3.12a). The step size is also higher than 2 nm. The film grown at P2, shown in Figure 3.12c, is very rough. The grainy structure is clearly seen. We have grown another film at a pressure in between these two

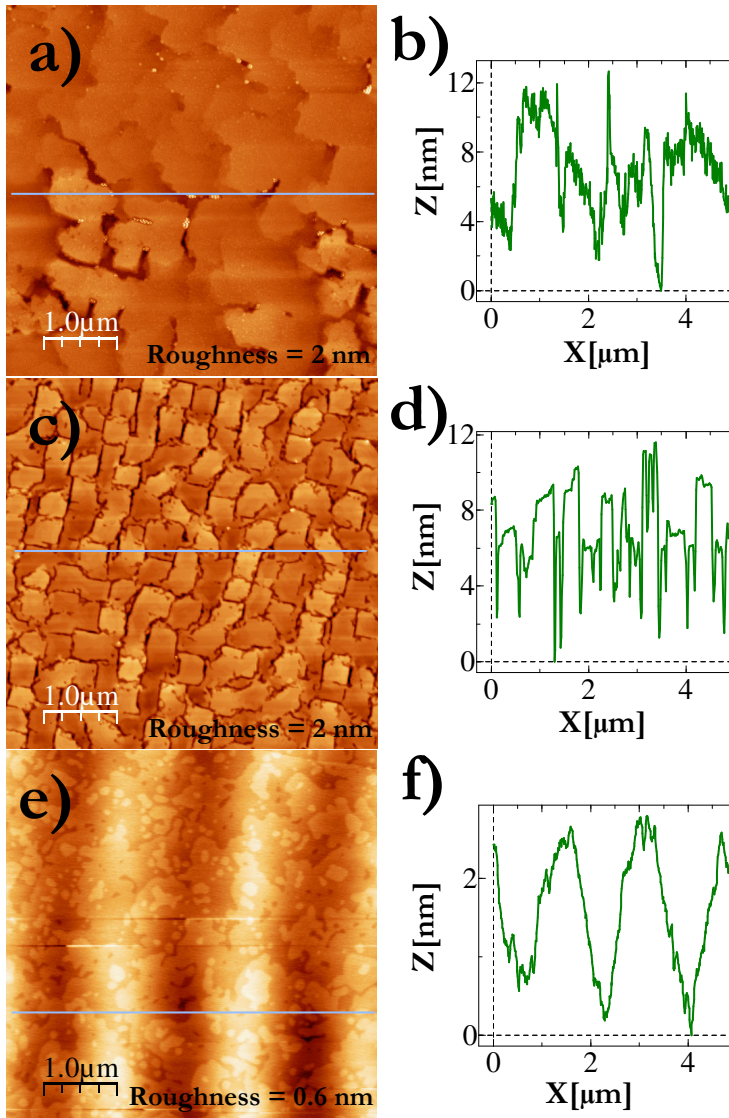


Figure 3.12: Effect of external oxygen on the morphology of thin films of LCMO. According to table 3.2 at pressure P1(L581) (a,b) at pressure P2 (L582)(c,d) at pressure P3 (L589) (e,f).

P_{water} (mbar)	Process ID	Roughness (nm)	d_{LCMO} (nm)	Sample ID
1×10^{-4} mbar	P1	2	x	L580
1×10^{-5} mbar	P2	2	10	L581
5×10^{-5} mbar	P3	0.6	24	L589

Table 3.2: Treatment of oxidized LCMO target at different water pressures to optimize the growth of thin films of LCMO. Given are the pressures used to optimize water content represented by P_{water} mbar, the process ID related to water-pressure, the roughness in nm, thickness of film d_{LCMO} (nm), and the relative sample identity ID.

pressures, P3. In Figure 3.12e, the film shows flat terraces with roughness of 0.2 nm.

The thickness of the films was measured by XRR. It is important to note that for film P1, fringes could not be found. We used XRD for structural analysis of the films. The diffraction plane (002) can only be found for the films grown by P3 while for the other films, no film peak can be seen.

LCMO thin films were analyzed by reciprocal space maps (RSM) which gave a good analysis of the epitaxy of the films. Figure 3.13 shows a reciprocal space map of the 10 nm film of LCMO on STO (L589) grown by P3 around the reflection (123). The peak of the film can be seen above the substrate peak (a very bright spot at the center). The out-of-plane lattice constant determined with this reflection is 0.382 nm. The in-plane peak values for film and substrate is the same, which shows that the film is epitaxial. The corresponding values of the in-plane lattice constant for film and substrate is 0.39 nm.

Figure 3.14 shows the resistance versus temperature behavior and it is clear that film grown at P3 has a transition temperature of 160 K as expected for this thickness (10 nm), while other three films do not have any transition which means that they do not have the properties correct LCMO. So, the optimized growth water pressure is P3, 5×10^{-5} mbar. At this pressure, we can grow high quality epitaxial manganite thin films of LCMO.

3.5.5 Pre-conditioning only

The purpose of water vapor addition to the sputter gas was to condition the target. We also tested film growth where we pre-sputter the target with water but closed its supply while depositing. The films grown in this way showed good morphology, crystallinity, phase and correct transition temperature corresponding to thickness of film. The only difference observed was that films which were grown with water have lower growth rate than done only by conditioning (pre-sputtering in water). This shows that the right tuning of water can compensate the deficiency of oxygen in old LCMO target.

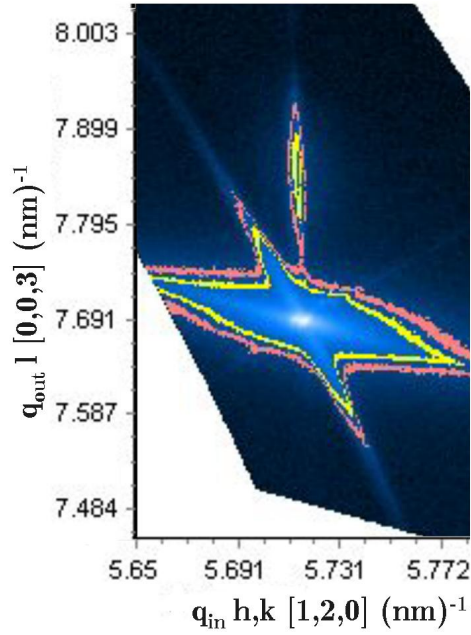


Figure 3.13: A reciprocal space map of 10 nm thick LCMO film on STO (L588) around the [123] reflection grown by P3. The film peak can be seen at 7.85 nm^{-1} .

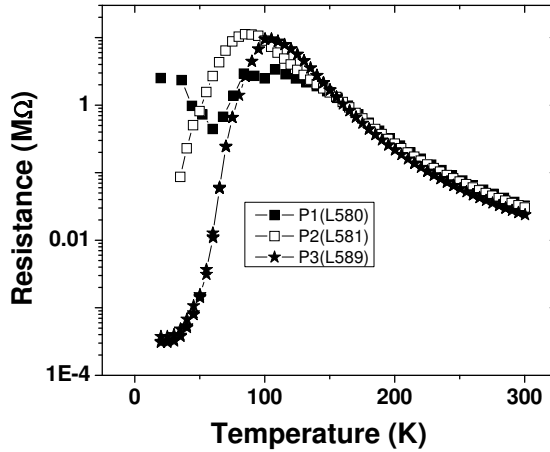


Figure 3.14: Transport properties of thin films of LCMO on STO (001) after treatment of target under different water pressures (see Table 3.2).

3.5.6 Role of substrate orientation

We described the effects of additional oxygen on thin films of LCMO on STO (001) substrates. This conditioning/treatment works also well for flat substrates of LSGO (001) and on NGO (001). The process does not work for substrates which have higher miscut angles or different orientation of planes, e.g., STO (110) and 1° stepped STO (001). The different orientation of planes in these substrates may require different water pressure to be optimized or a different growth temperature.

3.5.7 Conclusion

Thin films of LCMO were treated by water on flat STO (001) substrate using the PCOD process. Highly epitaxial thin films with the correct transition temperature depending on thickness on strained STO can be obtained in this process. The process also worked by only conditioning the target and stopping the water supply during growth, which increased the growth rate of thin films of LCMO. The optimized water pressure only worked for flat substrates with (100) orientation while stepped STO (001) and STO (110) may need to re-calibrate at a different water pressure.

Bibliography

- [1] D.A. Glocker, S.I. Shah, Hand book of thin films process technology, Vol. **1**, IOP publishing Ltd, 2002.
- [2] M. Kawasaki, K. Takahashi, T. Maeda, R. Tsuchiya , M. Shinohara, O. Ishiyama, T. Yonezawa, M. Yoshimoto and H. Koinuma, Science **266**, 1540 (1994)
- [3] G. Koster, B.L. Kropman, G.J.H.M. Rijnders, D.H.A. Blank and H. Rogalla, Appl. Phys. Lett. **73**, 2920 (1998).
- [4] S. Migita, Y. Kasai, S. Sakai, J. Low Temp. Phys. **105** , 1337 (1996).
- [5] R. Takahashi, Y. Matsumoto, T. Ohsawa, M. Lippmaa, M. Kawasaki, and H. Koinuma, J. Cryst. Growth **234**, 505 (2002).
- [6] S. Geller, Acta Cryst. **10**, 243 (1957).
- [7] S. Freisem, PhD thesis, University Leiden, the Netherlands (1999).
- [8] C. Beekman, I. Komissarov, M. Hesselberth and J. Aarts, Appl. Phys. Lett. **91**, 062101 (2007).
- [9] J. Aarts, S. Freisem, R. Hendrix, H.W. Zandbergen, Appl. Phys. Lett. **72**, 2975 (1998).
- [10] Z.Q. Yang, R. Hendrix, J. Aarts, Y.L. Qin, H.W. Zandbergen, Phys. Rev. B **70**, 174111 (2004).
- [11] S. Jin, T.H. Thiel, M. McCormack, R.A. Fastnacht, R. Ramesh, and L.H. Chen, Science **264**, 413 (1994).

- [12] C. Ritter, M.R. Ibarra, J.M.D. Teresa, P.A. Algarabel, C. Marquina, J. Blasco, J. Garcia, S. Oseroff, and S.-W. Cheong, *Phys. Rev. B* **56**, 8902 (1997).
- [13] Z.L. Wang, J.S. Yin, Y.D. Jiang, and J. Zhang, *Appl. Phys. Lett.* **70**, 3362 (1997).
- [14] J. Li, C.K. Ong, J.-M. Liu, Q. Huang, and S.J. Wang, *Appl. Phys. Lett.* **76**, 1051 (2000).
- [15] R. Cauro, A. Gilabert, J.P. Contour, R. Lyonnet, M.-G. Medici, J.-C. Grenet, C. Leighton, and I.K. Schuller, *Phys. Rev. B* **63**, 174423 (2001).
- [16] X.F. Song, G.J. Lian, and G.C. Xiong, *Phys. Rev. B* **71**, 214427 (2005).
- [17] N. Malde, P.S.I.P.N. de Silva, A.K.M.A. Hossian, L.F. Cohen, K.A. Thomas, J.L. MacManus-Driscoll, N.D. Mathur, and M.G. Blamire, *Solid State Commun.* **105**, 643 (1998).
- [18] S.J. Liu, J.Y. Juang, J.-Y. Lin, K.H. Wu, T.M. Uen, *J. Appl. Phys.* **103**, 023917 (2008).
- [19] M. Rajeswari, R. Shreekala, A. Goyal, S.E. Lofland, S.M. Bhagat, *Appl. Phys. Lett.* **73**, 2672 (1998).
- [20] A. Goyal, M. Rajeswari, R. Shreekala, S.E. Lofland, S.M. Bhagat, T. Boettcher, C. Kwon, R. Ramesh, and T. Venkatesan, *Appl. Phys. Lett.* **71**, 2535 (1997).
- [21] J.R. Gavaler, J. Talvacchio, T.T. Braggins, M.G. Forrester, and J. Gregg, *J. Appl. Phys.* **70**, 4383 (1999).
- [22] R. Krupke, Z. Barkay, G. Deutscher, *Physica C* **289**, 146 (1997).
- [23] R. Krupke, Z. Barkay, G. Deutscher, *Physica C* **315**, 99 (1999).
- [24] F. Kaufman, J.R. Kelso, *J. Chem. Phys.* **32**, 301 (1960).
- [25] M.D. Costa, P.A. Zuliani, and J.M. Deckers, *Can. J. Chem.* **57**, 568 (1979).
- [26] R.L. Brown, *J. Chem. Phys.* **71**, 2492 (1967).

Carrier density in thin films of doped manganites

In chapter 2 we discussed the physics of La doped manganites in detail. The double exchange mechanism explains the interplay of metallicity and ferromagnetism at low temperatures. At high temperatures, the trapping of electrons occur due to the distortion of oxygen octahedra under the Jahn-Teller effect. The physical properties of these materials largely depend on doping level. The doping of divalent Ca or Sr in the range between 0.2 and 0.5 gives a ferromagnetic metal regime. A ferromagnetic to paramagnetic transition takes place at Curie temperature T_c accompanied by a metal-to-insulator transition at the transition temperature T_p which has practically the same value as T_c . A doping of 0.3 for Ca or Sr gives the highest T_c and T_p . In thin films under strain, T_c and T_p go down, sometimes considerably. In this chapter, we investigate whether the carrier density is affected in very thin films, or when the films are under strain. For this we study the Hall effect.

In this chapter, we study the Hall effect in thin films of $\text{La}_{0.7}\text{Ca}_{0.3}\text{MnO}_3$ and $\text{La}_{0.7}\text{Sr}_{0.3}\text{MnO}_3$ deposited on SrTiO_3 (STO), NdGaO_3 (NGO) and LaSrGaO_3 (LSGO) substrates in a temperature range from below (10 K) to above (400 K) the metal-insulator transition, in magnetic fields up to 9 T, and for thicknesses between 7 nm and 75 nm. The charge carrier density as calculated from the Hall voltage in a single band picture shows bulk-like values for the thick films, but a significant decrease in thin films (below 20 nm), both for strained thin films (on STO) and unstrained thin films on NGO, although less in the case of unstrained films on LSGO. It is well known however that a single band model is not appropriate for the manganites, in which both electron and hole surfaces occur simultaneously. We therefore analyzed the data in a two-band scenario. We still come to the conclusion that the *average* carrier density in the thin films, both strained and unstrained, is lower than in the thicker bulk-like films. We discuss this in terms of charge discontinuities and a possible dead layer at the various interfaces, which appear to play a significant role. We also found conductance anisotropy in transverse direction as a good tool to characterize the homogeneity of thin films of $\text{La}_{0.7}\text{Ca}_{0.3}\text{MnO}_3$ and $\text{La}_{0.7}\text{Sr}_{0.3}\text{MnO}_3$.

4.1 Introduction

Doped manganese perovskite oxides have generated much interest in the last decade, because of the rich physics resulting from the interplay between the electron, lattice, and spin degrees of freedom, and leading to phenomena such as Colossal Magnetoresistance, phase separation, and full spin polarization [1–3]. Considering the La-based 1-1-3 family of manganites, the parent compound LaMnO_3 has a structure consisting of 6 corner-sharing MnO_6 octahedra on a simple cubic lattice, encaging the La-ion. It is an antiferromagnetic Mott insulator which can be driven to a metal by partial substitution of divalent Sr^{2+} or Ca^{2+} ions on the La^{3+} sites. The substitution creates holes as charge carriers and above a critical composition of $x_c = 0.17$, a ferromagnetic metallic state forms below the Curie temperature T_c . At a doping level of $x = 0.3$, T_c is around 250 K for $\text{La}_{0.7}\text{Ca}_{0.3}\text{MnO}_3$ (LCMO hereafter) and 370 K for $\text{La}_{0.7}\text{Sr}_{0.3}\text{MnO}_3$ (LSMO). Above T_c the material is a polaronic insulator, and the transition at T_c is therefore both metal-to-insulator (MI) and ferromagnetic-to-paramagnetic. The transition is mainly determined by the competition between the trapping of electrons in Jahn-Teller distortions [4] and the itinerancy of charge carriers through the double exchange mechanism [5, 6]. The sensitivity of the properties of the manganites to lattice distortions is seen in the effects of hydrostatic pressure, which can significantly enhance T_c through rotations of the MnO_6 octahedra [7].

The same sensitivity to lattice distortions makes it possible to apply strain engineering in thin films, by varying the (mis)match between the lattice parameters of film and substrate, as was for instance demonstrated in Refs. [8, 9]. For LCMO in particular, the effects of tensile strain are well documented. Growing LCMO with a pseudocubic lattice parameter of $a_c = 0.387$ nm on SrTiO_3 (STO) with $a_c = 0.391$ nm can lead to a lowering of T_c of more than 150 K for the thinnest films which still show an MI-transition [10–12]. This is generally attributed to the effect of the decrease of the bandwidth of the itinerant d -electrons, due to the change in Mn-O-Mn bond angles and the accompanying decrease of the electron hopping parameter, while also the biaxial nature of the strain plays a role [13]. Such a discussion in terms of the bandwidth of a simple one-band model is not fully correct. Hall-effect measurements on single crystals and thick films consistently show, when analyzed in a one-band model, a higher carrier concentration than the chemical doping indicates (0.3 holes per unit cell for a 2+ doping of 30%). For instance, Asamitsu and Tokura reported a value of 1 hole/Mn site in single crystals of LSMO (30% Sr) [14]; Jacob *et al.* found 0.7 hole/Mn-site in thick films of LCMO (33% Ca) [15]; and Chun *et al.* found values up to 2.4 holes per unit cell in single crystals of $\text{La}_{2/3}(\text{Ca,Pb})_{1/3}\text{MnO}_3$ [16]. Other reports find similar numbers [17–19]. More than one band is therefore involved in the transport, and this is also indicated by band structure calculations, which find Fermi surfaces with both electron and hole character [20]. Any analysis of Hall data has then to be performed in a scenario of at least two bands, which is not always fully appreciated.

What has not yet been investigated is changes in Hall effect and possibly the carrier density when LSMO or LCMO films become thin and/or strained. This

is relevant, for instance, since microscopic mechanisms advocated to explain the decrease of T_c in strained thin films do not take a possible change of carrier density into account. Also the possibility of valence variations at the interface would make it possible that the carrier density changes when the films become very thin. Here we present results on the ordinary Hall coefficient measured in high magnetic fields, obtained on such films grown strained on SrTiO₃ (STO) and unstrained on NdGaO₃ (NGO) and LaSrGaO₃ (LSGO). We find that, at low temperatures, the one-band hole density $n_{h,1}$ for thick films is found close to 1.5 holes per unit cell, similar to the bulk value and demonstrating again that the Hall coefficient is not a measure for the carrier density when analyzed in a one-band scenario. Below a thickness of typically 20 nm the value of $n_{h,1}$ becomes smaller, and for strained films even goes down to 0.5. In the one-band model this would mean a decrease of the carrier density, but we show that also in terms of a two-band model (in which the mobilities of the various carriers are separate parameters) the conclusion must be that the thin films have a lower carrier density than thick films or bulk material. We argue that this is in line with observations of dead layers and valence variations at the interface.

4.2 Experimental

Epitaxial thin films of LCMO ($a_c = 0.3863$ nm) and LSMO ($a_c = 0.3873$ nm) were deposited on substrates of STO(100) ($a_c = 0.3905$ nm), NGO(100) ($a_c = 0.3851$ nm; note : this is NGO(110) in orthorhombic notation) and LSGO(100) ($a_c = 0.3843$ nm) using dc sputtering in pure oxygen at a pressure of 3 mbar. The experimental procedure has been described before [12, 21, 22] and also in chapter 3. The films ranged in thickness from 7 nm to 75 nm and were characterized by Atomic Force Microscopy (AFM) in tapping mode. A Physical Properties Measurement System (PPMS, Quantum design) was used for the temperature and field control. External current sources and voltmeters were used for the transport measurements of unstructured and structured thin films. The samples were patterned photolithographically into Hall structures. The bridges were 200 μm in width and 3.6 mm in length while the distance between two voltage contacts was 1.2 mm. Argon Ion Beam Etching (etch rate 0.3 nm/sec) was used for structuring the LCMO films, and wet etching ($\text{H}_2\text{O} : \text{HF} : \text{HCl} : \text{HNO}_3 = 25 : 1 : 1 : 1$) with an etch rate of 2 nm per second for the LSMO thin films. After Ar-Etching, the LCMO samples were treated with oxygen plasma in order to restore the insulating properties of the STO substrate [22]. For the measurements of the Hall coefficient, the temperature was stabilized to better than 20 mK. The data were taken at constant temperature, with a current between 1 mA and 100 μA . A full current-voltage measurement was made regularly to check linearity and the absence of an offset. The magnetic field (oriented perpendicular to the sample plane) was scanned from -9 T to +9 T, which takes about 3 hours.

4.3 Results

In this section, we present the morphology of the films, XRD and RSM maps, and resistivity measurements. High resolution XRD measurements were performed in Twente University in collaboration with Dr. S. Harkema.

4.3.1 Characterization by AFM

Figure 4.1a,b shows morphology and height variation of a 16 nm thick film of LCMO on STO called L583. The film is flat, and shows step-height variations of the order of a unit cell (0.4 nm), together with the beginning of spiral growth. Figure 4.1c,d shows the surface morphology and the height variation along a cross-section of a 25 nm thick film of LSMO on STO, called LS8. Again, height variations are not more than 0.4 nm.

4.3.2 Characterization by RSM

The film thickness was measured by x-ray reflectivity, using Cu-K α radiation, where the thickness of the film is defined by the period of oscillation. Films grown on STO are strained (mismatch: -1.07% in case of LCMO and -0.82% in case of LSMO), although the strain gradually relaxes with increasing thickness [21].

Figure 4.2 shows a reciprocal space map for the 25 nm thick film LS8 of LSMO on STO around the [123] reflection. The film is strained and epitaxial. Along the out-of-plane direction a clear film peak is visible separate from the substrate peak, while the in-plane direction shows the same peak values for substrate and film peak. The out-of-plane lattice parameter was determined with this reflection as well as the [002] and [003] reflections, and found to be 0.386 nm, well below the bulk value of 0.389 nm. Films of LCMO with a thickness below 20 nm, grown around the same time as the samples reported on here, showed an out-of-plane lattice parameter around 0.381 nm, much reduced from the pseudocubic bulk value, and confirming that such films are fully strained. Films on NGO (mismatch: less than 0.3% in case of LCMO and LSMO) are slightly tensile strained and on LSGO (mismatch: 0.52% in case of LCMO and 0.78% in case of LSMO) are slightly compressive.

4.3.3 Resistivity measurement

Figure 4.3a shows the temperature dependence of the longitudinal resistance $R(T)$ of structured films of LCMO for different thicknesses on different substrates (9 nm, 16 nm, 75 nm on STO, 16 nm on LSGO). Data are given both for zero field, and in a field of 9 T. The behavior is as reported before: the thinnest film on STO shows a peak temperature of the resistance T_p around 130 K, which then increases to 200 K for the 75 nm film. The films on better matching substrates show higher value of T_p , even though they are very thin. Figure 4.3b shows similar data for LSMO (LS15 with thickness 7 nm, LS8 with thickness 25 nm, a film of 75 nm) on STO. The effects of strain on LSMO are less strong, as can be seen from the fact

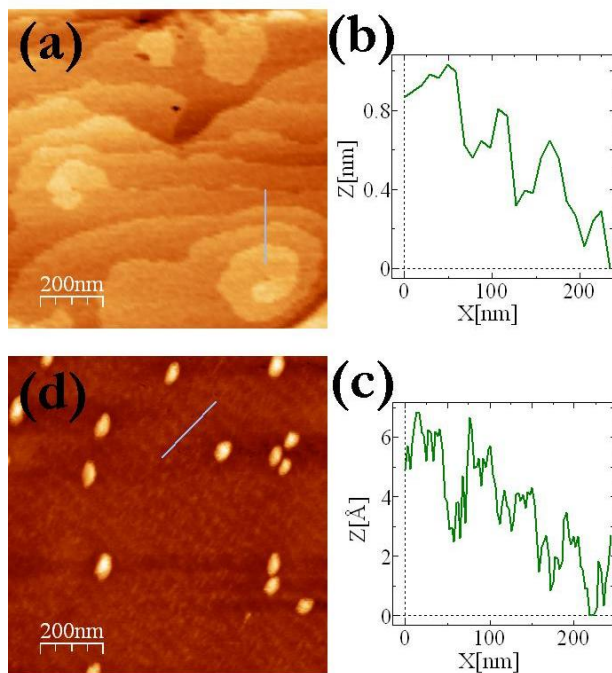


Figure 4.1: Surface morphology of (a) a 16 nm thick film of LCMO on STO (called L583); (c) a 25 nm thick film of LSMO on STO (called LS8). The panels (b) and (d) show the height variation along the lines given in (a) and (c), respectively.

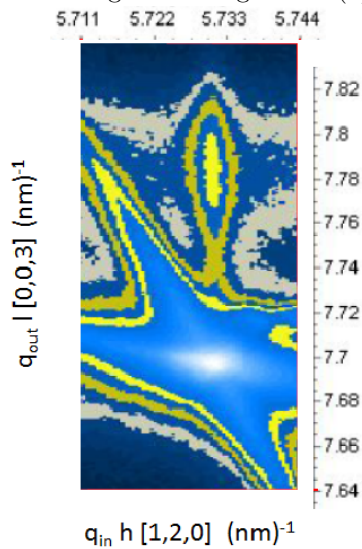


Figure 4.2: Reciprocal space map of a 25 nm thick film of LSMO on STO (called LS8), taken around the $[123]$ reflection. The film peak can be seen at $q_{out} \approx 7.78 \text{ nm}^{-1}$.

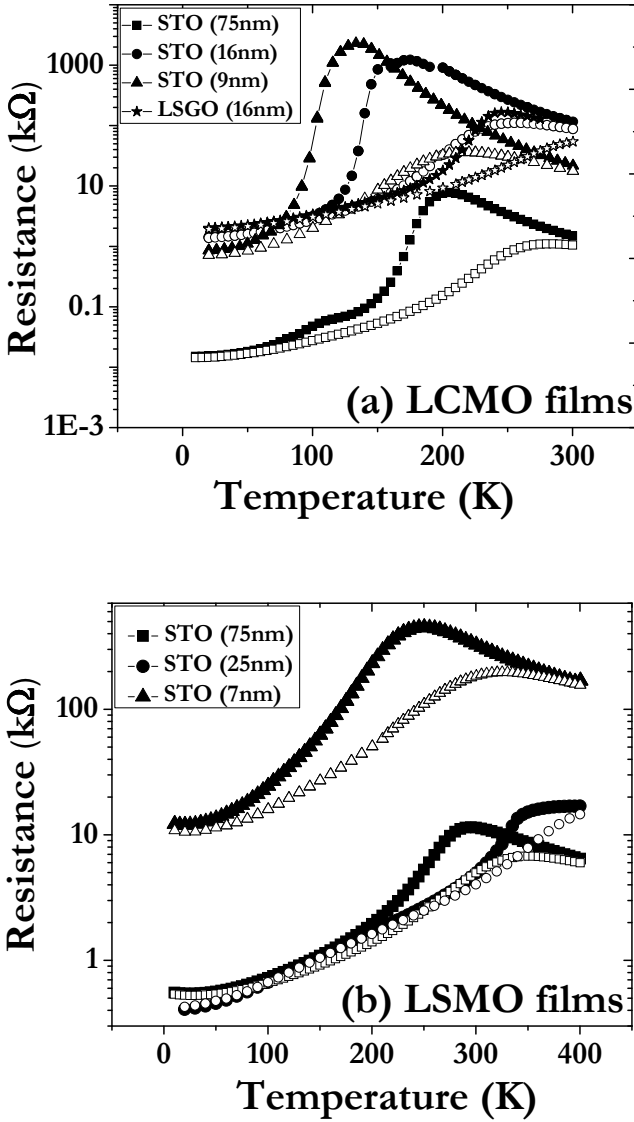


Figure 4.3: Resistance R versus temperature T in zero field and in a 9 T field of structured films of $\text{La}_{0.7}\text{Ca}_{0.3}\text{MnO}_3$ (LCMO) and $\text{La}_{0.7}\text{Sr}_{0.3}\text{MnO}_3$ (LSMO) of different thickness on different substrates. (a) LCMO: 9 nm, 16 nm, 75 nm on STO, 16 nm on LSGO. (b) LSMO: 7 nm (LS15), 25 nm (LS8), 75 nm on STO. The filled symbols show 0-field data, the open symbols show data taken in 9 T.

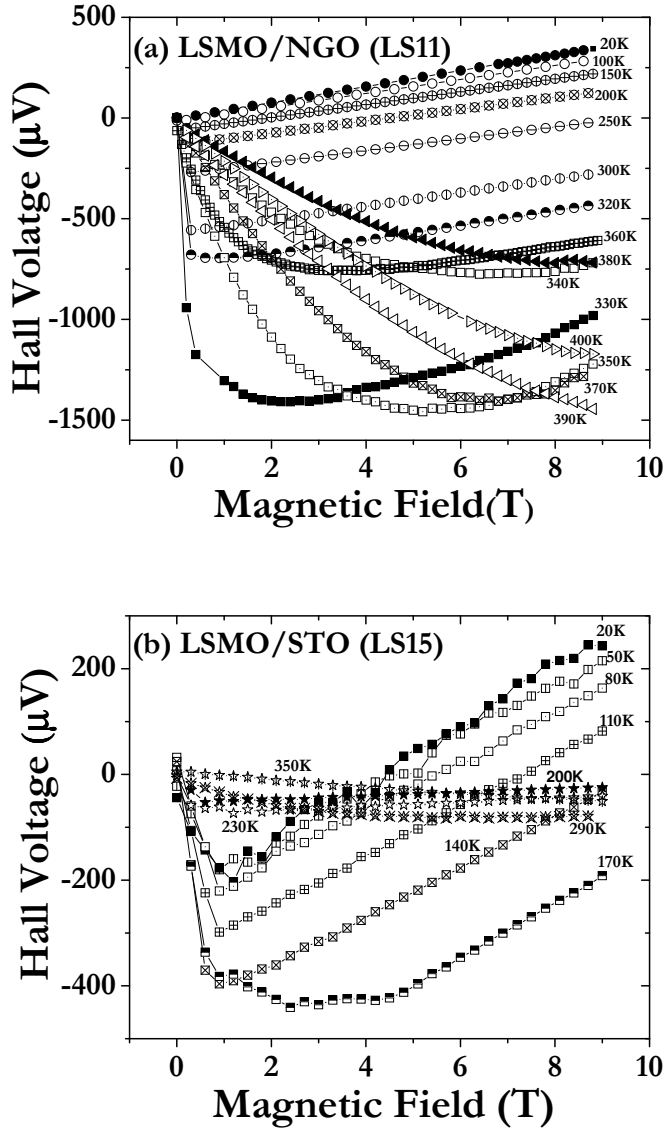


Figure 4.4: Hall voltage as function of magnetic field at constant temperature (as indicated) for the film of (a) 13 nm LSMO on NGO, called LS11. (b) 7 nm LSMO on STO, called LS15. The data is divided in three regimes; first regimes (indicated by circles) where Hall voltage is completely linear, 2nd regime (indicated by squares) both anomalous and linear part of Hall voltage, 3rd regime (triangles) behavior is totally anomalous.. For thin film on STO, the first region is missing and the anomalous behavior already starts at low temperature.

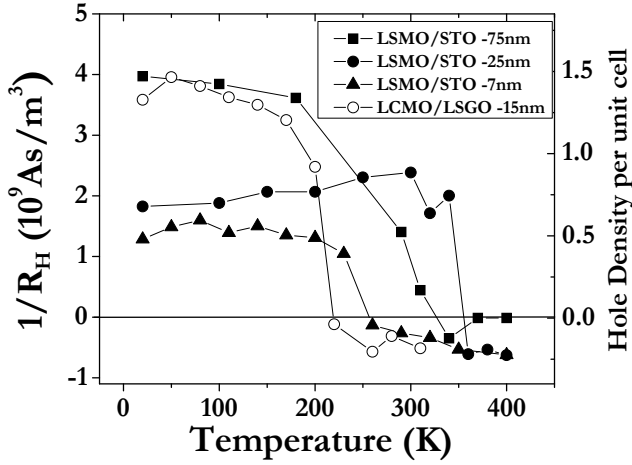


Figure 4.5: Inverse Hall resistance R_H (left hand scale) and hole density per unit cell (right hand scale) as function of temperature, for LSMO films with thicknesses 7 nm (LS15), 25 nm (LS8), 75 nm on STO, and an LCMO film of 15 nm on LSGO.

that T_p for the 25 nm film is already close to the bulk value. The high field data show the usual Colossal Magnetoresistance effect.

Next, the Hall voltage U_H was measured on these films as function of the magnetic field H_a applied perpendicular to the plane of the sample, and at different constant temperatures. In all cases the offset voltage was low, except for the case of 9 nm LCMO on STO. That sample will not be considered further. Figure 4.4 shows U_H for LS15 (the 7 nm film of LSMO on STO), as determined by taking the average of the measured voltage at $+H_a$ and $-H_a$. For this film T_p is around 230 K. Below T_p , U_H as function of increasing field first drops down, and then increases linearly. Around and above T_p , the crossover to linear behavior becomes less pronounced, and vanishes above 230 K. The behavior below T_p is usually understood from the relation

$$\rho_H = \frac{E_H}{J} = \frac{U_H d_F}{I} = \mu_0(R_H H_a + R_A M) \quad (4.1)$$

Here, E_H is the electric field, J the current density, I is the current, d_F is the film thickness, R_H the ordinary Hall coefficient and R_A the anomalous Hall coefficient. That can be due to the magnetization [23], but in manganites R_A appears to have a different origin, since its contribution grows with increasing temperature right up to the transition temperature. This behavior is well documented [15, 16, 18] and was ascribed to the carriers moving in a non-trivial background of core spins [24]. The positive slope seen in the data of Figure 4.4 signifies the hole character of the carriers. The value for R_H is determined from the linear part of the data for $U_H(H_a)$. For instance, at 20 K the slope is about $53 \mu\text{V}/\text{T}$ which, with a thickness

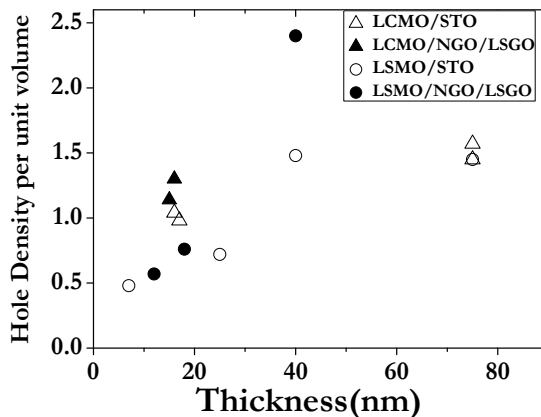


Figure 4.6: One-band hole density $n_{h,1}$ versus film thickness. Filled symbols show films on NGO/LSGO (triangles: LCMO; circles: LSMO), empty symbols show films on STO

of 7 nm and a measurement current of 500 μA yields $R_H = 7.5 \times 10^{-10} \text{ m}^3/\text{As}$. In a single band picture, the carrier density directly follows from $n_c = V_{uc}/(eR_H)$, with V_{uc} the unit cell volume and e the electron charge. Around T_c there is no large linear regime, and there we used the high-field part of the data above roughly 6 T. We are mainly interested in the low-temperature carrier density, but in this way the transition is clearly visible. In Figure 4.5, we show a representative set of data taken from different film-substrate combinations of $1/R_H$ and the hole density $n_{h,1}$ evaluated in a one band picture. In all cases there is a relatively steep rise around T_c of the film, followed by saturated behavior to low temperatures. At low temperatures, the 75 nm LSMO film on STO shows a value of $n_{h,1} \approx 1.5$, in line with previous reports on thick films. The 16 nm LCMO film on LSGO has $n_{h,1} \approx 1.3$, slightly lower than the bulk. The thin strained films deposited on STO show values around 0.7. In Figure 4.6 the values of $n_{h,1}$ for all samples are collected, taken at 20 K. The values and other characteristics of all samples are also collected in Table 4.1.

4.3.4 Hall Offset as a homogeneity parameter

A question which can be raised is whether these very thin and small films pose homogeneity problems which may yield inhomogeneous current distributions. It was noticed that for thin films of LCMO, less than 12 nm, it is not possible to perform reliable measurements because of the very large resistance at low temperature. Here, we find a relation between Hall offset and homogeneity of thin films of LSMO and LCMO.

Hall measurements always show a small offset. To avoid this offset, a magnetic

Film	substrate	thickness nm	T_p K	$1/R_H$ 10^9 C/m^3	$n_{h,1}$	$n_{h,2}$	μ_e/μ_h
LSMO	STO	75	325	4.0	1.45	0.55	0.8
LSMO	STO	40	370	4.1	1.48	0.55	0.8
LSMO	STO	25	370	2.0	0.72	0.32	0.3
LSMO	STO	7	250	1.3	0.48	0.2	0.3
LSMO	NGO	12	370	1.6	0.57	0.25	0.3
LSMO	STO	18	365	2.1	0.76	0.35	0.3
LSMO	STO	40	375	6.8	2.4	0.55	1.5
LCMO	STO	75	190	4.0	1.45	0.55	0.8
LCMO	STO	75	210	4.3	1.57	0.55	0.9
LCMO	STO	17	175	2.7	0.98	0.45	0.3
LCMO	STO	16	175	2.85	1.04	0.46	0.3
LCMO	NGO	15	210	2.9	1.14	0.53	0.3
LCMO	LSGO	15	245	3.7	1.3	0.55	0.7

Table 4.1: The Table shows type of film; type of substrate; film thickness; peak temperature T_p ; the value of $1/R_H$ taken at 20 K, and the corresponding value of the one-band hole density $n_{h,1}$. It also show the two-band hole density $n_{h,2}$ and the mobility ratio μ_e/μ_h determined in the following way: if $n_{h,2}$ can be fixed to 0.55, the mobility ratio is a free parameter; if no mobility ratio can be found to match 0.55, the ratio is fixed at 0.3.

field is applied in both directions and then averaging $+\Delta V_H$ and $-\Delta V_H$ gives the actual Hall voltage U_H . In the absence of magnetic field, the Hall offset (measured in Ohm) is found to be a good parameter to check the homogeneity of thin films of LSMO and LCMO.

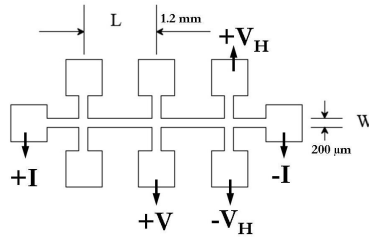


Figure 4.7: A standard Hall bar used to measure resistance in longitudinal configuration (shown as $+V$ and $-V_H$) and in Hall configuration (shown as $+V_H$ and $-V_H$).

Figure 4.8 shows the resistance measured in longitudinal configuration and Hall configuration (both are sketched in Figure 4.7) for a 12 nm thin film of LSMO on NGO. The longitudinal measurement shows T_{MI} at 380 K while the Hall offset follows the same trend but the resistance is about 2% of the longitudinal resis-

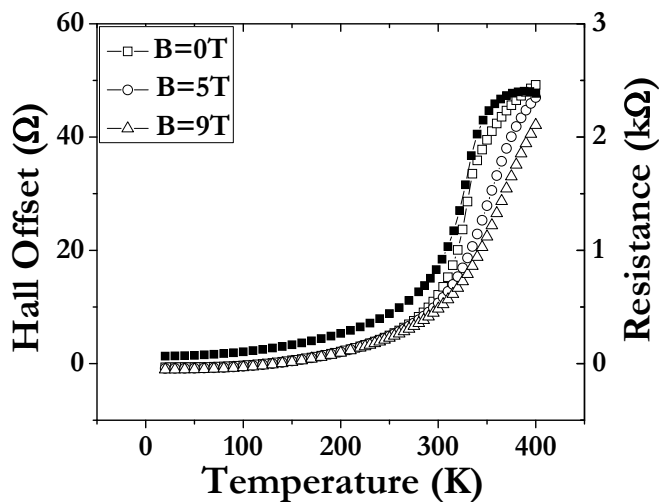


Figure 4.8: (Left axis, open symbols) Hall offset versus temperature in zero field, 5 T and 9 T for a 13 nm thin films of LSMO on NGO (LS11), (right axis, filled symbols) longitudinal resistance of the same sample.

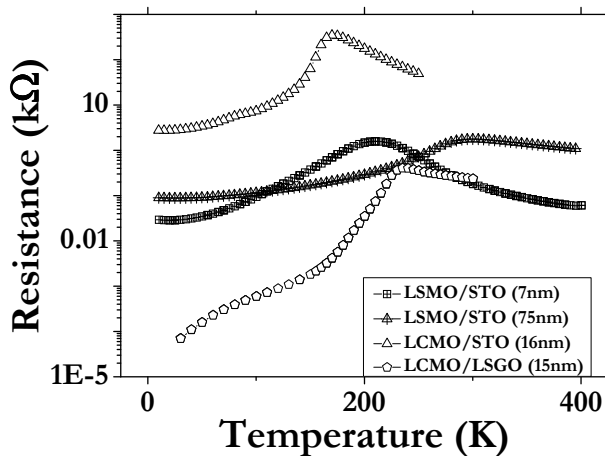


Figure 4.9: Temperature dependence of Hall offset for LSMO and LCMO films.

tance. Applying a magnetic field shows a small reduction in the Hall offset above 250 K. This is the first region in Figure 4.8a where the Hall voltage was found to be perfectly linear with the applied field. This behavior (reduced resistance and $\pm T_{MI}$) is found in all films of LSMO and LCMO except less than 15 nm films of LCMO.

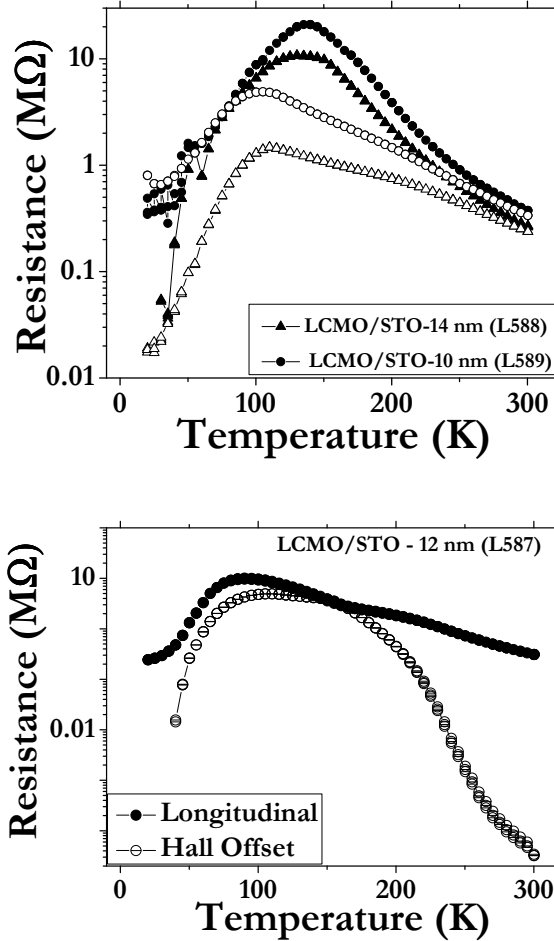


Figure 4.10: (a) Longitudinal resistance versus temperature for two films of LCMO on STO, a 14 nm (L588) and a 10 nm (L589) measured at 0 T (shown with filled symbols) and at 9 T (shown with open symbols), (b) Resistance versus temperature behavior for a 12 nm film measured in longitudinal and in Hall offset mode.

We showed in Figure 4.3 the resistance dependence on temperature for thin

films of LSMO and LCMO at 0 T and at 9 T. The Hall offset of these films is presented in Figure 4.9. For all homogenous LSMO and LCMO films, the Hall offset gives the T_{MI} with ± 40 K change as compared to T_{MI} measured in the longitudinal measurements. The main difference is that the resistance in the Hall offset is 50 times lower than the longitudinal resistance. The resistance in Hall offset increases for thin films but remains measurable. Ultrathin films of LCMO, less than 15 nm, show homogeneity problem because the resistance becomes very high at low temperature and the effect of the magnetic field is not as strong as in thicker films, as shown in Figure 4.10a. In these thin films, measuring the Hall offset gives a resistance with values very similar to the longitudinal resistance as shown in Figure 4.10b. We also find that for these films, it was not possible to measure linear U_H while for LSMO, even 7 nm thin film gives linear data as shown in Figure 4.4b. In LCMO thin films, a large resistance measured in Hall offset configuration cannot be only because of misalignment of contacts. Inhomogeneities persist in narrow bandwidth LCMO thin films more than the wider bandwidth LSMO and the charge carriers can be not dragged away due to inhomogeneous current distribution to measure U_H for thinner films.

4.4 Discussion

As we noted above, a one band picture is not appropriate to discuss Hall data. For a more complete discussion, we use the same starting point as done before, namely the band structure calculations of Pickett and Singh. They found a hole pocket of cubic shape, containing 0.55 holes and centered around the R -point of the Brillouin zone (the corner point of a simple cube); and an electron pocket of spherical shape, containing 0.05 electrons and centered around the Γ point [20, 25]. This was confirmed by other calculations as well as by several experiments. In particular Livesay *et al.* reported similar calculations and experimentally verified the presence and shape of both Fermi Surfaces (FS) by positron annihilation [26] on a single crystal of $\text{La}_{0.7}\text{Sr}_{0.3}\text{MnO}_3$. Photoemission studies on thin films (40 nm) of $\text{La}_{1-x}\text{Sr}_x\text{MnO}_3$ grown on NGO confirmed the existence of the Γ -centered electron pocket for $x = 0.3$ [27]. This film was slightly strained, and it is important to note that in such films this part of the FS still exists. In photoemission no clear evidence is found for the hole-type FS, as discussed in Ref. [28].

In the two-band picture, the relation between the measured Hall resistance R_H and the two carrier densities is as follows:

$$R_H = \frac{r_h n_h \mu_h^2 - r_e n_e \mu_e^2}{e(n_h \mu_h + n_e \mu_e)^2} \quad (4.2)$$

Here, $n_{h,e}$ are the hole, electron densities, $\mu_{h,e}$ are the hole, electron mobilities, and $r_{h,e}$ are factors taking the shape of the FS into account, with $r = 1$ for a spherical surface and $r = 1/2$ for a cubic surface [29]. The shape factors were used by Chun *et al.* in their analysis [16], but not by Jacob *et al.* [15], nor by Bibes *et al.* [30]. For our analysis, the shape factors turn out to be important.

In order to work with Eq. 4.2, several assumptions have to be made. Taking the Pickett-Singh carrier densities, we can resolve for the mobility ratio μ_e/μ_h using the measured R_H . For the three 75 nm LCMO and LSMO films on STO, we find mobility ratios of 0.8 and 0.9, which is of the same order of magnitude as found before [16]. The actual numbers are given in Table 4.1.

When we try the same for the data with lower values of $1/R_H$ (and therefore n_h) however, we cannot find reasonable values for μ_e/μ_h which would reproduce the Pickett-Singh densities of 0.55 (n_h) and 0.05 (n_e). This is shown pictorially in Figure 4.11 where we plot the values of $n_{h,2}$ versus $V_{uc}/(eR_H) = n_{h,1}$ for different values of μ_e/μ_h .

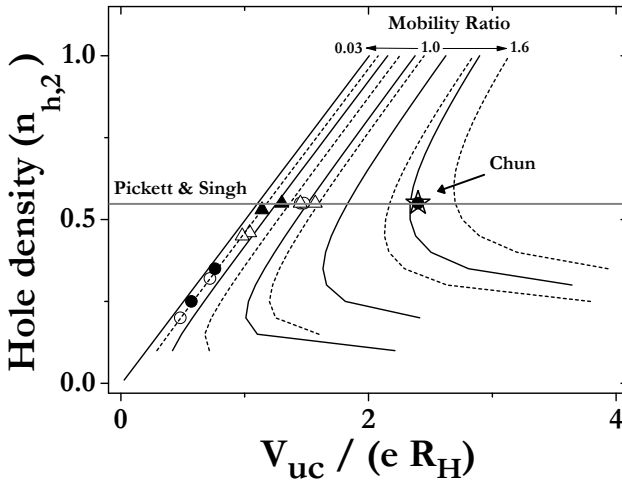


Figure 4.11: The two-band hole density $n_{h,2}$ plotted as function of V_{uc}/eR_H , with the contours showing different values of the mobility ratio μ_e/μ_h . Contours are given at mobility ratios 0.03, 0.3, 0.5, 0.7, 0.9, 1.0, 1.2, 1.4, 1.5, 1.6. For $V_{uc}/(eR_H) = n_{h,1} > 1.2$, its value is fixed at the Pickett-Singh value of 0.55. Below $n_{h,1} = 1.2$, data are plotted on the $\mu_e/\mu_h = 0.3$ contour. Filled symbols show films on NGO / LSGO (triangles: LCMO; circles: LSMO), empty symbols show films on STO. The single crystal data of Chun *et al* [16] is plotted with an asterisk.

The Figure firstly shows the solution of Chun *et al.* for their single crystal, namely a mobility ratio of about 1.5 at a Hall resistance corresponding to $n_{h,1} = 2.4$. It also shows the asymptote which is found when μ_e/μ_h goes to zero, which is the reason that for values below roughly $V_{uc}/(eR_H) = n_{h,1} = 1.2$, no solution can be found which reproduces the Pickett-Singh carrier densities. For the 75 nm samples, the mobility ratio is seen to be about 1. For samples with $n_{h,1}$ below 1.2 we plot them at a mobility ratio of 0.3, which means we allow for a factor 3 change in the ratio. As can be seen in the Figure, this leads to a decrease of

$n_{h,2}$ from 0.55 to about 0.25. The conclusion from the analysis therefore is that in the 2-band model, and using $r = 1/2$, the data in particular for the thinnest films cannot be described by changing only the mobility ratio, but that the carrier density also has to be lower. This is somewhat different when $r = 1$ is used for the hole pocket. Solutions are then possible down to $n_{h,1} \approx 0.6$. However, the single crystal experiments of Chun *et al* cannot be described in this way, and the spread of mobility ratio's which describe our samples becomes large : from 0.3 at $n_{h,1} = 0.6$ to 2.5 at $n_{h,1} = 1.5$, roughly an order of magnitude, while the 7 nm LSMO on STO still cannot be described.

Generally, the LSMO films show a significantly decreased carrier density even when the mobility ratio is lowered to 0.3, while the LCMO films show a smaller decrease, of the order of 10%. However, lowering the value of μ_e/μ_h from 1.5 to 0.3 is not completely physical, because of the following. From the band structure calculations it was found that the holes are very light ($m_h \approx 0.6m^*$, m^* the bare electron mass), while the electrons are very heavy ($m_e \approx 14m^*$). A lower μ_e/μ_h would mean a still *larger* value of m_e and/or a still *smaller* value of m_h , which seems unlikely. On the other hand, a higher μ_e/μ_h means a lower carrier density. The analysis therefore strongly indicates that for both LSMO and LCMO films the carrier density of films of roughly 20 nm or less is significantly smaller than in the bulk. The one exception is the 15 nm LCMO film on LSGO, which can be described with parameters still close to the bulk values.

For all substrate/film combinations, therefore, the number of measured carriers becomes smaller for thin films, also in the field of 9 T used in the measurements. Looking separately at LSMO and LCMO, we see from Table 4.1 that for LSMO, there is a monotonic decrease of $n_{h,2}$ with thickness, and that the film on NGO does not behave differently from the films on STO. Here we come back to the issue of the dead layers, already signaled in section 2.3.2. Such a dead layer of about 4 nm is well documented for LSMO/STO [31] and LSMO/NGO [32]. If we assume that this layer does not contribute carriers (even in 9 T), but that above the critical thickness d_{cr} the carrier contribution is bulk like, then the thickness-averaged carrier density is given by $\bar{n}_{2,h} = n_{2,h}^{bulk} (1 - d_{cr}/d)$. At the smallest thickness of 7 nm, this leads to an average value of 0.4 times the bulk value, in very good agreement with the number from the analysis.

Also for LCMO, dead layers of the order of 5 nm have generally been reported [11,21]. In this case the analyzed reduction at 15 nm is less, of the order of 10 % - 20 %, and also less than the 30 % which might be expected on the basis of the dead layer. Assuming that the mobility ratio has changed less than to 0.3 would remedy this. On the whole, the data indicate that both for wider and smaller bandwidths, and irrespective of strain, the interface effects are significant, and stretch over a number of nanometers. The cause of this effect may well lie in a charge transfer due to a charge discontinuity, very similar to what is intensively researched on the LAO/STO interface [36]. Just as the polar LaAlO_3 consists of charged blocks of $(\text{LaO})^{1+}$ and $(\text{AlO}_2)^{1-}$, the LSMO layer consists of blocks $[(\text{La}_{0.7}\text{Ca}_{0.3}\text{O}_3)]^{0.7+}$ and $(\text{MnO}_2)^{0.7-}$ which cause a charge discontinuity at the interface with STO. In the case of LSMO/STO dead layer, an explanation was given in terms of an

orbital reconstruction [33], accompanied by a slight increase in the amount of Mn^{3+} ions [34]. We have similar evidence of Mn^{3+} enrichment from Electron Energy Loss Spectroscopy (EELS) at the interface of LCMO/STO [35]. Particularly interesting in this respect is the case of LCMO on LSGO, where we do not find carrier loss, since this would also fit the charge discontinuity picture. For LAO and NGO, the charge of the blocks is (+1,-1). For LSGO it is half that value, because of the mixed La,Sr valence, and therefore closest in charge matching to the LSMO layer. The LSGO substrate is therefore expected to give the smallest effect.

In conclusion, the data fit a model in which an active manganite layer occurs above a critical thickness. This active layer contains a bulk-like amount of carriers, although T_p can be significantly lower, which is the result of strain.

4.5 Anomalous Hall effect

In ferromagnetic materials, an additional voltage is produced due to the embedded magnetic moments which causes asymmetric scattering of current carrying electrons, called anomalous Hall voltage. The anomalous Hall coefficient, denoted as R_A in Eq. 4.1 has a straightforward relation with the Hall resistivity but is theoretically difficult to explain, and has remained poorly understood. The anomalous Hall effect (AHE) in manganites for thick films [15, 30] and single crystals [14, 16] was studied but not in thin films of manganites. In chapter 2, we gave some the background and theories related to anomalous Hall effect. In this section, we discuss the contribution of anomalous Hall effect (AHE) in thin films of LSMO and LCMO.

We saw in Figure 4.4 that in the low temperature and high field regime, the anomalous contribution is minimum because of saturation of magnetic domains. The Hall voltage remains linear and we find out the ordinary Hall co-efficient R_H almost constant. With increase in temperature, R_H increases and R_A also increases. In the low field regime, the anomalous Hall contribution is dominant and it arises from two different elementary processes, skew scattering and side jump. Skew scattering describes the average deflection of the trajectory of a charge carrier in a scattering event and a side jump mechanisms is ascribed to the displacement of the trajectory from its original path through the scattering center. These two processes are linked to the longitudinal resistivity and anomalous Hall coefficient through a power law $R_A \mu_o M = \gamma \rho_{xx}^n$. For the skew scattering process, $n=1$ while $n = 2$ for the side jump mechanism. To find the value of n in thin films, we rearrange Eq. 4.1 as

$$\rho_H^* = \mu_o R_A M \quad (4.3)$$

where $\rho_H^* = \rho_H - \mu_o R_H H_a$.

For all grown films shown in Table 4.2, the Curie temperature and saturation magnetization were measured as shown in Figure 4.12. The anomalous Hall contribution is determined by extrapolating the linear high field data at 9 T, back to zero field. A double logarithmic plot of ρ_H^* (9 T) versus $R_A = \rho_H^*/(\rho_H M_{sat})$

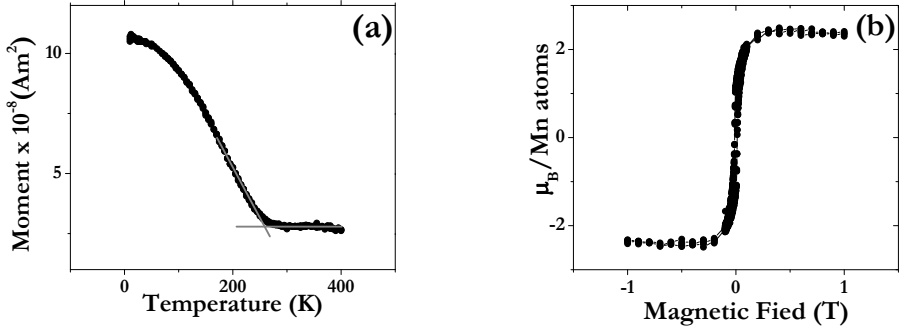


Figure 4.12: (a) Temperature dependence of magnetization for a 7 nm thin film of LSMO on STO (LS15) (b) Field versus magnetization for the same film shown in (a) at 10 K.

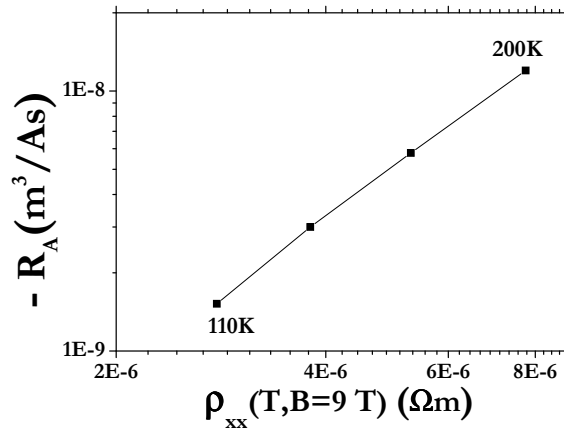


Figure 4.13: Anomalous Hall coefficient versus longitudinal resistivity ρ_{xx} at $B=9$ T for a 15 nm thin film of LCMO on LSGO.

is plotted in Figure 4.13 for a 15 nm thin film of LCMO on LSGO (L600). This gives a perfect power law in the ferromagnetic regime, with an exponent $n = 2$. To take into account the magnetoresistive effects, data points at temperatures close to T_c and T_p are included and smaller than 50 K are excluded to find out power factor [15]. We have determined the power n for thin films of LSMO and LCMO on STO and LSGO substrates as shown in Table 4.2. We observe that thick films of LSMO and LCMO (75 nm) on STO as well as LCMO on LSGO give $1.5 \leq n \leq 2.1$. The same value for n is found in literature and it is claimed that the side

jump mechanisms is dominant in manganites [15]. For thin films which are strained and show a reduction in *average* carrier density, the power factor n is close to 1. The skew scattering seems to play a role in thin strained films. It is required to develop theoretical models to find out the scattering mechanisms in very thin films of manganites.

Film	substrate	thickness nm	T_p K	T_c K	μ_B/Mn	$n_{h,1}$	n
LSMO	STO	75	325	312	2.4	1.45	2.1
LSMO	STO	25	370	340	2.5	0.72	1
LSMO	STO	7	250	243	2.1	0.48	0.9
LCMO	STO	75	190	177	2.8	1.45	1.5
LCMO	STO	75	210	200	2.8	1.47	1.6
LCMO	STO	16	175	170	2.4	1.04	1.0
LCMO	LSGO	15	245	242	2.1	1.3	2

Table 4.2: The Table shows type of film; type of substrate; film thickness; peak temperature T_p ; Curie Temperature (K) at 1 mT for all films except for 25 nm LSMO on STO which was measured at 10 mT; Bohr magneton μ_B/Mn , hole density $n_{h,1}$ in one band model and power factor n , related to Hall and longitudinal resistivity.

4.6 Conclusion

In conclusion, we have shown that, even though the inverse Hall constant cannot be directly connected to a carrier density since a one band picture does not apply, also an analysis in a two-band scenario shows that the *average* carrier density decreases both in LSMO and LCMO films when they become thinner. Strain does not appear to be the main driver. Rather, the data taken with different substrates indicate interface effects, in line with current models for charge discontinuities. The range of these effects appears to be a few nanometer. The utilization of Hall offset for homogeneous thin films is described. The AHE is found to have different scattering processes for thicker/relaxed and thin/strained films.

Bibliography

- [1] E. Dagotto, T. Hotta, and A. Moreo, Phys. Rep. **344**, 1 (2001)
- [2] M.B. Salamon and M. Jaime, Rev. Mod. Phys. **73**, 583 (2001).
- [3] Y. Tokura, Rep. Prog. Phys. **69**, 797 (2006).
- [4] A.J. Millis, Nature **392**, 147 (1998).
- [5] C. Zener, Phys. Rev. **82**, 403 (1951).
- [6] P.W. Anderson and H. Hasegawa, Phys. Rev. **100**, 67 (1955).
- [7] H.Y. Hwang, T.T.M. Palstra, S.-W. Cheong and B. Batlogg, Phys. Rev. B **52**, 15046 (1995).
- [8] Y. Konishi, Z. Fang, M. Izumi, T. Mamako, M. Kasai, H. Kuwahara, M. Kawasaki, K. Terakura and Y. Tokura, Jn. Phys. Soc. Japan **68**, 3790 (1999).
- [9] Z. Fang, I.V. Solovyev, and K. Terakura, Phys. Rev. Lett. **84**, 3169 (2000).
- [10] J. Aarts, S. Freisem, R. Hendrikx and H.W. Zandbergen, Appl. Phys. Lett. **72**, 2975 (1998).
- [11] M. Bibes, Ll. Balcells, S. Valencia, J. Fontcuberta, M. Wojcik, E. Jedryka, and S. Nadolski, Phys. Rev. Lett. **87**, 067210 (2001).
- [12] Z.Q. Yang, R. Hendrikx, J. Aarts, Y.L. Qin and H.W. Zandbergen, Phys. Rev. B **70**, 174111 (2004).
- [13] A.J. Millis, T. Darling and A. Migliori, J. Appl. Phys. **83**, 1588 (1998).
- [14] A. Asamitsu and Y. Tokura, Phys. Rev. B **58**, 47 (1998).

- [15] G. Jakob, F. Martin, W. Westerburg and H. Adrian, *Phys. Rev. B* **57**, 10252 (1998).
- [16] S.H. Chun, M.B. Salamon and P.D. Han, *Jn. Appl. Phys.* **85**, 5573 (1999).
- [17] G.J. Snyder, R. Hiskes, S. DiCarolis, M.R. Beasley and T.H. Geballe, *Phys. Rev. B* **53**, 14434 (1996).
- [18] P. Matl, N.P. Ong, Y.F. Yan, Y.Q. Li, D. Studebaker, T. Baum and G. Doubinina, *Phys. Rev. B* **57**, 10248 (1998).
- [19] N.G. Bebenin, R.I. Zainullina, N.S. Bannikova, V.V. Ustinov, Y.M. Mukovskii, *Phys. Rev. B* **68**, 064415 (2008).
- [20] W.E. Pickett and D.J. Singh, *Phys. Rev. B* **55**, R8642 (1997).
- [21] Z.Q. Yang, R. Hendrikx, J. Aarts, Y. Qin, and H.W. Zandbergen, *Phys. Rev. B* **67**, 024408 (2003).
- [22] C. Beekman, I. Komissarov, M. Hesselberth and J. Aarts, *Appl. Phys. Lett.* **91**, 062101 (2007).
- [23] R. O`Handley, *Modern Magnetic Materials*, Wiley and Sons, New York, 2000.
- [24] J. Ye, Y.B. Kim, A.J. Millis, B.I. Shraiman, P. Majumdar, and Z. Tesanovic *Phys. Rev. Lett.* **83**, 3737 (1999).
- [25] W.E. Pickett and D.J. Singh, *Jn. Magnetism and Magn. Materials* **172**, 237 (1997).
- [26] E.A Livesay, R. N West, S. B Dugdale, G. Santi and T. Jarlborg, *J. Phys. Cond. Mat.* **11**, 1279 (199).
- [27] A. Chikamatsu, H. Wadati, H. Kumigashira, M. Oshima, A. Fujimori, M. Lippmaa, K. Ono, M. Kawasaki and H. Koinuma, *Phys. Rev. B* **76**, 201103 (2007).
- [28] M. Shi, M.C. Falub, P.R. Willmott, J. Krempasky, R. Herger, L. Patthey, K. Hricovini, C.V. Falub and M. Schneider, *J. Phys. Cond. Mat.* **20**, 222001 (2008).
- [29] R.S. Allgaier, *Phys. Rev.* **165**, 775 (1968).
- [30] M. Bibes, V. Laukhin, S. Valencia, B. Martínez, J. Fontcuberta, O. Yu. Gorbenko, A. R. Kaul, and J L Martínez, *J. Phys. Cond. Mat.* **17**, 2733 (2005).
- [31] M. Huijben, L.W. Martin, Y.-H. Chu, M.B. Holcomb, P. Yu, G. Rijnders, D.H.A. Blank, and R. Ramesh, *Phys. Rev. B* **78**, 094413 (2008).
- [32] J.Z. Sun, D.W. Abraham, R.A. Rao, and C. Eom, *Appl. Phys. Lett.* **74**, 3017 (1999).

- [33] A. Tebano, C. Aruta, S. Sanna, P.G. Medaglia, G. Balestrino, A.A. Sidorenko, R. De Renzi, G. Ghiringhelli, L. Braicovich, V. Bisogni and N.B. Brookes, *Phys. Rev. Lett.* **100**, 137401 (2008).
- [34] J.-S. Lee, D.A. Arena, P. Yu, C.S. Nelson, R. Fan, C.J. Kinane, S. Langridge, M.D. Rossell, R. Ramesh, and C.-C. Kao, *Phys. Rev. Lett.* **105**, 257204 (2010).
- [35] C. Beekman, M. Porcu, and H.W. Zandbergen, and J. Aarts, arXiv:1102.4004v1 [cond-mat.mes-hall].
- [36] O. Ohtomo and H.Y. Hwang, *Nature* **427**, 423 (2004).

Mesoscopic transport in thin films of $\text{La}_{0.67}\text{Sr}_{0.33}\text{MnO}_3$

5.1 Introduction

The correlations among electrons in perovskite manganite thin films offer a broad framework to study their physical properties. The properties can be influenced by introducing structural defects (by strain), chemical and compositional defects (doping level, oxygen content and stoichiometry). Epitaxial thin films can behave quite different from polycrystalline thin films and single crystals. In epitaxial thin films, strain is an inherent property and it strongly affects the transport and magnetic properties [1–6]. In polycrystalline thin films, the size of grains and grain boundaries can induce subtle changes in properties of films, and microstructured and nanostructured grainy systems are well studied [7–12]. In epitaxial thin films of manganites, an area which is not much explored is the electronic transport in reduced dimensions. By reducing these to microscopic length scales, the properties can be significantly different from those in textured and epitaxial thin films. An example of this was found in (narrow band) $\text{La}_{0.7}\text{Ca}_{0.3}\text{MnO}_3$ on SrTiO_3 , where mesoscopic bridges (typical width 1–5 μm) showed strongly non-linear behavior of the current-voltage characteristics in the temperature interval of the Metal-Insulator transition [13]. The effect was attributed to the melting of a glassy polaron state which is sensitive to the injection of electrons and which forms while going from the correlated metal to the polaronic liquid [14], in line with the details of the electronic phase diagram of $(\text{La,Ca})\text{MnO}_3$ [15]. This gives rise to the question whether similar behavior can be found in a wider bandwidth material, which is the subject of this chapter.

We investigate thin films of $\text{La}_{0.7}\text{Sr}_{0.3}\text{MnO}_3$ grown on SrTiO_3 in which bridges of 100 μm long and 1 μm or 300 nm wide (distance between voltage contacts was 25 μm) were defined lithographically. In bridges of 1 μm , we find the current-voltage characteristics to be perfectly linear (ohmic) over the full temperature

range between 400 K and 10 K. Strong non-linearities however are observed for a 300 nm wide bridge in the temperature regime below the transition temperature. The non-linearities are present even when applying a high magnetic field of 9 T.

5.2 Experimental

Thin films of $\text{La}_{0.7}\text{Sr}_{0.3}\text{MnO}_3$ (LSMO) were deposited on SrTiO_3 (STO) (001) substrates using dc reactive sputtering in pure oxygen environment at pressure of 2.2 mbar. The films were deposited in the thickness range between 6 nm and 42 nm. All films were characterized by atomic force microscopy (AFM) in tapping mode after deposition. Figure 5.1a and b show morphology and height variation of a 17 nm thick film of LSMO on STO, called LS32. The roughness of the film is 2.1 nm and it has step-height variations of the order of a unit cell (0.4 nm). Figure 5.1c,d show the surface morphology and the height variation perpendicular to the terraces of a 6 nm-thick film of LSMO on STO, called LS41. The step variation is again 0.4 nm but the roughness of film is low, 0.4 nm, a bit smoother than the thicker film in Figure 5.1a.

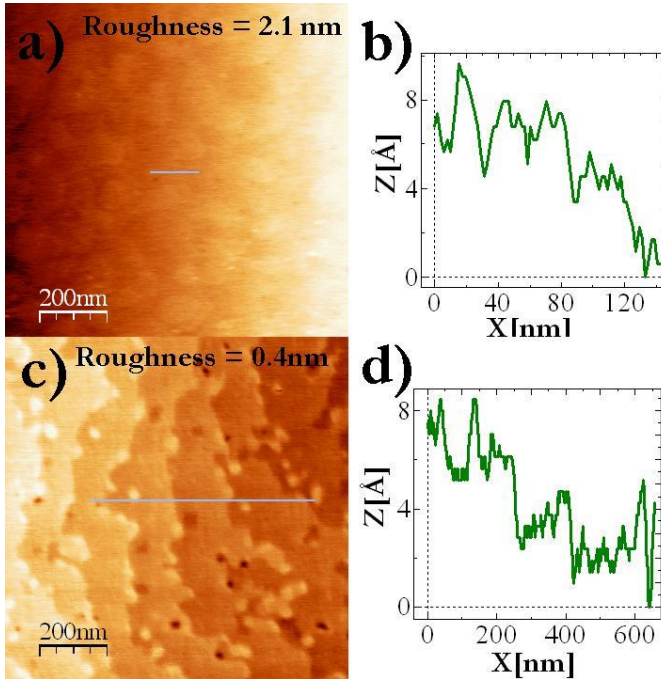


Figure 5.1: Surface morphology of (a) a 17 nm film of LSMO on STO (LS32), (b) height variation of (a) along the drawn line, (c) a 6 nm film of LSMO on STO (LS41), (d) height variation of (c) along the drawn line.

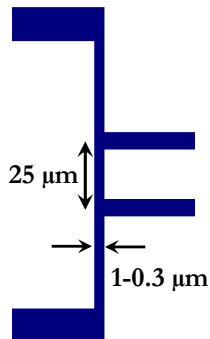


Figure 5.2: The structure of patterned bridges of LSMO on STO. The length of the bridge is 100 μm and the distance between voltage contacts is 25 μm .

The film thickness was measured by x-ray reflectivity, using $\text{Cu-K}\alpha$ radiation. The lattice mismatch between bulk LSMO ($a_c = 0.3873 \text{ nm}$) thin films and single crystal STO substrates (001) ($a_c = 0.3905 \text{ nm}$) is -0.82% . Thin films grown on STO are therefore strained. The strain gradually relaxes with increasing thickness.

The films were patterned using e-beam lithographic technique. A three-step process was used to pattern LSMO microbridges of 1 μm and 300 nm wide with Au contact pads. A typical structured pattern for the microbridges is shown in Figure 5.2. In the first step, gold markers were written to have a better contrast with STO substrates. A bilayer of PMMA/MMA was spun on top of the samples and baked at $180^\circ\text{C}/120^\circ\text{C}$ respectively for 90/90 seconds. Then markers were written with e-beam. After developing, the samples were sputtered with gold and the lift-off process was accomplished. In the second step, a negative resist (MaN2405) was spun onto the sample, and baked at 90°C for 10 minutes. Then the chip of LSMO was written with e-beam with Au markers as reference. After developing, the sample was etched with wet etching. The chemicals used for wet etching and their respective quantities were ($\text{H}_2\text{O} : \text{HF} : \text{HCl} : \text{HNO}_3 = 25 : 1 : 1 : 1$). The etch rate was 2 nm per second for the LSMO thin films. Lastly, the first step was repeated for making Au contacts. A physical properties measurement system (PPMS) was used for the temperature and field control. External current sources and voltmeters were used for the transport measurements of unstructured and structured thin films and for the current-voltages characteristics.

5.3 Results

1 μm wide bridges

Figure 5.3 shows the transport properties of two thin films of LSMO on STO of (a) 17 nm and (b) 6 nm measured with 1 μA current. The unstructured samples

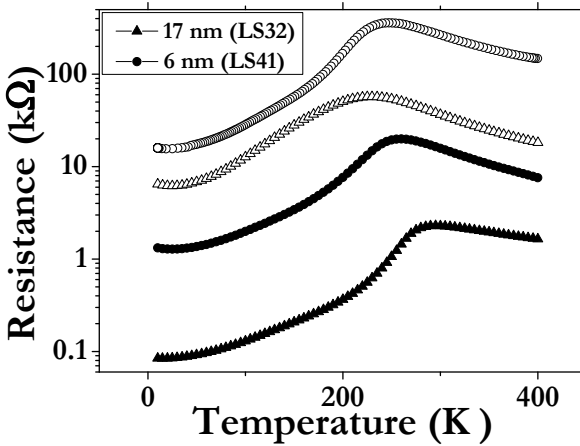


Figure 5.3: Resistance versus temperature behavior for two films of LSMO on STO (a) a 17 nm film (LS32) (b) a 6 nm film (LS41). Closed symbols are for unstructured films. Open symbols denote $R(T)$ for $1 \mu\text{m}$ wide bridges. The measurement current is $1 \mu\text{A}$ for all films shown here.

have a transition temperature of about 290 K and 250 K as compared to the bulk LSMO 370 K. Both films are strained as measured by XRD. The strain reduces the transition temperature by about 100 K. There is not much difference between unstructured and structured films except that the low-temperature resistance is increased about 100 times for the 17 nm film and only about 10 times for the 6 nm film, although the resistance of the 17 nm film is still lower than that of the 6 nm film.

To further explore the behavior of LSMO on micrometer scales, we measured the current-voltage characteristics at different temperatures for thin films of LSMO between 6 nm and 42 nm. For all $1 \mu\text{m}$ bridges, we observe a perfect linear behavior while measuring IV-curves for the whole temperature range. We show in Figure 5.4 the IV curves for a 17 nm thin film of LSMO/STO for a $1 \mu\text{m}$ wide bridge. The data are presented as current density, where the cross-section is taken as $17 \text{ nm} \times 1 \mu\text{m}$. The same behavior is found for the other films, including the 6 nm thick film (LS41). The derivatives of these curves are shown in Figure 5.5. The non-linearities found in LCMO microbridges [13] are clearly not found here.

300 nm wide bridges

Going from a width of $1 \mu\text{m}$ to a bridge of 300 nm, the behavior changes quite drastically. Figure 5.6 shows the $R(T)$ behavior of three films of LSMO on STO. The 42 nm thick film (LS38) does not show unusual behavior, with a peak temperature above 300 K both for structured and unstructured ones. The 10 nm thin film

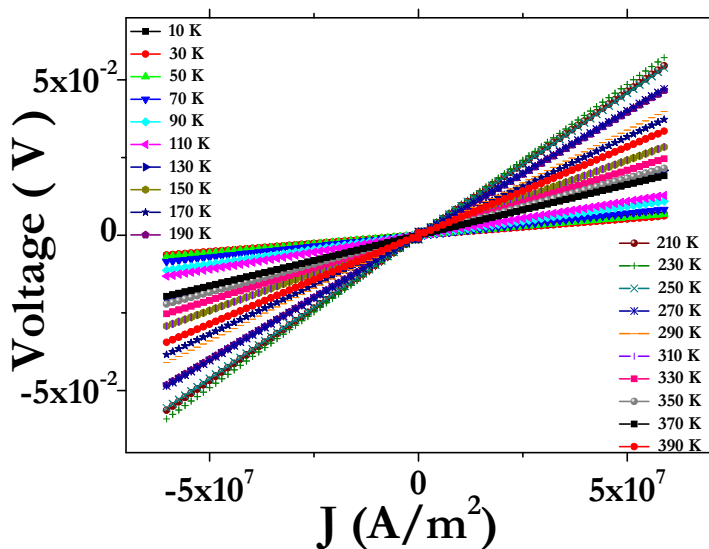


Figure 5.4: Current voltage characteristics for a 17 nm thin film of LSMO on STO (LS32) with a 1 μm wide bridge. The current density was calculated from the 17 nm \times 1 μm cross-section of the bridge.

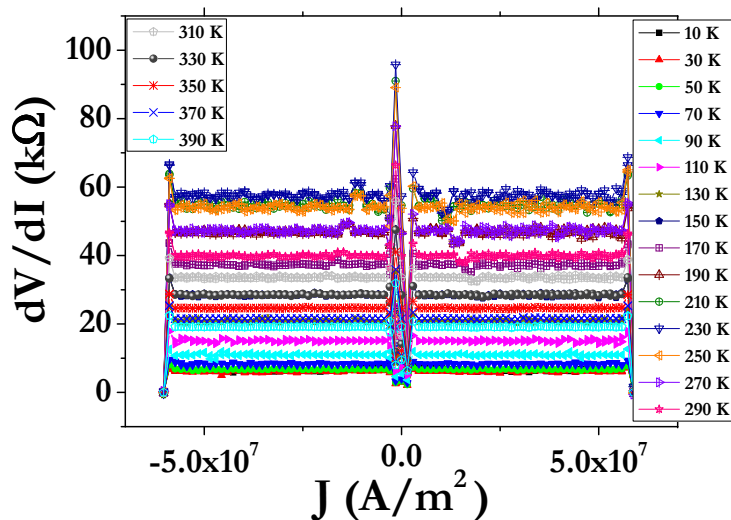


Figure 5.5: Derivatives of current-voltage curves for a 17 nm thin film of LSMO on STO (LS32) for the 1 μm wide bridge shown in Figure 5.4. The peak structure around zero current is due to a discontinuity in the source current.

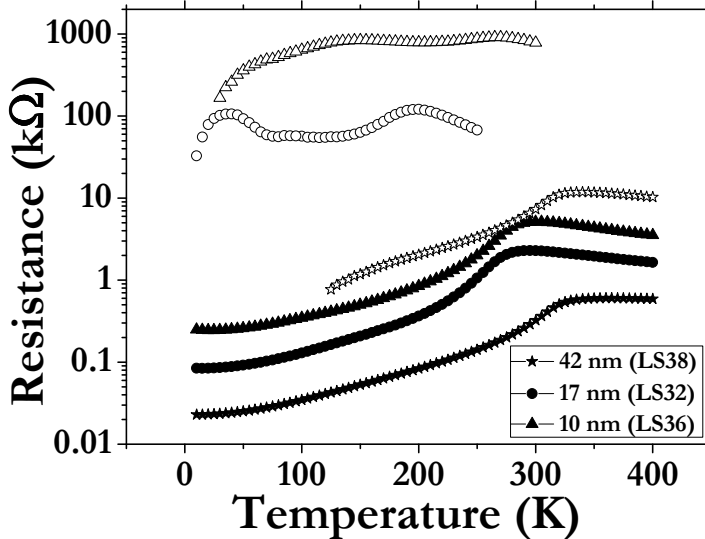


Figure 5.6: Temperature dependence of the resistance for 300 nm wide bridge of LSMO thin films with different thickness of 42 nm (LS38), 17 nm (LS32) and 10 nm (LS36). The unstructured films are shown with filled symbols and the 300 nm bridges films are shown with open symbols. The measurement current is $1 \mu\text{A}$ for all films shown here except for the unstructured LS38, measuring current is $10 \mu\text{A}$.

(LS36) shows a small upturn at low temperature and the peak temperature goes down to 250 K while the unstructured film has T_p around 300 K. The 17 nm thin film (LS32) has two resistance peaks. One lies at 185 K which can be considered as T_p ; the peak around 50 K does not have a straightforward origin. Note that the resistance of the 10 nm film is about an order of magnitude larger than the resistance of the 17 nm film over most of the temperature range.

We further explored the characteristic in 300 nm wide bridges by measuring IV curves. The 10 nm film (LS36) with the 300 nm wide bridge is shown in Figure 5.7. Here, we observe strong nonlinearities which start around 40 K and continue until 190 K. The derivatives of such IV curves are shown in Figure 5.8 which clearly divide the nonlinear behavior into three different regions. These effects are not found in the 42 nm film with the 300 nm bridge. The first region is between 10 K to 40 K (Figure 5.8a) where ohmic behavior can be seen. The second region between 50 K and 150 K (Figure 5.8b) shows a strong peak at the zero bias, indicating a strong nonlinear behavior. In the third region which starts around 200 K, the nonlinear behavior becomes shallow and after T_p , nonlinearities disappear fully. We see same trend of nonlinearity in 17 nm thin film of LSMO for the 300 nm wide bridge.

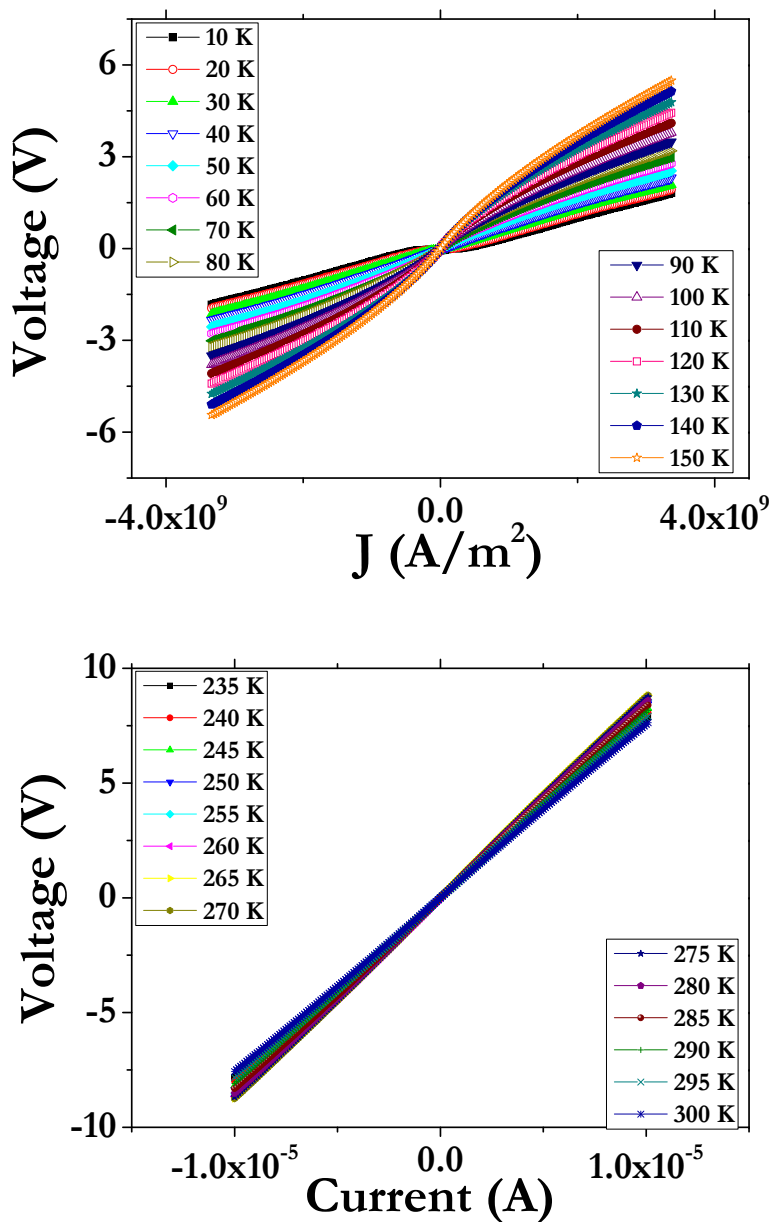


Figure 5.7: Current voltage characteristics for a 10 nm thin film of LSMO on STO (LS36) for 300 nm wide bridge. The current density was calculated from the $10 \text{ nm} \times 300 \text{ nm}$ cross-section of the bridge.

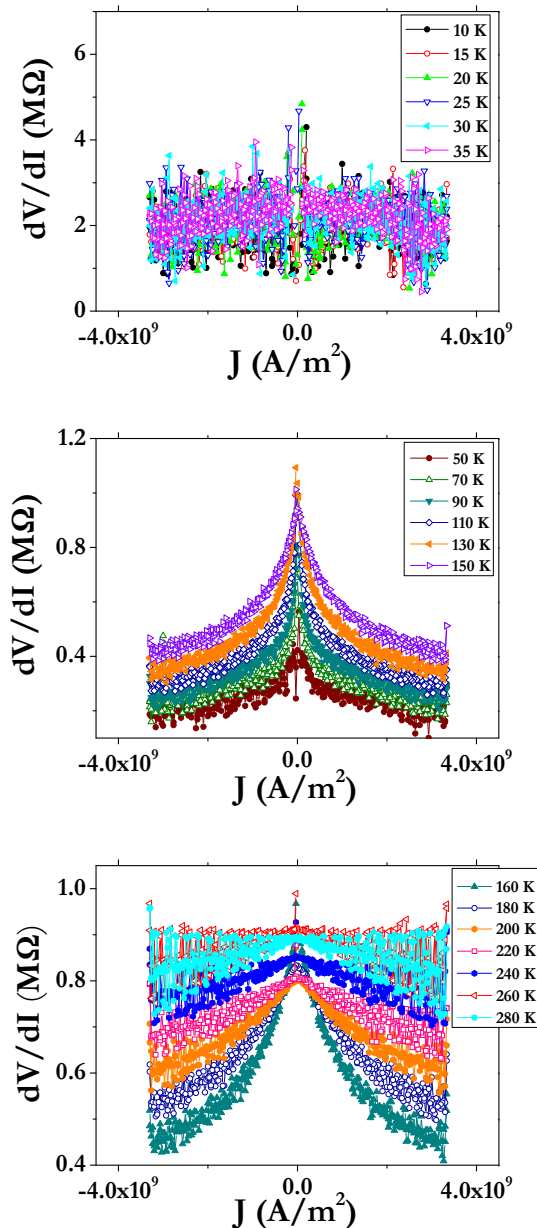


Figure 5.8: Derivatives of some of current-voltage curves shown in Figure 5.7 for the 10 nm thin film of LSMO on STO (LS36) with a 300 nm wide bridge. (a) first region 10 K to 40 K, fully linear (b) second region between 50 K and 150 K, strongly nonlinear (c) third region after 180 K, slightly nonlinear and nonlinearity disappears with increasing temperature.

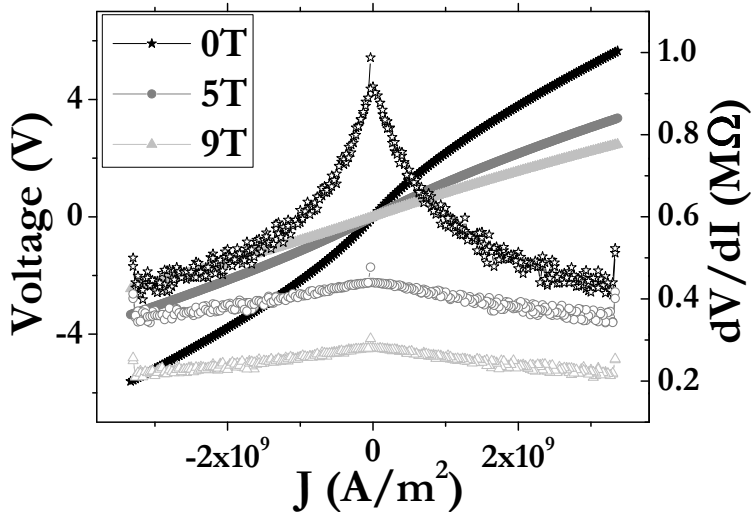


Figure 5.9: Effect of magnetic field on 300 nm wide bridge of a 10 nm film (LS36) of LSMO on STO at 155 K. Left axis shows the voltage and right axis is for the derivatives taken from the IVs curves.

The effect of an applied magnetic field on these IV curves is shown in Figure 5.9 for the 10 nm (LS36) film at 155 K. The strongest effect was obtained at 0 T. The left axis shows IV-curves and derivatives are shown on right axis. The nonlinear behavior is strongly reduced by applying a high magnetic field.

The nonlinear effects can also be displayed as $R(T)$ at different currents as shown in Figure 5.10. The current has no significant effects on a 42 nm thick film of LSMO but for thin films, increasing the current decreases the resistance. These effects are consistently seen in thin films structured into 300 nm wide bridges. Looking at Figure 5.10c (the 10 nm film again), it is also here clear that the nonlinear behavior is strongest in the region of 50 K to 150 K, where different current give a significantly different resistance.

5.4 Discussion

Nonlinear IV characteristics at temperatures below the IM transition have been observed in two types of circumstances. They were found in oxygen-deficient films, and they were observed across artificially fabricated grain boundaries (GB). In the latter case, it is basically a tunneling phenomenon. In particular Klein *et al.* showed that a series of such GB's could lead to an $R(T)$ with two peaks [8]. Moreover, they were able to fit their IV curves to a model suggested by Glazman and Matveev, in which the current is carried by a multistep tunneling process

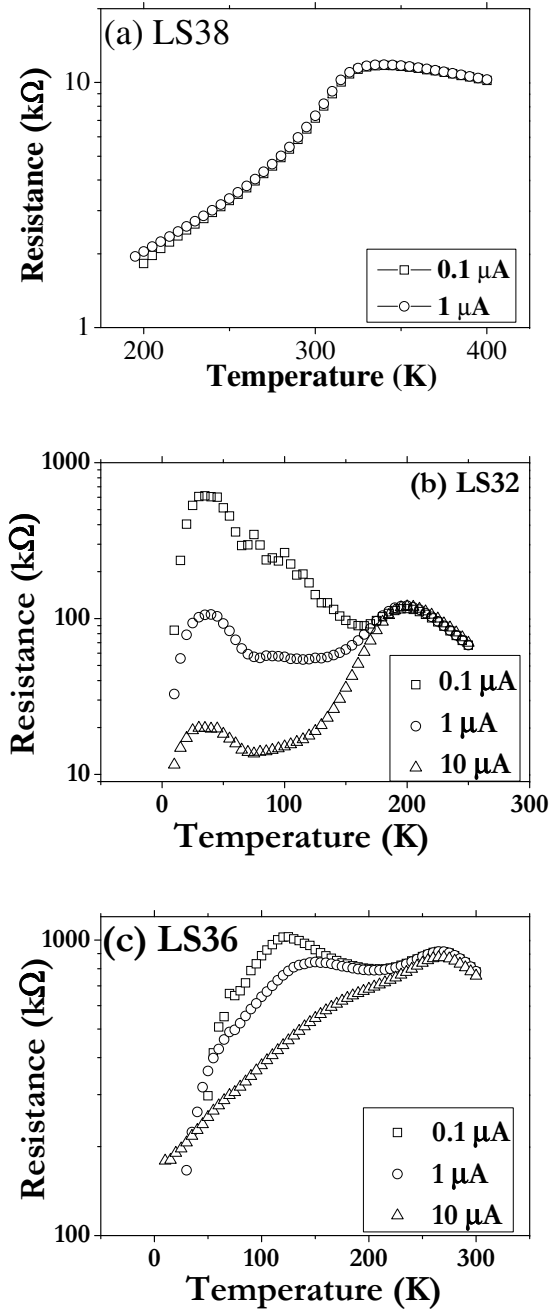


Figure 5.10: Temperature dependence of resistance for 300 nm wide bridge of LSMO films under different dc currents (a) a 42 nm film (LS38) (b) a 17 nm film (LS32) (c) a 10 nm film (LS36).

Sample ID	d_{LSMO} (nm)	J (A/m ²) (1 μ m, 1 μ A)	J (A/m ²) (300 nm, 10 μ A)
LS38	42	2.4×10^7	8×10^8
LS32	17	5.9×10^7	2×10^9
LS36	10	1×10^8	3×10^9
LS41	6	1.7×10^8	6×10^9

Table 5.1: Current densities for thin films of LSMO calculated for 1 μ m and 300 nm wide bridges at currents of 1 μ A and 10 μ A respectively. Given are the sample ID, thickness of LSMO d_{LSMO} (nm), current density J (A/m²) for 1 μ m bridge and 300 nm wide bridges.

involving 1,2,3...n localized states. This leads to a voltage-dependent conductance $G(V) = G_o + G_1 + G_2 V^{4/3} + G_3 V^{5/2}$ with $I = G(V) V$. Note that for simple tunneling one would expect something like $G(V) = a + b V^2$. Figure 5.11 shows what the GB expression would look like for the data taken on the 10 nm film at 155 K, using the $G_o + G_1 + G_2$ terms. It is clear that the measured behavior is too shallow for a tunneling description. That leaves oxygen vacancies, as a possible candidate. This case was studied by Liu *et al.* on thin films of $La_{0.7}Ca_{0.3}MnO_3$, which were annealed to different degrees in order to remove oxygen [22]. They basically found a spike-like voltage dependent conductance, similar to the behavior shown in Figure 5.8b, for slightly oxygen deficient material; or more parabolic behavior, reminiscent of tunneling, for the highly oxygen deficient films. Our case of the 300 nm bridges resembles the slight oxygen deficiency, and this is also the case for the behavior in a magnetic field, where the nonlinear behavior disappears. The data therefore suggest that the 300 nm bridges are significantly more oxygen-deficient than the 1 μ m bridges. This could well be the result of the lithographic structuring process. If that leads to a depleted zone with an extension of half the bridge width, the 1 μ m bridges would not be affected. That leaves the question why the resistance decreases so strongly with the increasing current or voltage. Following ref. [21] we would argue that oxygen loss leads to a decrease of the amount of Mn^{+4} , and therefore locally to lower T_c 's. The bridge then is a mixture of material with different T_c 's, and the nonlinearities disappear when all regions have become metallic, around 50 K. Using the results of Dörr *et al.* [21], this suggests that the Mn^{+4} concentration has decreased to 0.2, corresponding to an oxygen loss $\delta = 0.05$ in the formula $La_{0.7}Sr_{0.3}MnO_{3-\delta}$.

The data also indicate, however, that the current can drive the mixed regions metallic. A possible mechanism here is that carriers are released which were initially trapped by the disorder. An oxygen defect produces extra Mn^{+3} ions with the tendency of a local Jahn - Teller deformation as well as antiferromagnetic correlations. The current is supposed to be spin polarized, and it has been conjectured that spin torque effects could flip the spin of Mn^{+3} ion and free that charge. In homogeneous manganite systems this would mean that a current could enhance T_c , which has never been observed. This need not be surprising, since the current densities for generating spin torque effects are very high. In typical experiments

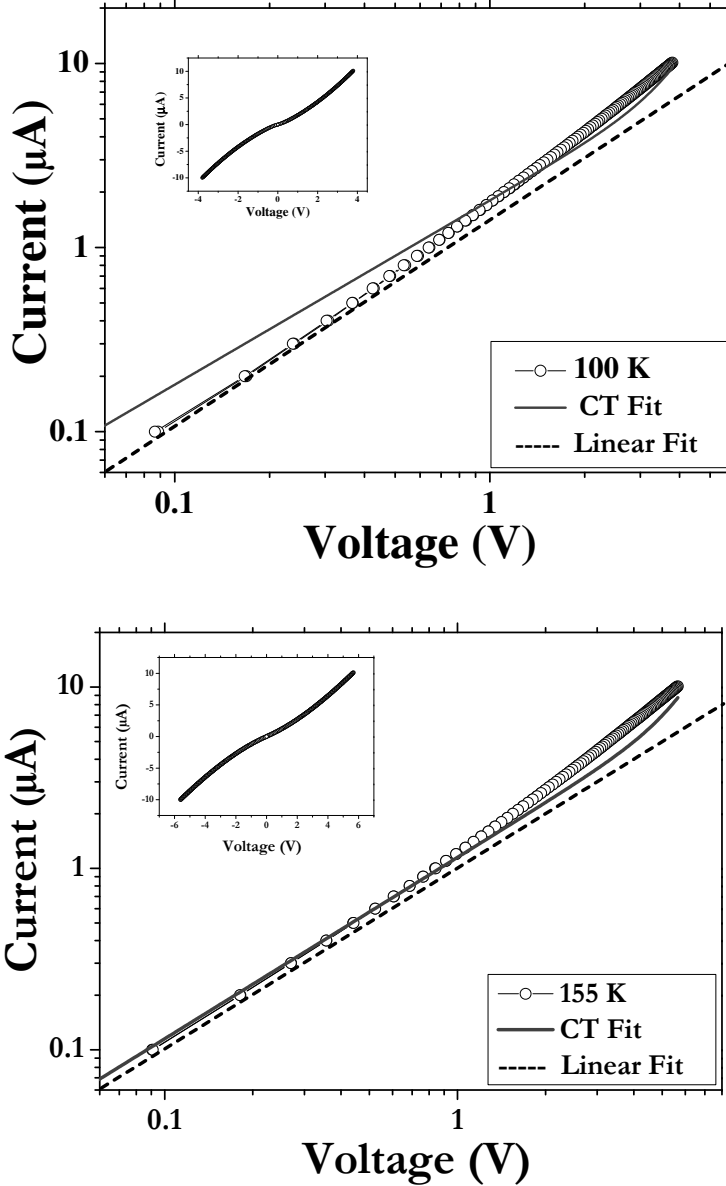


Figure 5.11: (a) Current-voltage curves for a 10 nm LSMO on STO at (a) 100 K (b) 155 K. The curves are plotted on a double logarithmic scale, the dark grey line represents the least square fit to the CT (conductance tunneling) fit, $I = G(V) V$ where $G(V) = G_o + G_1 + G_2 V^{4/3} + G_3 V^{5/2}$ and the black dashed line is the linear fit, the insets show the IV curves on linear scale.

involving magnetic nanopillars, the values are of the order of 10^{11} A/m² [24]. In our case, however, the system is manifestly inhomogeneous, which means filamentary current distribution, and the current densities are very large. Table 5.1 shows that, when the full bridge area is taken into account, the current density at 10 μ A is 3×10^9 A/m². This is a conservative estimate, since we know from the experiments described in chapter 4 that a dead layer is likely to occur and the 10 nm layer is probably rather a 5 nm layer, so that the order of magnitude is at least 10^{10} A/m².

A final point to address is the behavior of the 42 nm film, which behaves quite like the bulk material. Apparently, oxygen depletion is not as strong for the thinner film as it is for the thicker one. The reason for this is not yet clear.

5.5 Conclusion

We conclude that thin films of LSMO lose some oxygen locally in 300 nm wide bridges which results in highly nonlinear behavior in IV curves at intermediate temperatures. The effect is only seen in thin films less than 18 nm. The effect appears to be due to inhomogeneities in the oxygen distribution, and is therefore different from the effects found in LCMO bridges, where a homogeneous glassy state was posed to occur. The present study gives an opportunity to explore the additional effects in physical properties of manganites on microscopic scales.

Bibliography

- [1] J. Aarts, S. Freisem, R. Hendriks, and H.W. Zandbergen, *Appl. Phys. Lett.* **72**, 2975 (1998).
- [2] Y. Konishi, Z. Fang, M. Izumi, T.Mamako, M. Kasai, H. Kuwahara, M. Kawasaki, K. Terakura and Y. Tokura, *J. Phys. Soc. Jpn.* **68**, 3790 (1999).
- [3] Z. Fang, I.V. Solovyeu, and K. Terakura, *Phys. Rev. Lett.* **84**, 3169 (2000).
- [4] M. Bibes, Ll. Balcells, S. Valencia, J. Fontcuberta, M. Wojcik, E. Jedryka, and S. Nadolski, *Phys. Rev. Lett.* **87**, 067210 (2001).
- [5] Z.Q. Yang, R. Hendriks, J. Aarts, Y.L. Qin, and H.W. Zandbergen, *Phys. Rev. B* **70**, 174111 (2004).
- [6] M. Huijben, L.W. Martin, Y.-H. Chu, M.B. Holcomb, P. Yu, G. Rijnders, D.H.A. Blank, and R. Ramesh, *Phys. Rev. B* **78**, 094413 (2008).
- [7] A. Gupta, G.Q. Gong, G. Xiao, P.R. Duncombe, P. Lecoeur, P. Trouilloud, Y.Y. Wang, V.P. Dravid, J.Z. Sun, *Phys. Rev. B* **54**, R15629 (1996).
- [8] J. Klein, C. Hofener, S. Uhlenbruck, L. Alff, B. Buchner, and G. Gross, *Euro. Phys. Lett.* **47**, 371 (1999).
- [9] A.M.H. Gosnet, J. Wolfman, B. Mercey, C. Simon, P. Leocour, M. Korzenski, M. Hervieu, R. Desfeux, G. Baldinozzi, *J. Appl. Phys.* **88**, 4257 (2000).
- [10] Y. Fu, *Appl. Phys. Lett.* **77**, 118 (2000).
- [11] A.D. Andres, J. Rubio, G. Castro, S. Taboada, J.L. Martinez, J.M. Colino, *J. Appl. Phys.* **83**, 713 (2003).

- [12] B. Ghosh, S. Kar, L.K. Brar, A.K. Raychaudhuri, J. Appl Phys. **98**, 094302 (2005).
- [13] C. Beekman, J. Zaanen, and J. Aarts, Phys. Rev. B **83**, 235128 (2011).
- [14] V. Markovich, E.S. Vlahov, Y. Yuzhelevskii, B. Blagoev, K.A. Nenkov, and G. Gorodetsky, Phys. Rev. Lett. **72**, 134414 (2005).
- [15] Y. Tokura, Colossal Magnetoresistive Oxides, Vol. **2**, Gordon & Breach Science publishers, 2000.
- [16] J. Gao, S.Q. Shen, T.K. Li, and J.R. Sun, Appl. Phys. Lett. **82**, 4732 (2003).
- [17] C. Barone, C. Adamo, A. Galdi, P. Orgiani, A.Y. Petrov, O. Quarnta, L. Maritato, and S. Pagano, Phys. Rev. B **75**, 174431 (2007).
- [18] T. Wu, S.B. Ogale, J.E. Garrison, B. Nagaraj, A. Biswas, Z. Chen, R.L. Greene, R. Ramesh, T. Venkatesan, and A.J. Millis, Phys. Rev. Lett. **86**, 5998 (2001).
- [19] M. Fäth, S. Freisem, A.A. Menovsky, Y. Tomioka, J. Aarts, and J.A. Mydosh, Science **285**, 1540 (1999).
- [20] L. Bery, Phys. Rev. B **75**, 104423 (2007).
- [21] K. Dörr, J.M. De. Teresa, K-H. Müller, D. Eckert, T. Walter, E. Vlahov, K. Nenkov, and L. Schultz, J. Phys. Condens. Matter **12**, 7099 (2000).
- [22] S.J. Liu, J.Y. Juang, J.-Y. Lin, K.H. Wu, T.M. Uen, and Y.S. Gou, J. Appl. Phys. **103**, 023917 (2008).
- [23] L.I. Glazman, and K.A. Matveev, Sov. Phys. JETP **67**, 1276 (1988).
- [24] J.A. Katine, F.J. Albert, R.A. Buhrman, E.B. Myers and D.C. Ralph, Phys. Rev. Lett. **84**, 8149 (2000).

Interfaces of $\text{LaAlO}_3/\text{SrTiO}_3$ made by sputter deposition

6.1 Introduction

We have discussed the properties of the two dimensional electron gas at the interface between the band insulators LaAlO_3 (LAO) and SrTiO_3 (STO), and the mechanisms behind its formation in chapter 2. Ohtomo & Hwang were the pioneers to introduce such conducting interfaces in 2004 [1], which they ascribed to an intrinsic doping mechanism driven by the broken symmetry at the interface. In LAO, alternating layers of LaO and AlO_2 are positively (negatively) charged, while the SrO and TiO_2 layers in SrTiO_3 are neutral. This mechanism of electronic reconstruction is important, as can be seen in the fact that a minimum LAO layer thickness of 4 unit cells is needed to create the conducting interface, and that the STO surface needs to be terminated with a TiO_2 layer, furnishing Ti 3d orbitals at the interface. It is not the only possible mechanism however, and surprisingly, there is still considerable debate about the relative importance of the different factors which conspire to produce a conducting interface [2].

In particular important is the question of oxygen deficiencies, as can be appreciated from the fact that the properties of the LAO/STO interface crucially depend on the pressure of the background oxygen, at least when grown by Pulsed Laser Deposition (PLD) [3–5]. In general, the conductivity decreases with increasing oxygen pressure, and it was recently reported that at a pressure of 5×10^{-2} mbar, which is close to the upper limit for the PLD process, the interface became insulating [6]. On the other hand, Cancellieri et al showed that interfaces grown at 10^{-2} mbar could be made superconducting when subjected to a postanneal treatment [7]. Clearly, the mobility of oxygen through the different layers during and after growth is a relevant parameter. Also cation intermixing at the interface was shown to play a role [8–10], and in a recent study on samples grown by Molecular Beam Epitaxy it was found that the La to Al ratio of the LAO layer needs to be

smaller than 1 in order to activate the interface conductance [11]. This issue has not yet been addressed at all in PLD grown interfaces.

The overwhelming majority of studies of the LAO/STO interface has been performed on PLD-grown samples. Given the promise for applications in oxide electronics [2, 12], the question is valid whether interfaces with similar (conducting) properties can be prepared by sputter deposition, a question which to our knowledge has not yet been addressed.

Sputter deposition of oxides takes place at high oxygen pressures (typically 1 mbar), which again raises the issue of the behavior of oxygen atoms and vacancies. In this chapter, we report such experiments. The interfaces between LaAlO_3 and the TiO_2 -terminated surface of SrTiO_3 substrate are grown by RF sputtering in an oxygen atmosphere as described in section 6.2. In our deposition system, the optimized growth pressure and growth temperature for the best film and interface quality are 0.8 mbar and 920°C . The surface of the LAO films is characterized by AFM and XPS, thickness and lattice constants of films are measured using x-rays, details are given in section 6.2. As shown in section 6.3, we do not observe conductance, nor can we render the interface conducting after postannealing. In section 6.4, interfaces of films are studied by TEM and EELS. Moreover, in TEM/EDX measurements, we find that the La/Al ratio in the LaAlO_3 film is 1.07. It appears that this ratio is connected to the high pressure, and is also material in allowing oxygen diffusion to and from the interface. The results are compared with the low pressure PLD grown samples and discussed in detail in section 6.5. It is found that these films, which do yield conducting interfaces, are Al-enriched.

In section 6.6, the magnetic properties of sputtered grown interfaces are discussed. It is found that sputtered grown non-conducting interfaces are also non-magnetic.

6.2 Sputter grown LAO/STO interfaces

Crystal growth being a non-equilibrium kinetic process is generally difficult to control in any type of deposition, since it depends on a large number of parameters such as temperature, process gas pressure, mismatch between substrate and film lattice parameters, energy of the deposited particles, surface mobility etc. In the case of growing complex oxides with reactive RF sputtering, the reaction between gas and emitted target particles is assisted by substrate heating to ensure the formation of the desired film structure and stoichiometry.

Basically, to grow stoichiometric thin films of LaAlO_3 , a stoichiometric LaAlO_3 target (La=1, Al=1) is chosen. All LAO films are grown on STO substrates, singly terminated by a TiO_2 surface. The singly terminated surfaces were commercially prepared by the company TSST B.V, Enschede, the Netherlands. For a given forward power and target-to-sample distance, two critical parameters which control the growth in sputtering are the deposition temperature T_{dp} and the pressure P_{dp} . We determined a window for (T_{dp}, P_{dp}) for smooth and epitaxial growth of LaAlO_3 on SrTiO_3 which proved to be rather narrow. The determination is mainly based on

P_{dp} (mbar)	T_{dp} ($^{\circ}C$)	Rough.(nm)	c_o (Å)	d_{LAO}	t_{dp} (Min.)	Sample ID
1.2	800	1.6	x	5	120	LA44
1.2	840	1.7	x	15	306	LA37
1.2	900	2.1	x	8	60	LA48
1.2	1034	0.2	3.786	13	120	LA47
1.0	840	1.4	3.789	13	160	LA38
0.8	840	2	3.789	13	120	LA36
0.8	920	0.2	3.786	20	120	LA51
0.8	920	0.4	3.777	12	90	LA69
0.8	940	0.2	3.766	12	90	LA72
0.6	940	0.8	3.799	14	100	LA68
0.4	940	0.2	x	15	60	LA67
0.28	840	22	x	x	30	LA9

Table 6.1: Sputter deposition parameters of LaAlO_3 on SrTiO_3 . Given are the sputter gas pressure P_{dp} , the substrate temperature T_{dp} , the roughness of the LAO film as measured by AFM, the out-of-plane lattice constant c_o , the LAO film thickness, growth time in t_{dp} (minutes) and the identifier of each sample. The forward power used to grow these films is 30 W.

AFM surface roughness. The out-of-plane lattice constant c_o was also monitored, although its significance is more complicated, since it can be influenced by the stoichiometry as will be discussed. It can be noted that the growth rate for the films grown at 1.2 mbar is quite low when compared to the films at 0.8 mbar.

Before giving some details, the main results are presented in Table 6.1, where the roughness and c_o values are given for film growth in a pressure range between 1.2 mbar and 0.28 mbar, and a temperature range between 800 $^{\circ}C$ and 940 $^{\circ}C$. Smooth and epitaxial films are grown around 920 $^{\circ}C$ -940 $^{\circ}C$ and 0.8 mbar. Growing outside this window results in rough and structurally defective films. More trends are visible in Table 6.1. At 1.2 mbar, smooth films can be grown, but that requires very high temperature. Films grown at 0.6 mbar are smooth, but they have larger lattice constants than bulk LAO, which indicates the films are not correctly strained. At 0.4 mbar, films are smooth but no peak of LAO film can be seen in diffraction experiments. The lowest growth pressure used to grow LAO films is 0.28 mbar. The surface is then very rough as we will see back sputtering impedes the growth of LAO film.

Thin films of LAO were grown in a wide thickness range from 2 nm to 51 nm although for the optimized growth parameters (920 $^{\circ}C$ and 0.8 mbar), the range is between 2.5 nm and 30 nm. After deposition, films were cooled down in vacuum. It takes about 5 hours to cool down to room temperature. Some films were cooled down in the growth pressure of 0.8 mbar, but no significant change in morphology, lattice constant, XPS elemental spectra and conductivity was observed. The distance between target and substrate was about 4 cm which gives a growth rate of 0.16 nm/min for optimized $P_{dp} = 0.8$ mbar, $T_{dp} = 920^{\circ}C$, $P = 30$ W. With this

Power (W)	Rough.(nm)	c_o (Å)	d_{LAO} (nm)	R_{dp} (nm/min)	Sample ID
30	0.1	3.786	21	0.16	LA53
40	0.2	3.788	32	0.27	LA54
50	0.4	3.773	35	0.3	LA55
60	0.4	3.799	51	0.43	LA56
70	0.2	3.808	x	x	LA57
80	0.2	3.817	x	x	LA58
90	0.3	3.813	x	x	LA59

Table 6.2: Effect of forward power on LAO films grown at $T_{dp} = 920^\circ\text{C}$ and $P_{dp} = 0.8$ mbar. Given are the forward (FW) power, the roughness of the LAO film, the out-of-plane lattice constant c_o , the LAO film thickness, rate of deposition R_{dp} and relative identity (ID) for each sample.

pressure and temperature, decreasing target to substrate distance to 2 cm increased the growth rate but no change on quality of thin films.

We also investigated the effects of changing the forward power for growth in the window ($T_{dp} = 920^\circ\text{C}$ and $P_{dp} = 0.8$ mbar). As can be seen in the Table 6.2, increasing forward power from 30 W first increases the roughness, while above 60 W the value of c_o started to increase. Apparently, both a lower sputter gas pressure and high RF power leads to more energy being deposited during growth, and a loss of strain, e.g., epitaxy. In the next two paragraphs we give more details on the AFM and XRD results.

6.2.1 Surface characterization by AFM

We discussed in the previous section that the sputtering allows a small temperature and pressure window to work in. We have grown a large number of films to find out the right growth parameters. The first step is to check the quality of film using atomic force microscopy (AFM). AFM software was used for the image rendering, data smoothing, height profiles and roughness analysis using a standard area of $1\mu\text{m}$, mostly shown for images in this section and in Table 6.1.

Figure 6.1 shows the results of some films grown at 2 mbar of oxygen at different temperatures. The growth time is 15 minutes for all. The change in temperature has a clear effect on the morphology. The film grown at 800°C shows grains and the roughness is high (1.6 nm). The film grown at 840°C has decorated steps. The film is very smooth (0.3 nm). The film grown at 870°C is rough again (1.7 nm) and shows some outgrowths along with irregular terraces.

We observe that LA3 grown at 840°C looks better in morphology than the other two films. The next step is to reduce the pressure but keep the temperature at 840°C . The resulting films with the corresponding morphological changes are shown in Figure 6.2. The film at 0.8 mbar shows nicely spaced steps while the film 0.28 mbar has larger grains forming like clusters and is very rough (35 nm). Smooth films (0.3 nm) are grown at 0.8 mbar and 920°C . Figure 6.3 shows the

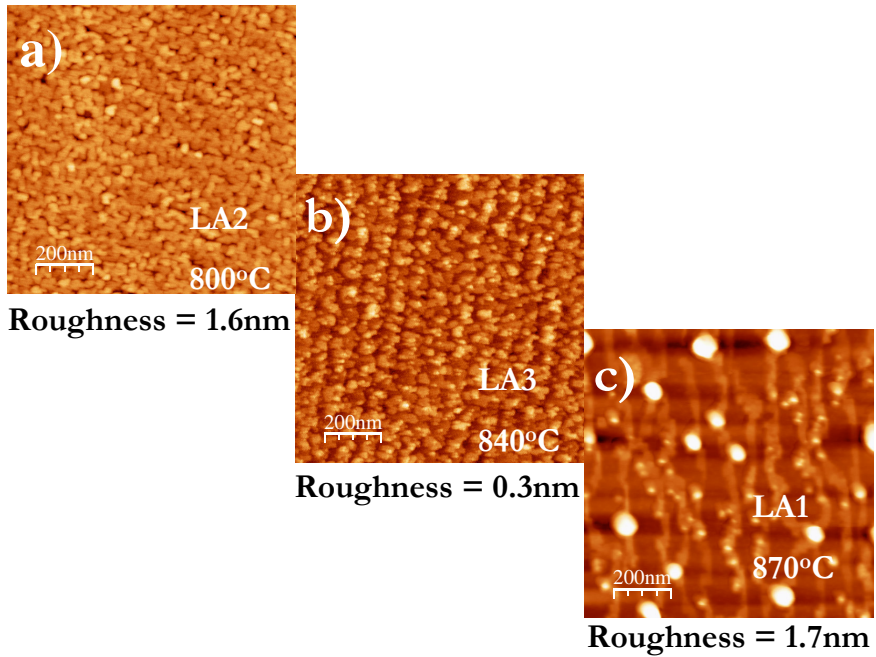


Figure 6.1: Surface morphology of LAO film grown at 2 mbar of oxygen pressure for 15 minutes. (a) LA2 grown at 800°C (b) LA3 grown at 840°C (c) LA1 grown at 870°C.

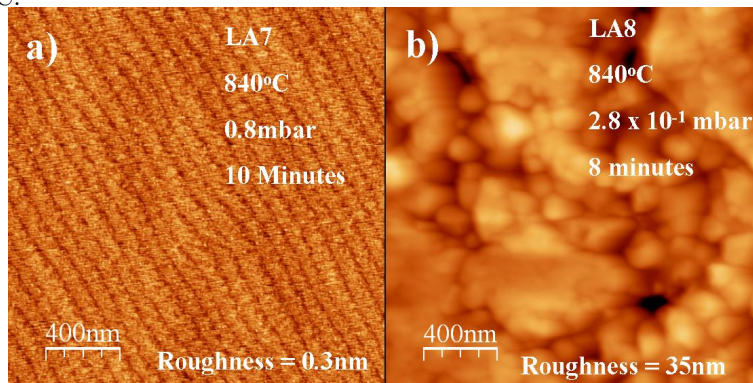


Figure 6.2: Surface morphology of LAO films grown at 840°C for approximately the same time at different growth pressures. (a) LA7 grown at 0.8 mbar of oxygen pressure (b) LA8 grown at 0.28 mbar of oxygen pressure.

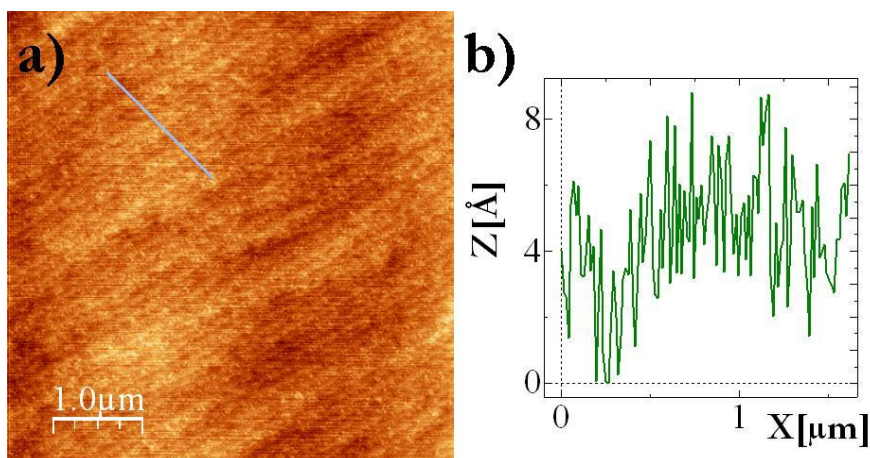


Figure 6.3: Surface morphology of a 20 nm thin film of LAO grown at 920°C , 0.8 mbar of oxygen pressure (a) topography (b) height profile of (a).

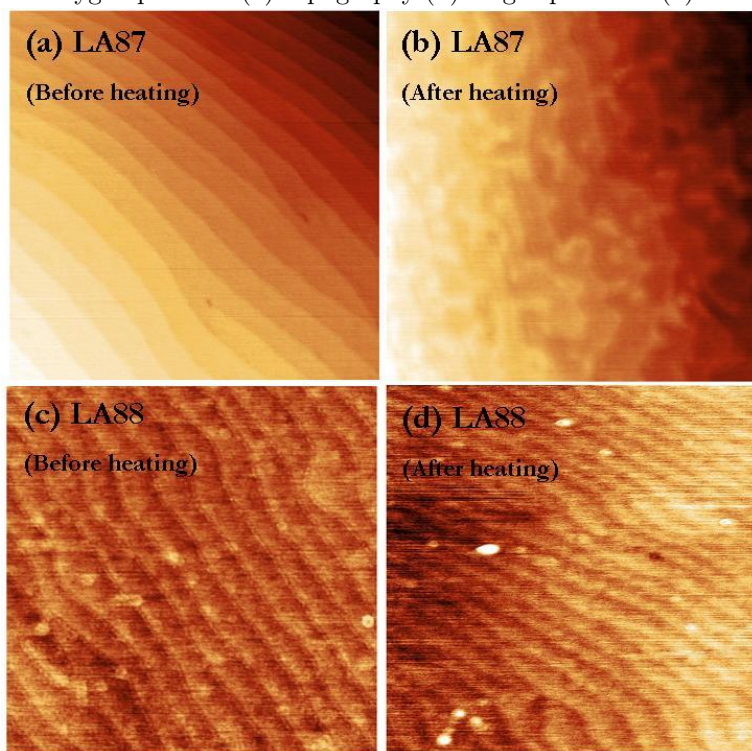


Figure 6.4: Surface morphology of a $\text{SrTiO}_3\text{-TiO}_2$ terminated surface before and after passing through the deposition steps without growing film (a & c). After heating to 920°C the substrate is (b) cooled down in vacuum (LAS7), (d) cooled down in 0.8 mbar of oxygen (LA88).

surface morphology of a 20 nm film (LA51). The corresponding profile (figure 6.3b) indicates roughness of 0.2 nm, probably connected to standard unit cell steps of 0.4 nm.

To see the effects of the high temperature growth and the cooling procedure on the TiO_2 -terminated surface of the STO substrate, some substrates were passed through all deposition steps without depositing a LaAlO_3 film. The surface morphology of the samples before and after heating is shown in Figure 6.4. The samples were heated up to 920°C at 0.8 mbar of oxygen pressure and remained at that temperature for 10 minutes and then cooled down to room temperature in two different ways. The sample shown in Figure 6.4a was cooled down in vacuum and the sample shown in figure 6.4c was cooled down in oxygen pressure of 0.8 mbar. There is no appreciable change in morphology measured by AFM before and after heating, although the terrace structure in the oxygen-cooled down sample is somewhat better preserved. Since this comes closer to the growth conditions (the vacuum can cause additional oxygen loss from the substrate), we conclude that the starting surface for growth is unchanged by the high temperature.

6.2.2 Characterization by XPS

In the early stage of finding the growth window, x-ray photoelectron spectroscopy was used. Figure 6.5 shows spectra of two LAO films grown at 2 mbar and 0.28 mbar of pressure at a temperature of 840°C . A wide range of binding energies is measured to obtain information about the element present at the surface. Figure 6.5a shows peaks of La and Al and also small peaks of Sr and Ti while in Figure 6.5b, almost only Sr is visible. This strongly suggests that at 0.28 mbar, back-sputtering is strong enough to prevent film deposition.

6.2.3 Thickness measurement of LaAlO_3 films by XRR

The measurement in this subsection and the next one was performed by Dr. Harkema at the University of Twente, the Netherlands.

Figure 6.6 shows an XRR measurement of a 20 nm thin film of LAO on STO grown at 0.8 mbar and 920°C (LA51). Thickness fringes are clearly visible which indicate a uniform film thickness. The measured data could be well fitted with a model consisting of a 20.33(9) nm thick LAO film of uniform density using Bruker XRD software. The film/air interface has a roughness of 0.21(3) nm; the roughness of the STO/LAO interface was found to be 0.6(2) nm. Both values for the roughness are indications for epitaxial interfaces, consistent with the AFM data shown in Figure 6.3. The roughness of the interface hints at the possibility of intermixing, which is often found in this system. We shall come back to the intermixing issue in section 6.4. The constant density for within the layer indicates homogeneous films over the whole thickness range as shown in Figure 6.6b.

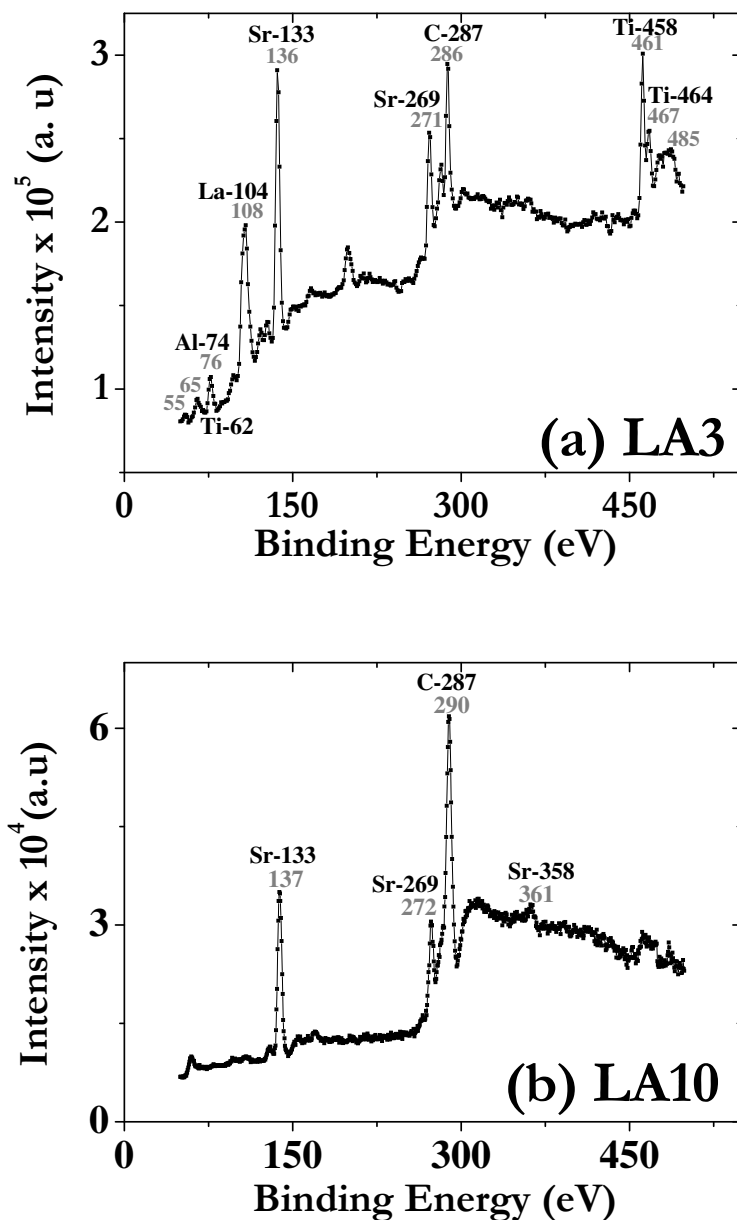


Figure 6.5: An X-ray photoelectron spectroscopy of two LAO films on STO. (Left) grown at 2 mbar and 840 °C, shows the peaks of La and Al with strong peak of Sr and small peaks of Ti, (Right) grown at 0.28 mbar and 840 °C shows diffusion of Sr at the surface of LAO film.

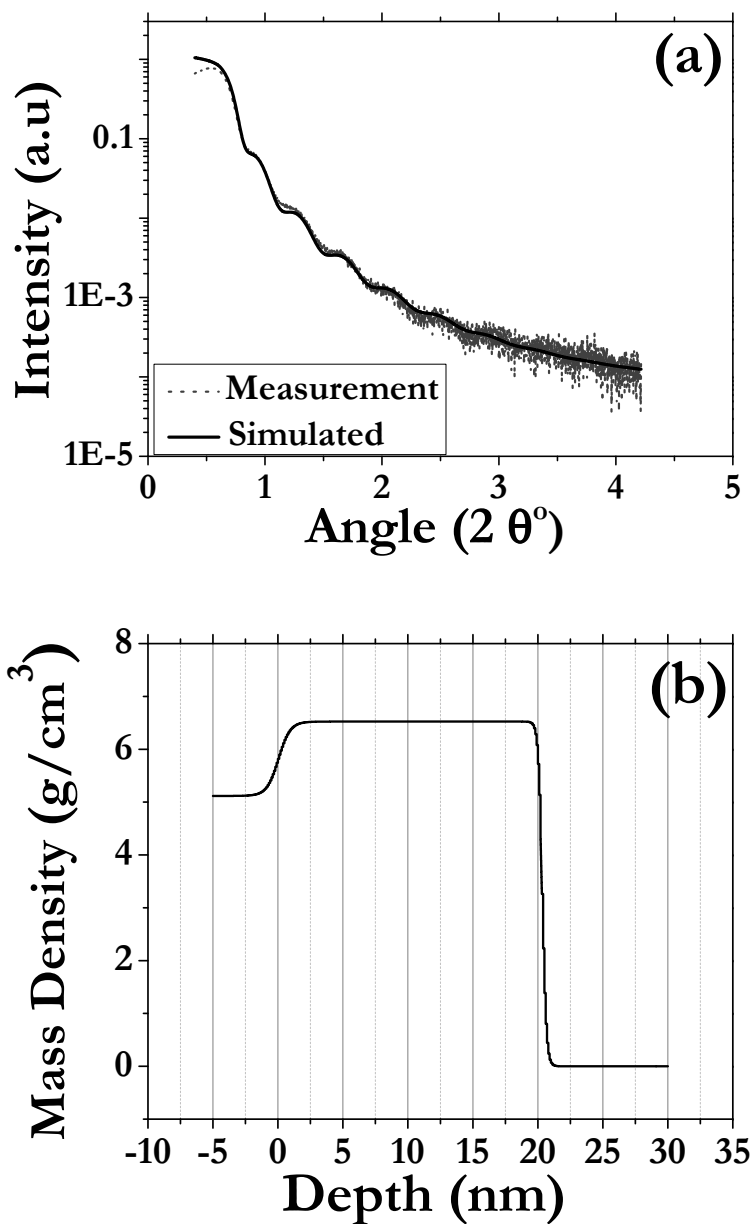


Figure 6.6: (a) An X-ray reflectivity curve for a 20 nm thick film (LA51). The period of oscillation determines the thickness of film, the drawn black line is a simulation. (b) A mass density analysis of the same 20 nm thick film to check the homogeneity of film in the whole depth range, The interface is at 0 depth.

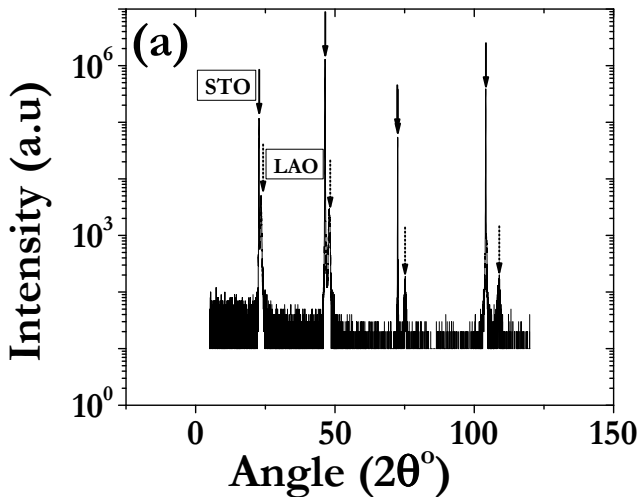


Figure 6.7: The diffraction data of a 20 nm thick film (LA51) showing 00l reflections of substrate and film. The solid arrows are for STO substrate and dotted arrows are for the LAO thin film.

6.2.4 Structure of LaAlO_3 thin films by XRD

The out-of-plane lattice constant c_o of the LAO films was measured by XRD. As an example showing the reflection the $\theta/2\theta$ scans of a 20 nm thick film of LAO is given Figure 6.7a.

Figure 6.8 shows three representative films with thicknesses 12 nm, 20 nm (LA51) and 51 nm. The values of c_o are given in Table 6.1. Comparison with the bulk lattice constant of LAO ($a_o = 3.789 \text{ \AA}$) shows that the 12 nm film is fully strained, and the 51 nm film has a lattice parameter even slightly larger than the bulk value. The 51 nm film was grown at 0.8 mbar, 920 °C, 60 W, so at larger forward power than the 12 nm and 20 nm films.

6.3 Interface Conductance

We determined the conductance of a number of films at room temperature. To approach the buried interface made by LAO/STO, wires were bonded for a 2-point or 4-point measurement, with contacts in line using a wire bonder. The typical distance between the voltage contacts was 1 mm. The samples were measured in a physical properties measuring system (PPMS) with external current and voltage sources. Typical values of the sheet resistance were 10 $M\Omega$ and above, limited by the voltage and current sources. Four films (with thickness of 12 nm, 13 nm, 14 nm and 30 nm) were cooled down to 10 K, but showed no variation in conductance

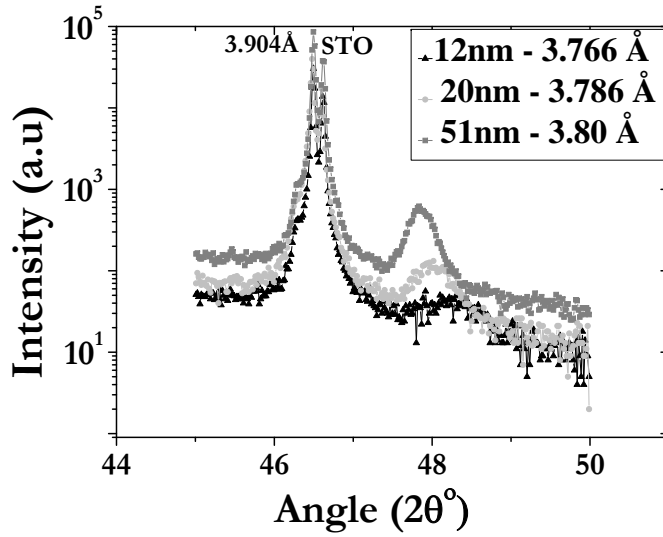


Figure 6.8: XRD data of three representative films of LAO at angles around the [002] reflection. The [002] STO peak corresponds to a lattice parameter of 3.904 Å. The square symbols show a 51 nm thick LAO film (LA56), the circles are for a 20 nm film (LA051), the triangles are for a 12 nm film (LA72). Also given are the lattice parameters of the films as calculated from the intensity peaks.

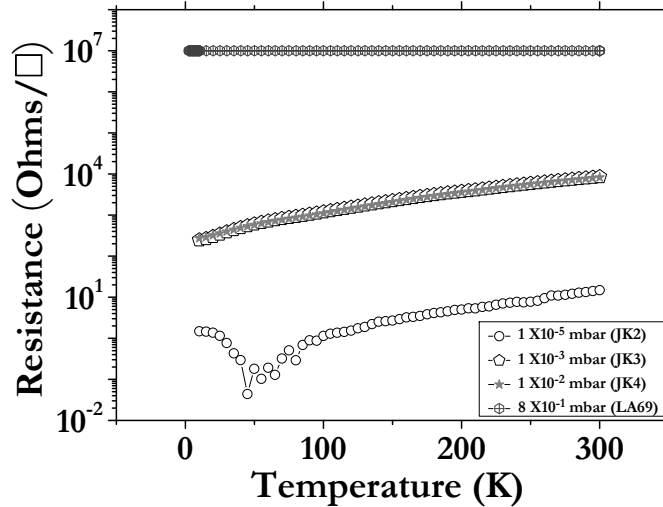


Figure 6.9: The resistance versus temperature behavior of interfaces grown by PLD at pressures of 10^{-5} mbar (JK2), 10^{-3} mbar (JK3), 10^{-2} mbar (JK4) respectively for a 5 nm LaAlO_3 film and by sputtering at 0.8 mbar of pressure for a 12 nm thin film of LAO (LA69).

(Figure 6.9). Post-annealing did not change this behavior. The details of post annealing are given in the next paragraph. To test the measurement setup, we obtained a series of films from the University of Twente (courtesy Dr. J. Kleibeuker). We measured the conductivity of PLD grown interfaces of $\text{LaAlO}_3/\text{SrTiO}_3$ grown at different pressures using Van der Pauw geometry. The conductivity of these samples (denoted by JK2, JK3, JK4) is shown in Figure 6.9.

Post-annealing

Insulating interfaces grown by PLD at 10^{-2} mbar can be made conductive by post annealing [7]. Therefore, rather than using the standard procedure of cooling, some samples were cooled down to 580°C . The oxygen pressure was then raised to 0.2 bar while the sample cooled further to 530°C in about 15 minutes. These conditions were maintained for 1 hour before cooling down to room temperature. Such samples still did not show conductance.

6.4 The LAO/STO Interface

To probe the interface between LAO/STO, transmission electron microscopy (HR-TEM), energy dispersive x-ray (TEM/EDX) and electron energy loss spectroscopy (EELS) were used in a collaboration with the group of Prof. H. Zandbergen at Delft University of Technology.

6.4.1 Quality of interface

The insulating interfaces made by sputtering need to be investigated in detail in particular to find out whether the quality is sufficient to make conductance over the macroscopic lengths possible. For this purpose, we used transmission electron microscopy which uses a high energy electron beam transmitted through a very thin sample to image and analyze the microstructure with atomic-scale resolution.

As we discussed earlier, sputtering allows a small window for crystalline films. Here we show interfaces of a few samples grown at different temperature and pressure. Figure 6.10 shows the TEM image of two films of LAO on STO, LA37 and LA47 which were grown at $P_{dp} = 1.2$ mbar and $T_{dp} = 840^\circ\text{C}$ and 1034°C respectively (see Table 6.1). Small and discontinuous patches can be seen for LA37 shown in Figure 6.10a. Figure 6.10b (LA47) looks more smooth but there are small etch pits. In these cases, it cannot be ruled out that the insulating behavior of films may be because of these discontinuities.

Figure 6.11 shows two more interfaces measured by TEM. Both films are on larger area of interface 10 nm and both show small discontinuities. Both films LA46 (1.2 mbar, 900°C , 40 W) and LA50 (1.2 mbar, 900°C , 30 W) show that the interface is rough and not continuous. There are small etch pits of around 10 nm high. Another two images of LAO thin films shown in Figure 6.12 also shows discontinuities and etch pits.

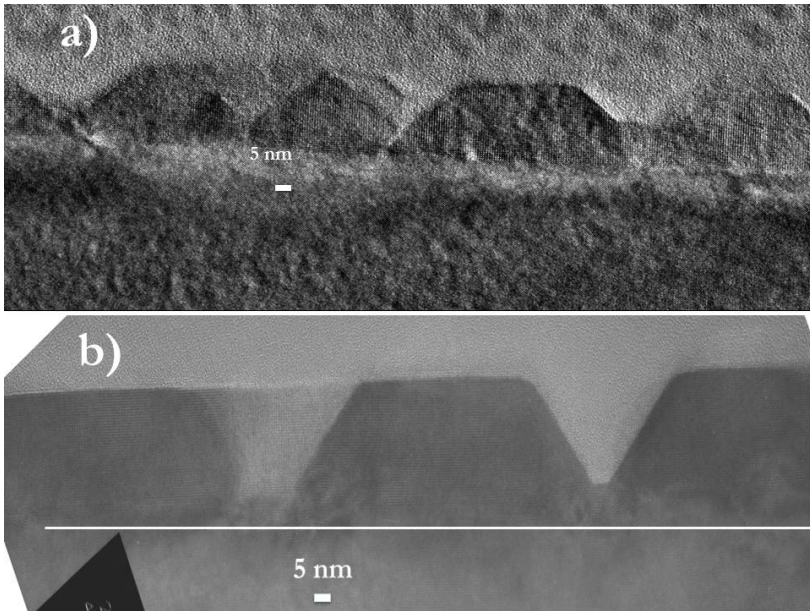


Figure 6.10: TEM analysis of two films of LAO/STO (a) LA37 (840°C, 1.2 mbar) (b) LA47 (1034°C, 1.2 mbar).

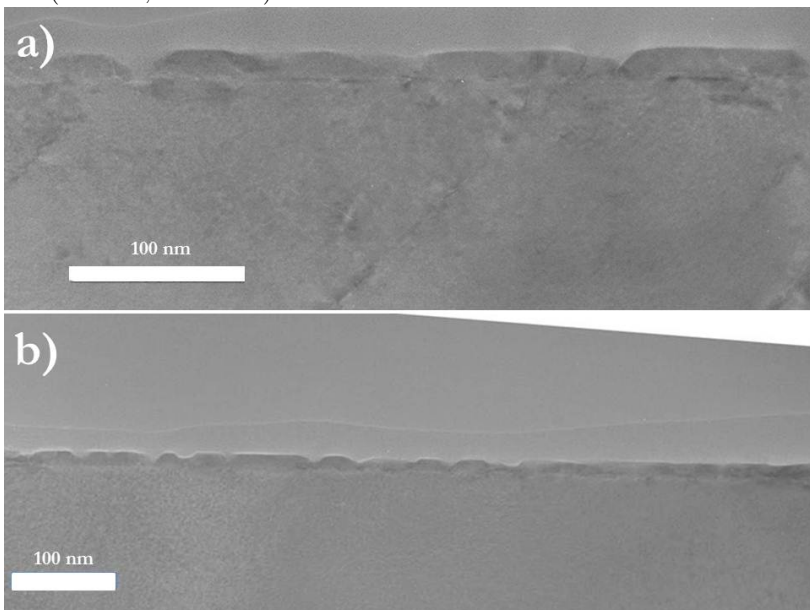


Figure 6.11: TEM analysis of two films of LAO/STO (a) LA46 (900°C, 1.2 mbar, 40 W) (b) LA50 (840°C, 1.2 mbar, 40 W).

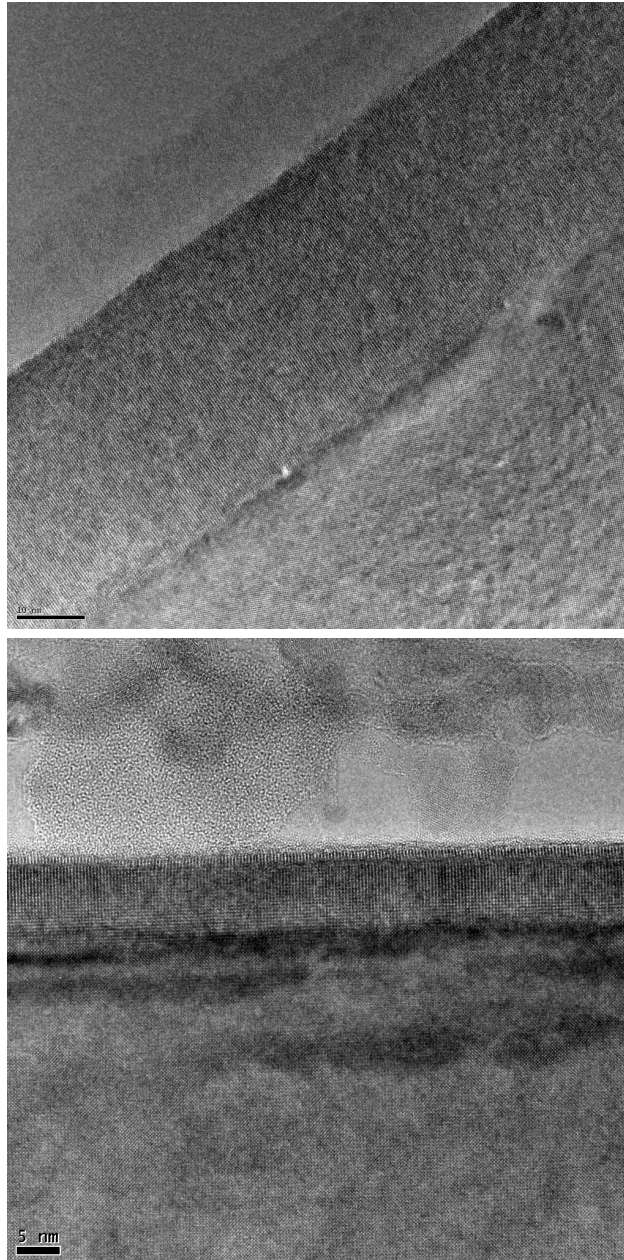


Figure 6.12: (Top) High resolution TEM picture of the LAO/STO interface for film LA55 (920°C, 0.8 mbar, 50 W). (Bottom) LA65 (940°C, 0.6 mbar, 30 W)

Figure 6.13a shows a TEM micrograph of an atomically sharp LAO/STO interface, made on film LA51. The diffractogram (figure 6.13b) shows a small splitting in the higher order diffraction spots, which point to a small misalignment between the out-of-plane crystallographic axes of LAO and STO. Similar observations were made on PLD-grown interfaces [10].

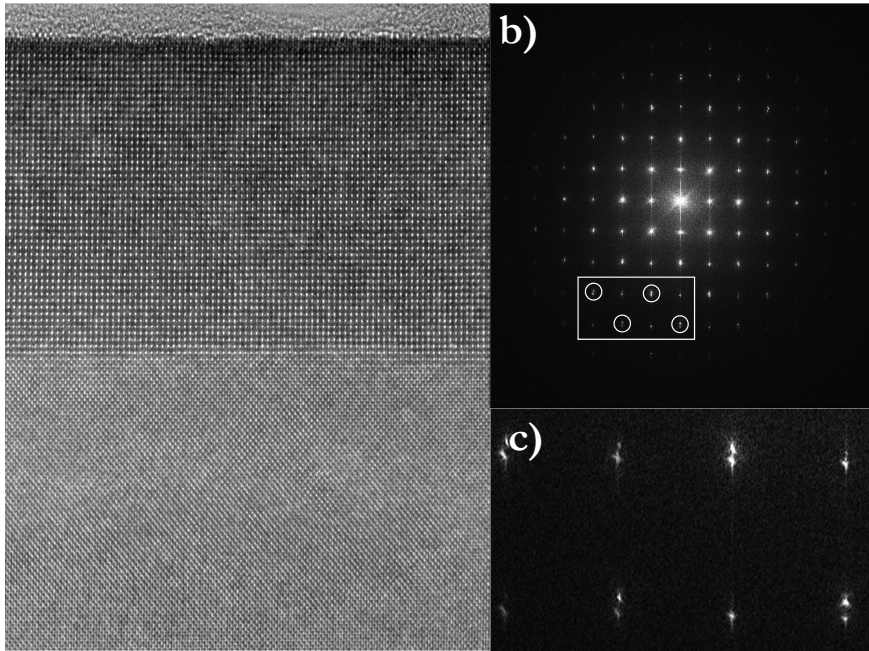


Figure 6.13: (a) High resolution TEM picture of the LAO/STO interface for film LA51.(b) Diffraction pattern. (c) Enlarged part of the region of the marked spots, showing a slight splitting which indicates some misalignment between film and substrate.

sharpness of interface

The sharpness and the amount of interface cationic mixing was investigated in the following way. Starting with the micrograph of Figure 6.14a, the original picture was subtracted from the same picture but shifted over half a unit cell along the $[110]$ -direction. Next, the intensity variation was derived for cross-sectional lines along a direction perpendicular to the interface. Two such lines are shown in Figure 6.14a (top), with the corresponding intensity variation in Figure 6.14b (bottom). On the LAO side of the interface, intensity still remains on the atomic positions, because of the difference in scattering factors for La and Al. On the STO

side of the interface, the Sr and Ti signals are very similar, and the subtraction brings the signal to close to zero. In this way, the crossover in the interface region gives a good estimate for the amount of intermixing, which can be seen to be of the order of two to three unit cells.

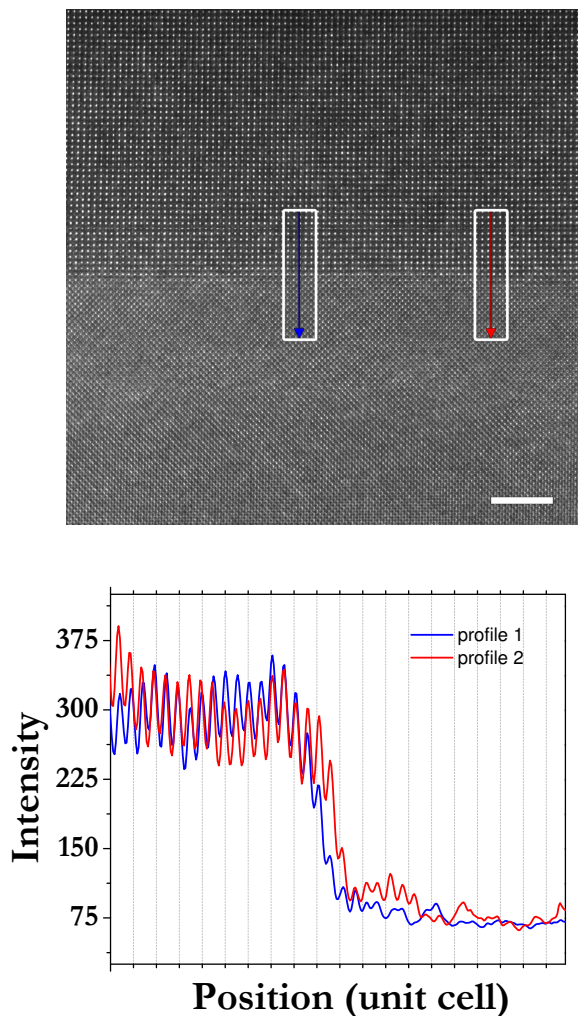


Figure 6.14: (Top) High resolution TEM picture of the LAO/STO interface for film LA51. (Bottom) Intensity variation along the two lines shown in the left figure, derived by subtracting the image from a copy of itself which was shifted by half a unit cell along the $[110]$ -direction (see text). Note that profile 1 (blue) is shifted over one unit cell with respect to profile 2 (red).

6.4.2 Stoichiometry of LAO film

The elemental ratio for each element was measured by energy dispersive x-ray analysis (EDX), in particular the ratio of La to Al. This was done as follows.

A diffracted spot is chosen, shown in dark black cross in Figure 6.15a. The beam is scanned through film/interface/substrate with reference to the dark black cross. The drift is checked continuously with respect to the diffracted spectrum. A single crystal of LaAlO_3 was used as a reference. The measurement done on it is shown in Figure 6.15. The ratio of La/Al for single crystal LAO is found to be 0.97. The

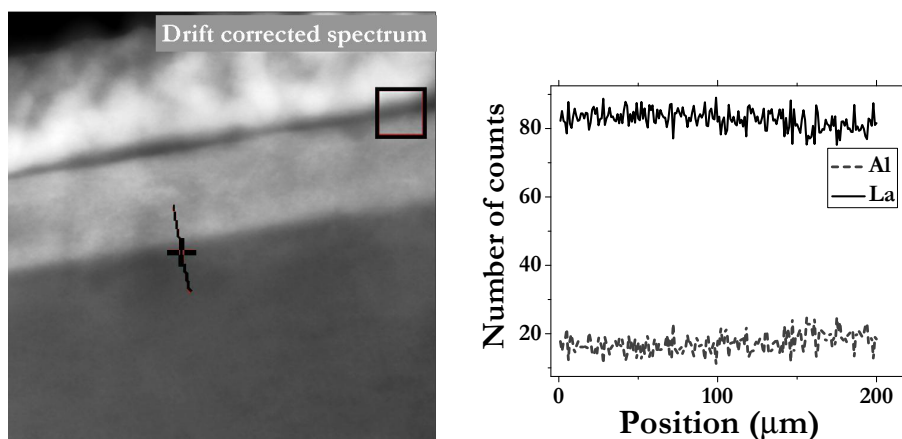


Figure 6.15: (Left) A drift corrected spectrum for precise measurement of TEM/EDX. (Right) Elemental profile of single crystal of LAO. The ratio La to Al is 0.97.

elemental variation across the LAO/STO interface was probed with EDX (beam diameter 0.2 nm) and is given in Figure 6.16. The signals are strong and stable beyond the interface region and allow to determine the elemental composition. EDX line scans were made across the LAO/STO interface, providing the atomic composition profiles as shown in Figure 6.16. The La/Al ratio of the film was obtained by averaging over 92 data points from Region 1 and calibrated by using the averaged value obtained from a LaAlO_3 crystal. For an accurate calibration, the EDX experimental conditions for the crystal and the film were deliberately set up in the same way, including the cross-section sample preparation, the orientation of the sample in the holder and the TEM mode settings. In this way, the La:Al ratio of the film was found to be 7 percent higher than that of the crystal. Supposing the ratio there to be 1, the La/Al ratio in the film is therefore 1.07(2).

6.4.3 Intermixing effects

To see intermixing effects at the interface, electron energy-loss spectroscopy (EELS) is used. EELS is a localized technique attached that measures the change in kinetic

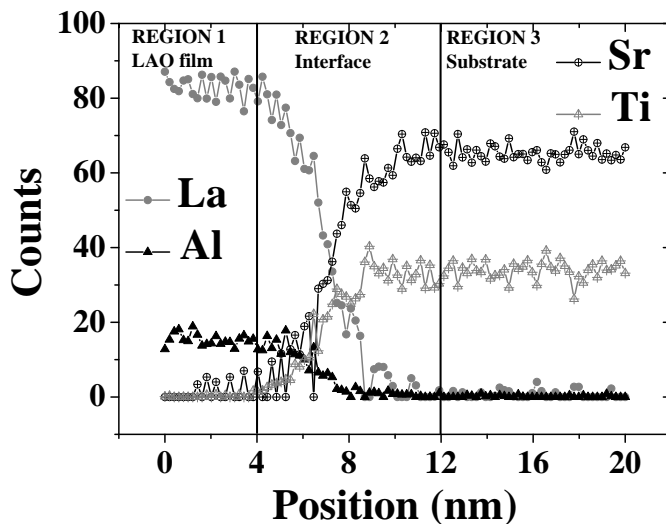


Figure 6.16: STEM/EDX elemental profile of the LAO/STO sandwich across the interface. The elemental ratios La/Al and Sr/Ti were determined in regions 1 and 3, respectively.

energy of electrons after they have interacted with a specimen. When carried out in a transmission electron microscope (TEM), EELS is capable of giving structural and chemical information about a solid down to the atomic level.

Figure 6.17 shows the EELS measurement performed on a 20 nm (LA51) thick film of LAO on STO. The TEM analysis of same film is shown in Figure 6.13. The number of counts corresponding to elements La and Ti are collected across the interface. It can be seen that La diffuses on the side of substrate while Ti diffuses on side of film which indicates that some unsharpness is found in both the change in Ti and La signal. The interface region is enlarged in part (b) of the figure. The width of the interface is 2 nm, comparable to the width in PLD grown interfaces.

6.4.4 Attempts to fabricate conducting interfaces

We have used oxygen as a reactive gas in RF sputtering to grow LAO films and LAO/STO interfaces which are found to be insulating. The high oxygen pressure possibly prevents the formation of oxygen defects and can compensate the deficiency of oxygen without need for pre/post annealing steps. It should be kept in mind that in PLD grown conducting interfaces, crystallinity is not an essential requirement. Amorphous films of LAO at 10^{-3} mbar can also make the interface conducting [24]. With this idea, we varied the growth parameters beyond the optimized growth window ($T_{dp} = 920^\circ\text{C}$ and $P_{dp} = 0.8$ mbar). We changed the oxygen

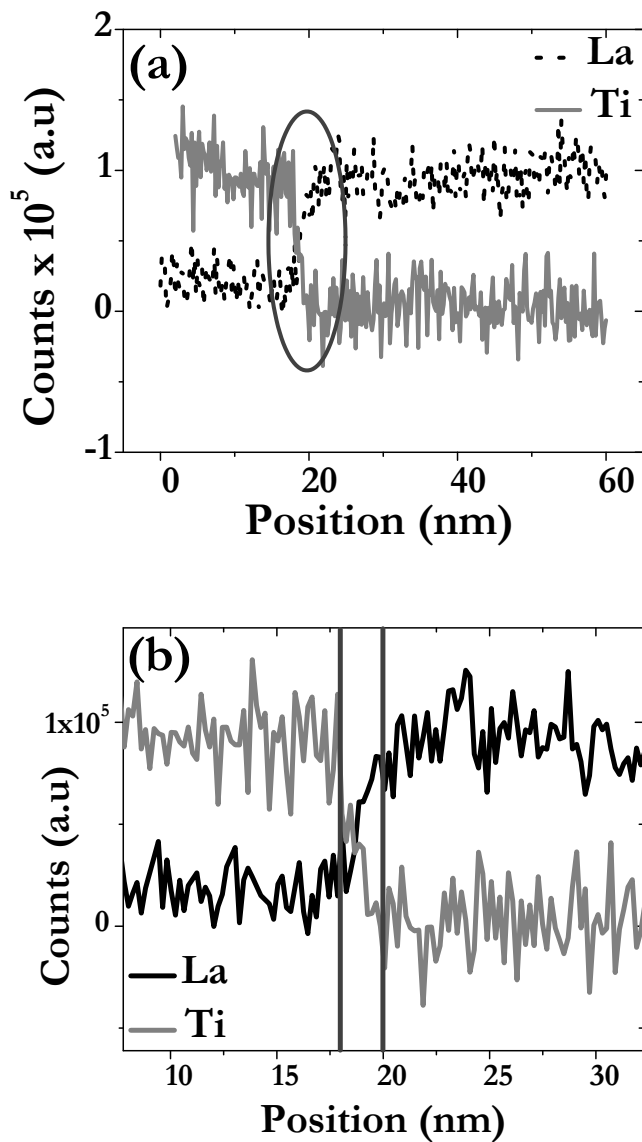


Figure 6.17: (a) EELS spectra showing the number of counts of intermixed La and Ti across the interface (b) the enlarged part at the interface showing the width of interface about 2 Å.

flow, introduced argon gas and even a mixture of argon and oxygen (50,50) but

interfaces were not conducting. Also reducing the pressure below the optimized pressure (Table 6.1) can produce amorphous films but the interface still remains non-conducting.

We also used a non-stoichiometric LaAlO_3 target ($\text{La}=0.94$, $\text{Al}=1.06$) to enhance the elemental contribution of Al in the grown films. There is no appreciable change in morphology, surface roughness by AFM, or lattice constant of these films. Their stoichiometry measured by TEM/EDX gives the ratio $\text{La}/\text{Al} = 1.06$ (LA78). So, it is not easily possible to enhance Al in growing films at high pressure oxygen environment, even with a defective target. We finally tried to put extra Al on the La-defective target in the form of pieces of Sapphire (Al_2O_3) to grow thin films of LAO for Al-enrichment. Clear changes can be seen in morphology but no change in the insulating state. Putting more Al resulted in roughening the surface and changing/increasing the lattice constant but conduction was not induced.

6.5 Discussion

The LAO films are grown at high oxygen pressure of 0.8 mbar and the interfaces are found to be insulating. The surface of the films is smooth, the structure is crystalline and the interfaces are sharp. The techniques which are used to characterize them confirm that sputtered grown interfaces are of high quality and can be compared to PLD or MBE grown interfaces. The picture from the data is then as follows.

Electronic reconstruction

Apparently, the sputter grown interfaces are not electrically reconstructed as in PLD. This leads us to argue that intrinsic electronic reconstruction is not the dominant mechanism. The presence of polar LAO and non-polar STO but the absence of conductance indicates a missing factor which either activates or initiates the interfacial conductance. Intermixing is not the cause since it is always there, either in PLD or sputtering. So, the polar discontinuity and intermixing do not seem to be the only or main factors determining the conductance.

Oxygen pressure

The sputtered interfaces grown at the high oxygen pressure of ~ 1 mbar closely resemble the high pressure PLD grown interfaces reported on by Kalabukhov [8] which are also insulating. This strongly hints at the important role of oxygen vacancies in conducting interfaces grown by PLD. Both in high-pressure PLD and in high-pressure sputtering, the amount of oxygen vacancies produced in the growth process becomes too low to generate a doped interface. This may not be simply due to the high gas pressure, which might be thought to quench vacancy production by highly energetic particles in the PLD- or sputter-plasma. Here, it should be remarked that the reduction of STO is difficult to rule out [6, 19]. If PLD growth parameters ($750^\circ\text{C} - 850^\circ\text{C}$, 10^{-5} to 10^{-3} mbar) can reduce STO even 10 nm or more (the interface is of the order of 2 nm), it can be enough to facilitate conduc-

tion at the interface. So, defects associated with the SrTiO₃ may be responsible for a conducting interface. In sputter grown films the high pressure of the background oxygen appears not to reduce the STO.

Growth temperature

The temperature of sputtered grown films is 920°C, which is higher than PLD grown films (typical temperature range 750°C - 850 °C). We would argue that the higher growth temperature is not the reason for the lack of conductance. There are two main reasons for that. First, STO substrates are annealed at high temperature (1300 °C) to produce the singly terminated TiO₂ surface. Second, TiO₂ terminated STO substrates were passed through the deposition steps without LAO films, cooled down in vacuum and growth pressure of 0.8 mbar and were checked by atomic force microscopy (AFM). This showed that no appreciable change in termination had occurred. Note that in PLD grown films the sheet resistance goes down with thickness [25], but that at 10 nm, there is still an appreciable dependence of the conductance, which we do not find in the sputter-grown films.

Strain, external electric field and post-annealing

The non-conductance of interfaces grown by sputtering does not change with strain. We have grown films on a large scale variation (Table 6.1) with respect to the out of plane lattice parameters of the LAO films but none of the samples has shown conductance. We also applied an electric field to these non-conducting interfaces to tune the interfacial conductance but found no change in insulating behavior. Post-annealing (the detailed process is discussed in section 6.3) also did not change the status of interfaces grown by sputtering. The results of Cancellieri *et al* [7] who converted initially non-conducting interfaces to conducting ones by post-annealing, strongly suggest that their LAO film allows the oxygen content of their interface to be varied. These three factors strain [26], electric field) [17] (in the underlying STO) and post-annealing [7] were able to induce or change the conductance of the interface grown by PLD but remained inactive for insulating interfaces grown by sputtering.

Stoichiometry

Next we come to the issue of stoichiometry, which until now has received relatively little attention. We start from the report mentioned in section 2.4.4, where it was demonstrated that the interface between STO and MBE-grown LAO was only conducting as long as the La/Al ratio was below 0.97. By inference, we assume for the moment that this means that the LAO film of a conducting PLD-grown STO/LAO interface also has a La/Al ratio below 0.97. As was shown in section 6.4.2, the sputtered samples have a ratio above 1, and this may have important consequences. For instance it was shown by Schneider *et al* that oxygen is drawn out of the STO substrate in the case of LAO films grown at low oxygen pressure (1.5×10^{-5} mbar), which were probably Al rich [14]. Such a mechanism to create oxygen defects may not be present in La-rich films, as was surmised by Chambers [15]. This is also of relevance for the post-annealed experiments of Cancellieri

P_{dp} (mbar)	Deposition process	La/Al ratio	Sample ID
8×10^{-1}	Sputtering	1.07	LA51
8×10^{-1}	Sputtering	1.066	LA78
1×10^{-5}	PLD	0.82	JK2
1×10^{-3}	PLD	0.856	JK3
1×10^{-2}	PLD	0.90	JK4
1×10^{-1}	PLD	1.03	JK8

Table 6.3: Summary of EDX measurement for sputter-grown and PLD grown samples. P_{dp} is the deposition pressure, corresponding La to Al ratio in PLD and sputtering and relative samples are also given.

et al, since their PLD-grown LAO is probably La deficient, allowing removal of oxygen [7].

In our case, the stoichiometry of sputter grown samples from a stoichiometric target measured by EDX gives La-rich films with a La to Al ratio of 1.07. The same ratio is obtained for a defective target of LaAlO_3 (La = 0.94, Al = 1.06). It shows that high pressure sputtering yields Al deficient films. This may not be strange as in sputtering lighter elements (here Al) can scatter more than heavier element (La). A recent study by Qiao *et al* gives an important correlation between La to Al ratio and lattice constants of LAO films on STO using PLD [13], which is shown in Figure 6.19. They find that the out-of-plane lattice constant increases by increasing the La/Al ratio but the in-plane lattice constant does not change and remains at 3.905 Å. When the La/Al ratio is 1.22, the in-plane lattice constant decreases and LAO films are no more tetragonal. A typical value of $c_o = 3.78$ Å for our thin strained films (Table 6.1) would correspond to a La/Al ratio of 1.10, in very good agreement with the value we find from EDX. The in-plane lattice constants of some of LAO films were measured using RSM plots in Twente University by Dr. S. Harkema. These preliminary measurements show that these films which were grown on optimized growth parameters (920°C, 0.8 mbar), have an in-plane lattice constant of 3.905 Å, and are therefore epitaxial and strained. It is interesting to note, however, that the 51 nm sample prepared with 60 W forward power (LA56) has a larger c_o than bulk. This might be possible if the La/Al ratio has increased further.

With respect to the consequences of ratio's La/Al larger or smaller than 1, this was investigated theoretically by Hellberg, using first-principle DFT calculations [16]. He concluded that in La-rich films, La does not substitute for Al but instead, Al vacancies are formed. These vacancies can migrate to the interface and screen the polar discontinuity, so that the metallic interface does not form.

Stoichiometry of PLD grown samples

A valid question which can be raised at this point is about the stoichiometry of conducting interfaces/films grown by pulsed laser deposition. We discussed in section 6.3 and 6.4 that films grown by sputtering and interfaces are of high quality.

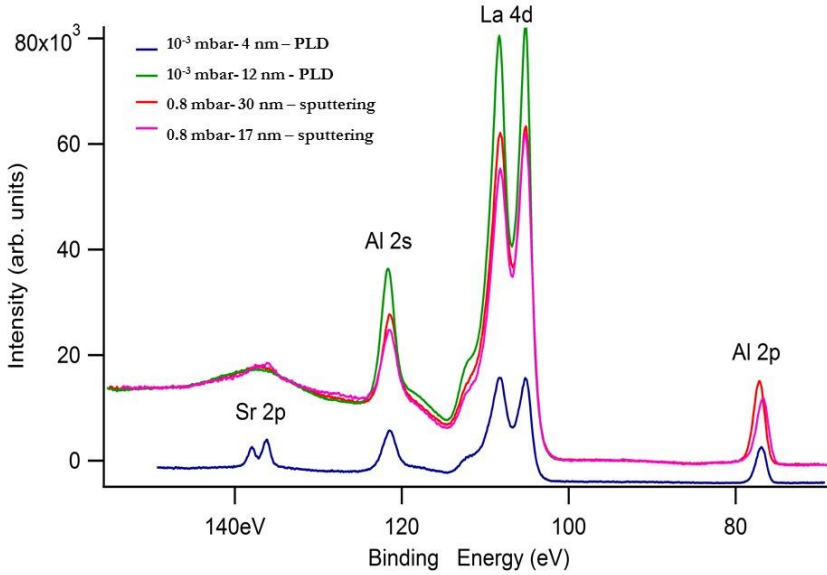


Figure 6.18: XPS spectra of PLD films grown at 10^{-3} mbar and sputter grown films at (0.8 mbar, 920°C - 940°C). The films shown in red line is cooled down in oxygen pressure of 0.8 mbar and in pink is cooled down in vacuum.

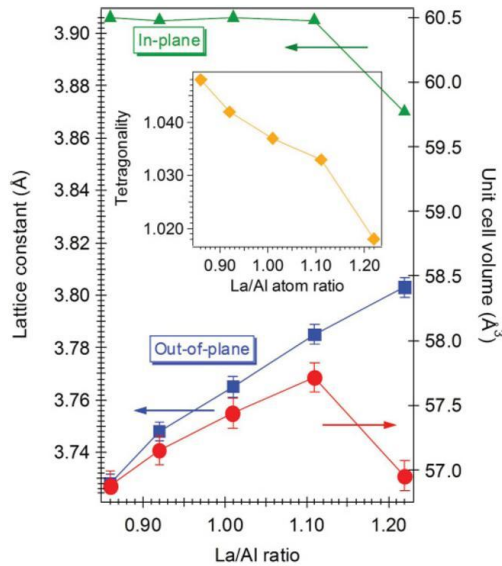


Figure 6.19: Dependence of lattice parameter and unit cell volume on La to Al atomic ratio from XRD data in PLD grown samples, the inset shows tetragonality of LAO films. The figure is taken from Ref. [13].

In Figure 6.18, we give XPS measurement of films grown by two types of deposition. The PLD samples were grown by Dr. J. Kleibeuker at Twente University, the Netherlands and she performed the XPS measurements. We can see a high intensity peak of La 4d and Al 2s, Al 2p for all samples. We also measured the ratio of La and Al in the samples grown by PLD at different growth pressures. The sample preparation for TEM/EDX measurement of all PLD grown samples is the same as discussed before in section 6.4 for sputter grown sample. The measurements show that conducting PLD samples grown at low pressure give a ratio around 0.85. The PLD grown films at the high pressure of 10^{-1} mbar gives the ratio of 1.03, close to sputter grown samples at 0.8 mbar (1.07). Clearly, this does not answer the question whether the La enrichment is a result of the high oxygen pressure, but it does help to understand why La-rich LaAlO_3 on SrTiO_3 does not yield conductance. Also, the La/Al ratio measured for PLD grown conducting interfaces confirm that the non-stoichiometry plays a vital role for conductance. Either Al rich films produce oxygen vacancy defects or oxygen vacancies allow the stoichiometric imbalance of the LAO films. The results of the EDX measurement are summarized in Table 6.3.

6.5.1 Conclusion

In conclusion, we have grown LAO/STO interfaces by sputtering in high oxygen pressure. The LAO films are smooth, strained for small thickness, and show excess of La, while the interfaces are not conducting; nor can they be rendered conducting by a post-anneal treatment. Apart from the practical implications with respect to sputtering as a technique to fabricate such conducting interfaces, the results point to the importance of the stoichiometry issue in relation to the physics.

6.6 Magnetic Properties of sputter grown interfaces

In the last section we showed that sputtered grown interfaces are not conducting. Here, we report the magnetic behavior of these interfaces. The magnetic properties were measured using a commercial superconducting quantum interface device (SQUID) magnetometer.

6.6.1 Introduction

Most of the focus in research on LAO/STO interfaces has been on their conducting properties. Recently, there has been renewed interest in the possible existence of magnetism at the interface of $\text{LaAlO}_3/\text{SrTiO}_3$. Interface magnetism was first theoretically suggested by Pentcheva and Pickett *et al.* for n-type interfaces of $\text{LaAlO}_3/\text{SrTiO}_3$ (both are non-magnetic materials) who found charge imbalance at the interface to be responsible for possible ferromagnetic order [27]. At about

the same time, experimental indications for interface magnetism were first reported [20].

There are different electronic configurations possible for the interface of $\text{LaAlO}_3/\text{SrTiO}_3$ which may lead to magnetism. It was found that at the interface, most of the carriers needed to compensate for the polar discontinuity go into localized states, which strongly suggests that it is these states that give rise to the magnetization [28]. The electronic phase separation is a theoretical prediction of transferred charges at the interface of LAO/STO which occupy nearly ten interface sub-bands [29]. Indications for such an EPS state is given by Ariando *et al.* [30]. Bert *et al.* found that the magnetic regions are inhomogeneous, with patches of micrometer-scale ferromagnetic regions and a total density of magnetic moments which is approximately equal to the density of electrons implied by the polar catastrophe [31]. Li *et al.* measured the magnetic moment of LAO/STO interfaces using torque magnetometry [32]. The values they found are somewhat smaller than those measured using SQUID for samples grown under similar conditions but the order of magnitude they find is $0.4 \mu_B$ per interface unit cell. Very recent work gives a direct relation between interface conductivity and ferromagnetism [33] where only those interfaces are found to be ferromagnetic which are also conducting above the critical thickness of four unit cells. Theoretical work of Pavlenko *et al.* showed that oxygen vacancies could locally lead to an enhanced charge density and favor a ferromagnetic state [34]. Taking into account the particular dielectric properties of STO may provide a description where electrons delocalize over a few unit cells inside the substrate [35].

It appears that interfaces of $\text{LaAlO}_3/\text{SrTiO}_3$ by pulsed laser deposition are always ferromagnetic. There can be a discussion on the amount of magnetization and it seems to vary as the conductivity of the reported interfaces vary. The growth conditions and cooling down procedure are very relevant to the different reported values. In contrast, we find that the SrTiO_3 substrates we use give a ferromagnetic contribution, but that the sputter-grown interfaces do not show more magnetism than what we find in the substrates. Our conclusion is that they are only slightly or even non-magnetic.

6.6.2 Experimental

Thin films of LAO on STO with thickness ranging from 5 nm to 20 nm were prepared using RF reactive sputtering at high oxygen pressure of 0.8 mbar at 920°C . The magnetic properties of the films were measured using a SQUID magnetometer in RSO (Reciprocating Sample Option) mode in the temperature range between 10 K to 400 K and magnetic fields up to 7 T. For reference, the magnetic susceptibility of few a STO substrates was also measured. Films were usually grown on $10 \text{ mm} \times 10 \text{ mm} \times 0.5 \text{ mm}$ STO substrates. For the SQUID measurements they were cut with a tungsten wire (using Silicon Carbide powder, mesh 800 and Paraffin oil as lubricant) into pieces of $5 \text{ mm} \times 5 \text{ mm}$. Some samples were also cut by a dicer with a Nickel wheel saw. Care was taken not to handle the substrates with other metallic objects but we suspect that cutting with the Ni saw might have contami-

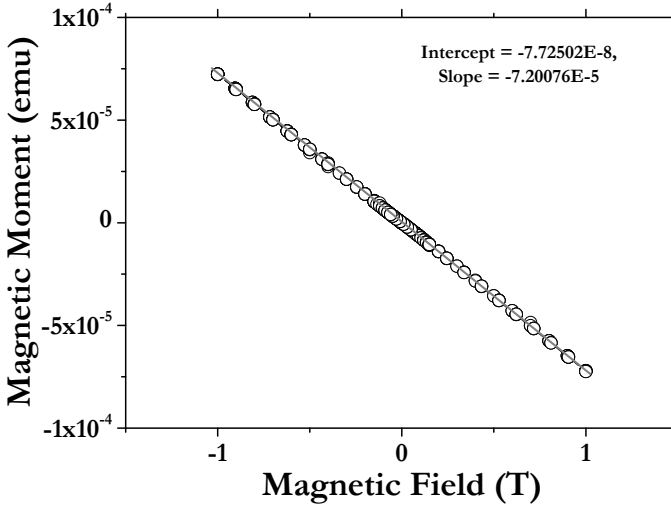


Figure 6.20: Magnetic field versus magnetic moment for an STO substrate at 300 K.

nated some STO substrates during cutting. More experiments are being performed to exclude this possibility.

The data will be given in terms of magnetic moment as measured in the SQUID from the fitted dipole signal. The cgs unit for magnetic moment is called here e.m.u, which corresponds to 10^{-3} Am^2 .

6.6.3 Results

To quantify the origin of possible ferromagnetism in LAO/STO grown by sputtering, we used a systematic approach. A singly terminated STO substrate was measured at 5 K and 300 K and the same substrate was measured again after heating to 920°C at 0.8 mbar of oxygen pressure without growing LAO films (defined as 0 nm LAO/STO, LA115).

First, the field dependent magnetic moment was measured as shown in Figure 6.20, for an STO substrate at 300 K. The STO substrate is diamagnetic. Using the slope of $-7.2 \times 10^{-8} \text{ Am}^2/\text{T}$, sample dimensions $5 \text{ mm} \times 5 \text{ mm} \times 0.5 \text{ mm}$ and a density of 5120 kg/m^3 , we find a susceptibility of $-1.4 \times 10^{-9} \text{ kg/m}^3$, in good agreement with the early experiments [36]. To check any ferromagnetism in the low field region, the diamagnetic background contribution is subtracted and the resulting moment is shown in Figure 6.21. This step was done for all measured samples and we next show only the M-H loops after diamagnetic subtraction.

After background subtraction, Figure 6.21 shows that the STO substrate is slightly ferromagnetic, with an M_s of the order of $8 \times 10^{-7} \text{ emu}$ at 300 K increasing

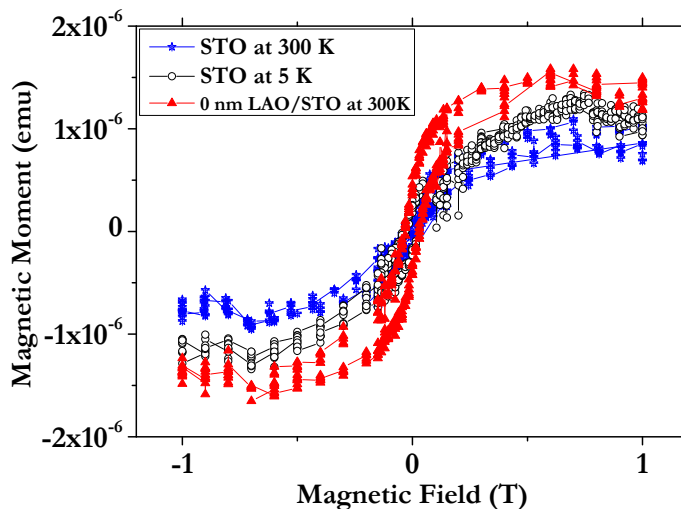


Figure 6.21: Field dependence of magnetization for STO substrates at 300 K and 5 K after subtracting diamagnetic background. A 0 nm LAO/STO (LA115) faced all deposition conditions with LAO film.

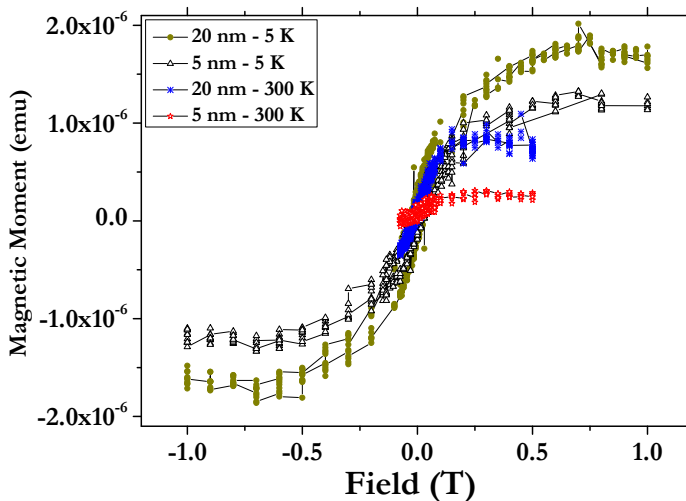


Figure 6.22: Field dependence of magnetization for a 5 nm and 20 nm films of LAO on STO at 5 K and 300 K.

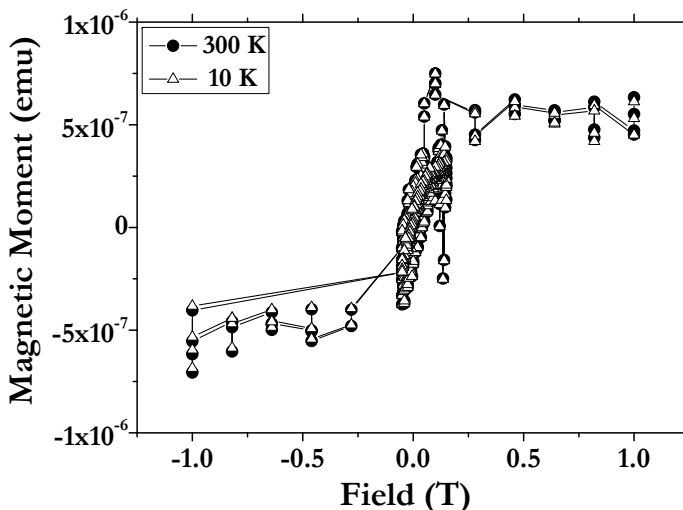


Figure 6.23: Field dependence of magnetization for a 9 nm film of LAO on STO at 10 K and 300 K.

to 10^{-6} at 5 K. The 0 nm LAO/STO (LA115) shows an M_s of 1.5×10^{-6} emu at 300 K, which means increase of a factor 2 after the annealing treatment.

Figure 6.22 shows magnetic field versus magnetic moment of 5 nm and 20 nm films of LAO on STO at 5 K and 300 K. Both samples show a small ferromagnetic loop at lower magnetic field. The difference in saturation magnetization for the 5 nm film and 20 nm film at 5 K is 7×10^{-7} emu. At 300 K, the magnetic moment for both films is lower than at 5 K. The saturation magnetization for the 5 nm film and the 20 nm film is 2.4×10^{-7} emu and 8.6×10^{-7} emu respectively at 300 K. Figure 6.23 shows the magnetic behavior of a 9 nm film of LAO on STO. The saturation magnetization at 10 K and 300 K is the same, 6×10^{-7} emu. Figure 6.24 shows the temperature dependence of magnetization in 1 T for LAO films grown on STO substrates (singly terminated by TiO_2) for 9 nm, 13 nm and 17 nm thin films, a 9 nm thin film of LAO on untreated STO and on a LAO substrate. We see a gradual decrease in diamagnetism in the thin films of LAO. The highest signal is obtained for films of 9 nm and 13 nm grown on treated STO substrates. The magnetization is independent of the temperature for all film.

6.6.4 Discussion

Our sputter grown interfaces show some ferromagnetism at lower temperature but the order of magnitude is the same as in the STO substrate. The effects of heating on STO substrate was studied by growing a 0 nm film (LA115). It is clear that growing a film on TiO_2 -singly terminated STO (Figure 6.22 and Figure 6.23) or

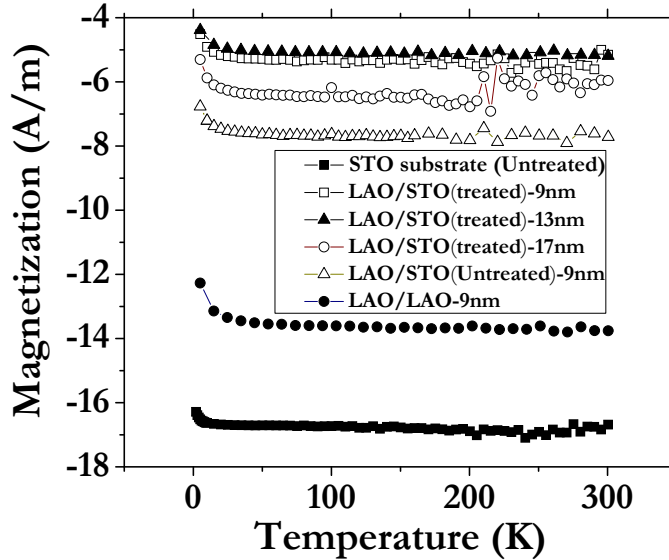


Figure 6.24: Temperature dependence of magnetization measured in 1 T for all films of LAO grown on untreated STO, treated STO and LAO substrates.

not growing at all (Figure 6.21) does not influence M_s or the M-H loop. The sputter grown interfaces show ferromagnetic behavior which is not a pure or partly LAO/STO interface effect, nor that of LAO films. The thickness of the LAO film in this scenario is not relevant, although thicker films needs more heating time to grow, which may affect M_s . Note that M_s increases when going from a 5 nm LAO film to 9 nm to 20 nm. It is also evident from the temperature dependent magnetization that treated STO is less diamagnetic than untreated STO. It seems that treated STO substrates may get some impurities during treatment or the annealing process itself reduces STO substrates to slightly ferromagnetic.

The measured ferromagnetism in the STO substrate is 5 times less than measured by Ariando *et al.* for LAO/STO PLD grown interfaces [30]. Taking a typical measured value of 5×10^{-7} emu ($=5 \times 10^{-10}$ Am²) for a 5 mm \times 5 mm substrate, this would correspond to $0.3 \mu_B$ for one surface unit cell of STO, or interface unit cell of LAO/STO. The same value is calculated by Liu *et al* for LAO/STO interface grown by PLD and measured by torque magnetometry [32]. It can be concluded, taking the 5 nm film as an example, that the interface magnetism in our sputter-grown LAO/STO films amounts to less than $0.15 \mu_B$ per unit cell, and given the presence of ferromagnetism in the substrates probably even much less. This conclusion is qualitatively similar to the one reached in ref. [37], where no magnetism was found in STO/LAO multilayers.

6.6.5 Conclusion

We cannot exclude the possibility that our sputter grown interfaces are ferromagnetic, since the observations are hampered by the presence of ferromagnetism in the STO substrates. Still, since the numbers for the magnetic moments with and without the STO/LAO interface are similar, we conclude that the amount of magnetism is smaller than $0.15 \mu_B$ per interface unit cell, and much smaller than reported in Refs. [30, 32].

Bibliography

- [1] O. Ohtomo, H. Hwang, *Nature* **427**, 423 (2004).
- [2] D.G. Schlomm, and J. Mannhart, *Nat. Mat.* **10**, 68 (2011).
- [3] M. Huijben, A. Brinkman, G. Koster, G. Rijnders, H. Hilgenkamp and D.H.A. Blank, *Adv. Mat.* **21**, 1665 (2009).
- [4] G. Herranz, M. Basletic, M. Bibes, C. Carretero, E. Tafra, E. Jacquet, K. Bouzehouane, C. Deranlot, A. Hamzic, J. - M.Broto, A. Bathelemy, and A.Fert, *Phys. Rev. Lett.* **98**, 216803 (2007).
- [5] W. Siemons, G. Koster, H. Yamamoto, W.A. Harrison, G. Lucovsky, T.H. Geballe, D.H.A. Blank and M.R. Beasley, *Phys. Rev. Lett.* **98**, 196802 (2007).
- [6] A. Kalabukhov, R. Gunnarsson, J. Borjessen, E. Olsson, T. Claeson, D. Winkler, *Phys. Rev. B* **75**, 121404(R) (2007).
- [7] C. Cancellieri, N. Reyren, S. Gariglio, A. D. Caviglia, and J.-M. Triscone, *Euro, Phys. Lett.* **91**, 17004 (2010).
- [8] A. Kalabukhov, Y.A. Boikov, I.T. Serenkov, V.I. Sakharov, J. Borjesson, N. Ljustine, E. Olsson, D. Winkler and T. Claeson, *Europhys. Lett.* **93**, 37001 (2011).
- [9] P.R. Willmott, S.A. Pauli, R. Herger, C.M. Schlepütz, D. Martocchia, B.D. Patterson, B. Delley, R. Clarke, D. Kumah, C. Cionca and Y. Yacoby. *Phys. Rev. Lett.* **99**, 155502 (2007).
- [10] S.A. Chambers, M.H. Engelhard, V. Shutthanandan, Z. Zhu, T.C. Droubay, L. Qiao, P.V. Sushkob, T. Feng, H.D. Lee, T. Gustafsson, E. Garfunkel, A.B. Shah, J.-M. Zuo, Q.M. Ramasse, *Surf. Sci. Rep.* **65**, 317-352 (2010).

- [11] M.P. Warusawithana, A.A. Pawlicki, T. Heeg, D.G. Schlom, C. Richter, S. Paetel, J. MANNHART, M. Zheng, B. Mulcahy, J.N. Eckstein, W. Zander, and J. Schubert, *Bulletin of the APS* **55**, nr. 2 (2010), abstract ID BAPS.2010.MAR.B37.1.
- [12] B. Förg, C. Richter, and J. Mannhart, *Appl. Phys. Lett.* **100**, 053506 (2012).
- [13] L. Qiao, T.C. Droubay, T. Varga, M.E. Bowden, V. Shutthanandan, Z. Zhu, T.C. Kaspar, and S.A. Chambers, *Phys. Rev. B* **83**, 085408 (2011).
- [14] C.W. Schneider, M. Esposito, I. Marozau, K. Conder, M. Doebeli, Ti Hu, M. Mallepell, A. Wokaun, and T. Lippert, *Appl. Phys. Lett.* **97**, 192107 (2010).
- [15] S.A. Chambers, *Surf. Sci.* **605**, 1133 (2011).
- [16] C.S. Hellberg, *Bulletin of the APS* **56**, nr. 1 (2011), abstract ID BAPS.2011.MAR.A34.5.
- [17] S. Thiel, G. Hammert, A. Schmehl, C.W. Schneider, J. Mannhart, *Science* **313**, 1942 (2006).
- [18] M. Huijben, G. Rijnders, D.H.A. Blank, S. Bals, S. Aert, J. Verbeeck, G. Tendeloo, A. Brinkman, and H. Hilgenkamp, *Nature* **5**, 556 (2006).
- [19] M.L. Scullin, J. Ravichandran, C. Yu, M. Huijben, J. Seidel, A. Majumdar, R. Ramesh, *Acta Mater.* **58**, 457 (2010).
- [20] A. Brinkman, M. Huijben, M. van Zalk, J. Huijben, U. Zeitler, J.C. Maan, W.G. van der Wiel, G. Rijnders, D.H.A. Blank, and H. Hilgenkamp, *Nature Materials* **6**, 493 (2007).
- [21] N. Nakagawa, H.Y. Hwang and D.A. Muller, *Nature Materials* **5**, 204 (2006).
- [22] N. Reyren, S. Thiel, A.D. Caviglia, L.F. Kourkoutis, G. Hammerl, C. Richter, C.W. Schneider, T.H. Kopp, A.-S. Ruetschi, D. Jaccard, M. Gabay, D.A. Muller, J.-M. Triscone, J. Mannhart, *Science* **317**, 1196 (2007).
- [23] A.D. Caviglia, S. Gariglio, N. Reyren, D. Jaccard, T. Schneider, M. Gabay, S. Thiel, G. Hammerl, J. Mannhart, and J.-M. Triscone, *Nature* **456**, 624 (2008).
- [24] Y.Z. Chen, D.V. Christensen, F. Trier, N. Pryds, A. Smith, S. Linderoth, *Appl. Surf. Science* **258**, 9242 (2012).
- [25] C. Bell, S. Harashima, Y. Hikita, and H.Y. Hwang, *Appl. Phys. Lett.* **94**, 222111 (2009).
- [26] C.W. Bark, D.A. Felker, Y. Wnag, Y. Zhang, H.W. Jang, C.M. Folkman, J.W. Park, S.H. Baek, H. Zhou, D.D. Fong, X.Q. Pan, E.Y. Tsymbal, M.S. Rzchowski, and C.M. Eom, *PNAS* **108**, 4720, (2011).
- [27] R. Pentcheva, and W.E. Pickett, *Phys. Rev. B* **74**, 035112 (2006).

- [28] P. Delugas, Phys. Rev. Lett. **106**, 166807 (2011).
- [29] Z.S. Popovic, S. Satpathy, and R.M. Martin, Phys. Rev. Lett. **101**, 256801 (2008).
- [30] Ariando, X. Wang, G. Baskaran, Z.Q. Liu, J. Huijben, J.B. Yi, A. Annadi, A.R. Barman, A. Rusydi, S. Dhar, Y.P. Feng, J. Ding, H. Hilgenkamp, T. Venkatesan, Nat. Comm. **2**, 188 (2011).
- [31] J.A. Bert, B. Kalisky, C. Bell, M. Kim, Y. Hikita, H.Y. Hwang, and K.A. Moler. Nature Phys. **7**, 767 (2011).
- [32] L. Li, C. Richter, J. Mannhart, R.C. Ashoori, Nature Phys. **7**, 762766 (2011).
- [33] B. Kalisky, J.A. Bert, B.B. Klopfer, C. Bell, H.K. Sato, M. Hosoda, Y. Hikita, H.Y. Hwang, K.A. Moler, Nature Commu. **3**, 922 (2012).
- [34] N. Pavlenko, T. Kopp, E.Y. Tsymbal, G.A. Sawatzky, J. Mannhart, arXiv:1105.1163 (2011)
- [35] K. Michaeli, A.C. Potter, and P.A. Lee [arXiv:1107.4352 (2011)].
- [36] H.P.R. Frederikse, and G.A. Candela, Phys. Rev. **147**, 583 (1966).
- [37] M.R. Fitzsimmons, N.W. Hengartner, S. Singh, M. Zhernenkov, F.Y. Bruno, J. Santamaria, A. Brinkman, M. Huijben, H.J.A. Molegraaf, J. de la Venta, and I.K. Schuller, Phys. Rev. Lett. **107**, 217201 (2011).

Summary

This thesis deals with the properties of doped perovskite manganites in the form of thin films, and with interfaces between insulating perovskites. In perovskite manganites, the correlations among the manganese d -electrons lead to the occurrence of two coupled transitions when going from high temperatures to low temperatures, an Insulator-to-Metal and a Paramagnetic-to-Ferromagnetic transition. Various questions still surround this phenomenon, in particular in films which are thin enough so that strain induced by the substrates becomes a parameter also. The basics of the physics is formed by doping an insulating so-called Mott insulator (in this case LaMnO_3) so that the material becomes metallic, at least at low temperatures. Doping means replacing the trivalent La, and we have used two different divalent doping ions, Sr and Ca, to study the magnetotransport properties of the prototype manganites $\text{La}_{0.7}\text{Sr}_{0.3}\text{MnO}_3$ (LSMO) and $\text{La}_{0.7}\text{Ca}_{0.3}\text{MnO}_3$ (LCMO). These compositions are chosen such that they give the highest magnetic/metal-insulator transition temperature for these materials and a wide ferromagnetic-metal regime in the phase diagram.

The first question we investigate has to do with the strong reduction of the metal-insulator (MI) transition temperature when the films are strained. In particular, we investigate whether there is an influence of a change in carrier density due to strain. This is done by growing LSMO and LCMO by the so-called sputtering technique, discussed in **chapter 3**, on substrates with different lattice parameters, and measuring the Hall effect. The results, presented in **chapter 4**, show that there is no difference in carrier density for strained and unstrained films, and that the lowering of the transition temperature is purely the effect of a smaller hopping probability or bandwidth of the Mn d electrons. The data also shows, however, that the carrier density averaged over the film thickness decreases when the films become very thin. This we ascribe to the effects of the interface, and of magnetically dead layers which form close to the interface, in which charge discontinuities prob-

ably play a role. The anomalous Hall effect indicates that the different scattering mechanisms are participating in thin/strain and thick/relaxed films.

Another issue, addressed in **chapter 5**, is the behavior of such films when structured into bridges of sub-micron dimensions. For LCMO, it was found before that in the narrow temperature range of the MI transition the resistance becomes current-dependent, or, in other words, that the current(I) - voltage(V) characteristics become non-linear. Here, we investigate a similar manganite, but now Sr-doped instead of Ca-doped. The results are quite different. Down to bridges with a width of 1 μm , the IV characteristics are perfectly linear, showing that the Sr-doped material is less sensitive to strain and disorder. For bridges of 300 nm width this changes, IV-characteristics now do become non-linear, but not specifically in the transition. This effect can be ascribed to a slight oxygen deficiency which is occurring in the bridges, possibly due to structuring.

We then turn the attention to a different issue in **chapter 6**, namely the conductance of the interface between two band insulators LaAlO_3 (Lanthanum aluminate) and SrTiO_3 (Strontium titanate). This is a much debated phenomenon, which was extensively studied on interfaces grown by pulsed laser deposition (PLD) in a background of low oxygen pressure. Using the sputtering technique, this pressure has to be much higher in order to grow good films and interfaces, and to our surprise we find the interfaces to be perfectly insulating. Apparently, the charge transfer mechanism (often called electronic reconstruction) which is supposed to play a role in generating the conducting interface, can be made non-operative when enough oxygen is available. A detailed study of the properties of the sputtered $\text{LaAlO}_3/\text{SrTiO}_3$ films and interfaces indicates that the La to Al ratio in the film is not stoichiometric, but that the films are rather $\text{La}_{1.1}\text{Al}_{0.9}\text{O}_3$, presumably because the high pressure leads to enhanced scattering of the light Aluminum atoms. This ratio higher than 1 makes it difficult to vary the amount of oxygen at the interface during or after the growth, which then leads to its insulating character. For the conducting interfaces fabricated by the PLD technique, the La/Al ratio is found to be less than 0.9, showing that deposition pressure, La/Al ratio and conductivity are strongly related, and that both the La/Al stoichiometry of the LaAlO_3 film, and the oxygen stoichiometry at the interface play a vital role in defining the conductance of the interface. Magnetic measurements were also performed on the sputter-grown and non-conducting interfaces, and they were found to be non-magnetic, again in contrast to what is found on PLD-grown conducting interfaces. Since the magnetism is thought to derive from defects in the oxygen octahedra surrounding the Ti atoms at the interface, this once more emphasizes the importance of the interface oxygen stoichiometry in the mechanisms for conductance and magnetism.

Samenvatting

Dit proefschrift behandelt de eigenschappen van dunne films en interfaces gemaakt van gedoopte manganaten met de perovskiet structuur en met perovskiet isolatoren. Deze materialen zijn van belang omdat de correlaties tussen de *d*-electronen van de Mn-ionen tot een bijzonder fenomeen leiden, namelijk een gekoppelde isolator-naar-metaal en paramagneet-naar-ferromagneet overgang, als het systeem wordt afgekoeld van hoge naar lage temperatuur. Er zijn verschillende openstaande vragen ten aanzien van de mechanismen hiervoor, met name in films die zo dun zijn dat de strain van belang wordt, die bijna onvermijdelijk geïnduceerd wordt door het substraat.

De fysica die ten grondslag ligt aan de faseovergang is die van een zogenoemde Mott isolator (in dit geval LaMnO_3) waarin het driewaardige La vervangen wordt door tweewaardig Sr of Ca, zodat het systeem een metaal wordt, althans bij lage temperaturen. Wij hebben de magnetotransport eigenschappen van dunne films bestudeerd van twee welbekende materialen in de familie van manganaten, $\text{La}_{0.7}\text{Sr}_{0.3}\text{MnO}_3$ (LSMO) and $\text{La}_{0.7}\text{Ca}_{0.3}\text{MnO}_3$ (LCMO). De hoeveelheid Sr (Ca) is hierbij zo gekozen dat daarmee de hoogste overgangstemperaturen binnen het doping-fasediagram bereikt worden.

De eerste vraag die onderzocht wordt heeft te maken met de sterke verlaging van de metaal-isolator (MI) overgangstemperatuur die optreedt wanneer de film onder rekspanning (strain) staat. We gaan in het bijzonder na of er in dit geval een andere ladingsdragerdichtheid optreedt. Hiervoor worden LSMO en LCMO films gegroeid met behulp van de zogenaamde sputter-techniek (zoals besproken in Hoofdstuk 3) op substraten met een verschillende roosterparameter. Vervolgens wordt het Hall effect gemeten. De resultaten, gepresenteerd in Hoofdstuk 4, laten zien dat er geen verschil is in ladingsdragerdichtheid voor films die wel of niet onder strain staan, en dat de verlaging van de overgangstemperatuur alleen het gevolg is van de kleinere bandbreedte van de Mn *d* electronen. De data laten echter

ook zien dat de ladingsdragerdichtheid gemiddeld over de filmdikte wel kleiner wordt als de films erg dun worden. Dit wordt toegeschreven aan de effecten van het grensvlak, en van de magnetisch dode lagen die zich daar vormen, waarbij de ladingsdiscontinuïteit tussen film en substraat waarschijnlijk een rol speelt. Verder laat het anomale Hall effect zien dat verschillende verstrooiingsmechanismes een rol spelen in dunne / gestraïnde of dikke / gerelaxeerde films.

Een andere vraag, besproken in Hoofdstuk 5, gaat over het gedrag van dergelijke films wanneer er bruggen van submicron afmetingen in worden aangebracht. For LCMO was al eerder gevonden dat in het smalle temperatuurgebied van de MI overgang de weerstand afhankelijk wordt van de stroom, in andere woorden dat de stroom (I) - spanning (V) karakteristiek niet-lineair wordt. Hier onderzoeken we het vergelijkbare LSMO, maar vinden heel ander gedrag. In bruggen met afmetingen groter dan $1 \mu\text{m}$ zijn de IV karakteristieken perfect lineair, wat toont dat het Sr-gedoopte materiaal minder gevoelig is voor strain en wanorde dan het Ca-gedoopte materiaal. Voor bruggen van 300 nm breedte verandert dit, de IV-karakteristieken worden nu niet-lineair, maar dat is niet beperkt tot het gebied van de overgang. Het effect kan toegeschreven worden aan een lichte zuurstof-deficientie, mogelijk ontstaan tijdens de structurering.

Vervolgens wordt de aandacht verplaatst naar een ander vraagstuk (Hoofdstuk 6), namelijk de geleiding van het interface tussen de bandisolatoren LaAlO_3 (Lanthaan aluminaat) and SrTiO_3 (Strontium titanaat). Hierover is veel discussie, en het verschijnsel werd al intensief bestudeerd aan interfaces gegroeid met de zogenaamde pulsed laser deposition techniek (PLD) in een achtergrond van lage zuurstofdruk. Met de sputtertechniek moet een aanzienlijk hogere druk gebruikt worden om goede films en interfaces te groeien, en tot onze verrassing vinden we dat deze interfaces perfect isolerend zijn. Blijkbaar werkt de ladingsoverdracht (vaak elektronische reconstructie genoemd) die verondersteld wordt een rol te spelen bij het creëren van het geleidende interface, niet meer als er genoeg zuurstof tijdens de groei aanwezig is. Een gedetailleerde studie van de eigenschappen van de gesputterde $\text{LaAlO}_3/\text{SrTiO}_3$ films en interfaces toont aan dat La/Al verhouding in de film niet stoichiometrisch is, maar dat de films eerder $\text{La}_{1.1}\text{Al}_{0.9}\text{O}_3$ zijn, waarschijnlijk omdat de hogere druk tot een sterkere verstrooiing van het lichte Al atoom leidt. Deze verhouding groter dan 1 maakt het moeilijker om de hoeveelheid zuurstof aan het interface nog tijdens of na groei te variëren, wat leidt tot het isolerende karakter. Bij de geleidende interfaces gefabriceerd met de PLD techniek wordt een La/Al verhouding gevonden van minder dan 0.9. De depositiedruk, de La/Al verhouding en de geleiding van het interface zijn duidelijk gerelateerd, en zowel de stoichiometrie van de LaAlO_3 film, als de zuurstof stoichiometrie aan het interface spelen een belangrijke rol bij de geleiding daarvan. Er werden ook magnetische metingen uitgevoerd aan de gesputterde en niet-geleidende interfaces, en ze bleken niet magnetisch. Dit is alweer anders dan voor de PLD-gegroeide geleidende interfaces. Aangezien het magnetisme verondersteld wordt samen te hangen met de aanwezigheid van zuurstofdefecten in de omgeving van de Ti atomen aan het interface benadrukt dit nogmaals het belang van de interface zuurstof stoichiometrie bij de mechanismen voor geleiding en magnetisme.

Curriculum Vitae

Ishrat Mubeen Dildar got her early education from a public school and college. She received her degree in Bachelors of Science (BSc) with majors in Mathematics and Physics in 1998 and Master of Science (MSc) in Physics in 2000 from the University of the Punjab (UP), Lahore, Pakistan. She was appointed as a lecturer in Feb. 2004 at the University of Engineering and Technology (UET), Lahore, Pakistan. In 2005, she completed her Master of Philosophy (MPhil) with a research project entitled “Investigation of silver plasma and surface morphology from a nanosecond laser ablation”. She was awarded a scholarship to pursue her studies by the Higher Education Commission, Pakistan in September 2007. She worked in the Laser Center, Free University, Amsterdam as a researcher from September 2007 to May 2008. She joined the Magnetic and Superconducting Materials group (MSM), Leiden University, the Netherlands as a PhD scholar in June 2008. Here, she carried out her research in the area of oxide materials. She was recently promoted to assistant professor at the University of Engineering and Technology, Lahore, Pakistan.

List of publications

- M. Khaleeq-ur-Rahman, M.Z. Butt, Ishrat Mubeen, M.S. Rafique, *Investigation of silver plasma and surface morphology from a nanosecond laser ablation*, Materials Chemistry and Physics **114**, 978-982 (2009).
- E.J. Salumbides, V. Maslinskas, I. M. Dildar, A.L. Wolf, E.-J. van Duijn, K.S.E. Eikema, and W. Ubachs, *High-precision frequency measurement of the 423-nm Ca I line*, Physical Review A **83**, 012502 (2011).
- I.M. Dildar, C. Beekman, X. He, and J. Aarts, *Hall Effect measurements on strained and unstrained thin films of $\text{La}_{0.7}\text{Ca}_{0.3}\text{MnO}_3$ and $\text{La}_{0.7}\text{Sr}_{0.3}\text{MnO}_3$* , Physical Review B **85**, 205103 (2012).
- I.M. Dildar, D. Boltje, M. Hesselberth, Q. Xu, H. Zandbergen, S. Harkema, and J. Aarts, *Conductivity of $\text{LaAlO}_3/\text{SrTiO}_3$ interfaces made by sputter deposition*, e-journal of Surface Science and Nanotechnology **10**, 1 (2012).
- I.M. Dildar, D. Boltje, M. Hesselberth, Q. Xu, H. Zandbergen, S. Harkema, and J. Aarts, *Non-conducting interfaces of sputter grown $\text{LaAlO}_3/\text{SrTiO}_3$ and the role of stoichiometry*, submitted to Applied Physics Letters, arXiv:1111.5047v1.
- I.M. Dildar, K. Uhlirova, and J. Aarts, *Non-magnetic interfaces of sputter grown $\text{LaAlO}_3/\text{SrTiO}_3$ and the contribution of the SrTiO_3 substrate*, in preparation.
- I.M. Dildar, J. Kleibeuker, M. Neklyudova, Q. Xu, H. Zandbergen, and J. Aarts, *Stoichiometry of $\text{LaAlO}_3/\text{SrTiO}_3$ films grown in high pressure sputtering and pulsed laser deposition technique*, in preparation.
- I.M. Dildar, M. Neklyudova, Q. Xu, H. Zandbergen, J. Kleibeuker, S. Harkema, and J. Aarts, *A complete characterization of $\text{LaAlO}_3/\text{SrTiO}_3$ interfaces and films grown by sputter deposition*, in preparation.

List of publications

- I.M. Dildar, M. Hesselberth, and J. Aarts, *Mesoscopic transport in thin films of $La_{0.7}Sr_{0.3}MnO_3$* , in preparation.
- I.M. Dildar, D. Boltje, M. Hesselberth, and J. Aarts, *Avoiding target degradation in thin films of $La_{0.7}Ca_{0.3}MnO_3$* , in preparation.

Acknowledgments

At the end of this dissertation, I am very glad to acknowledge all those without whom this could not be possible. I am thankful to the Higher Education Commission (HEC) Pakistan to award me a scholarship and to the University of Engineering and Technology (UET), Lahore, Pakistan to grant me study leave to further my career. I wish to thank the Leiden Institute of Physics (LION) and the ‘Stichting voor Fundamenteel Onderzoek der Materie’ (FOM) for partially funding this project.

Well-deserved thanks go to my promotor Prof. dr. Jan Aarts for starting me off in the field of material sciences. His support and interest in my project, and the discussions we had, helped much in my motivation for the research.

I am greatly indebted to Prof. dr. M. Khaleeq-ur-Rahman (former chairman of the Physics Department UET, Lahore, Pakistan and Vice Chancellor, G.C. University, Lahore, Pakistan) for his strong support for me and my career. He initiated my interest in research, first as a student, and then as a colleague. He taught me much, and was always there when I needed to discuss a problem.

In the MSM group I met very helpful people. Christianne Beekman, who was my predecessor in the field of oxides, provided me with a strong base and the confidence that I would be able to finish my work in time. The technical skills of Marcel Hesselberth, as well as his conceptual approach and patient explanations inspired me a lot. Federica Galli gave me much time and support, whenever I needed it, and discussions with her proved very useful, not to mention the shared Italian-Pakistani food recipes. Stefano Voltan selflessly assisted in some of the experimental work.

My research work could not be completed without the fruitful collaborations with Prof. dr. Henny Zandbergen, Dr. Qiang Xu and Maria Neklyudova from Delft University on TEM, EELS and EDX measurements. I am grateful for the kind cooperation and concern of Dr. Sybolt Harkema from Twente University

Acknowledgments

in performing XRD and RSM measurements. Thanks to Dr. Josee Kleibeuker from Twente University for providing samples and XPS measurements. I am also thankful for the technical help provided by Daan Boltje (on the oxide system, and with XRR and XRD), by Christian Pen (for technical and mechanical issues) and by Ruud Kuyvenhoven (helping with computer issues).

I am also thankful to my Pakistani friends Saima, Sadia, Afsheen, Faiza and Zakia for their moral support.

I have no words to express my feelings for the love and support of my mother. This thesis is dedicated to her courage. She set high goals for me and never compromised on it. I am thankful to my sisters, brother, nieces and nephews for their unconditional love.

Thanks again to all for making my life successful and beautiful.

Conductance of perovskite oxide thin films and interfaces

Ishtarat Mubeen Dildar



Universiteit Leiden
Casimir PhD series 2013-3
ISBN: : 978-90-8593-148-5

Propositions

accompanying the dissertation

Conductance of perovskite oxide thin films and interfaces

1. Given that there is interest in using manganite thin films as so-called Mott-type field-effect transistors, there is a surprising lack of data on the carrier density in manganite ultrathin films.

News et al., APL **73**, 780 (1998)

Chapter 4, this thesis

2. The polaron liquid which was observed in the metal-insulator transition of microbridges of $\text{La}_{0.7}\text{Ca}_{0.3}\text{MnO}_3$ may also exist in $\text{La}_{0.7}\text{Sr}_{0.3}\text{MnO}_3$. To investigate this, the problem of oxygen depletion in very narrow bridges of the latter material has to be overcome.

Beekman et al., PRB **83**, 235128 (2011)

Chapter 5, this thesis

3. The stoichiometry of the LaAlO_3 film can be expected to be important for the charge transfer to the $\text{LaAlO}_3/\text{SrTiO}_3$ interface, and the occurrence of conductance at the interface.

Chapter 6, this thesis

4. As attractive as it may be, it is difficult to fully rule out oxygen depletion in the bulk of SrTiO_3 as a mechanism for inducing the conducting interface between SrTiO_3 and LaAlO_3 .

Scullin et al., Acta Mater. **58**, 457 (2010)

Chapter 6, this thesis

5. The reconstruction of the TiO_2 -terminated SrTiO_3 surface, as it exists at the start of the growth of LaAlO_3 , may well be a parameter in determining the conductance of the interface, since that reconstruction depends on both the growth temperature and the O_2 partial pressure.

M. B. S. Hesselberth, private communication

6. Even if large single crystal areas of graphene can be grown on Cu, the difference in thermal expansion coefficients between the two materials will seriously hinder the production of high-mobility graphene.
7. A clean Au(111) surface with an artificial gold atom chain on top, is probably a more suitable surface for pulling atomic chains with an STM than a Au(110) surface with Missing Row Reconstruction.

E. Tartaglioni et al., accepted for Fizika Nizkikh Temperatur, 2013

8. Scanning Tunneling Spectroscopy on $\text{La}_{0.5}\text{Sr}_{0.5}\text{CoO}_3$ thin films grown on SrTiO_3 , show that some metallic areas become highly resistive in an externally applied magnetic field, opposite to what is expected in the phase-separation scenario for such films. It suggests the special situation of a non-ferromagnetic insulator with metallic ferromagnetic domains.

S. J. Kelly, PhD Thesis 2012

9. Even time cannot tell whether a decision was right or wrong.
10. Cycling in the rain shortens the distance to a PhD.

Ishrat Mubeen Dildar
Leiden, February 6, 2013